Een (bio)mechanische analyse van stentgraftimplantaties voor het behandelen van aneurysma's van de abdominale aorta

A (Bio)Mechanical Analysis of Stent Grafts for the Treatment of Abdominal Aortic Aneurysms

Sander De Bock

Promotoren: prof. dr. ir. P. Segers, prof. dr. ir. B. Verhegghe
Proefschrift ingediend tot het behalen van de graad van
Doctor in de Ingenieurswetenschappen: Biomedische Ingenieurstechnieken

Vakgroep Elektronica en Informatiesystemen
Voorzitter: prof. dr. ir. J. Van Campenhout
Faculteit Ingenieurswetenschappen en Architectuur
Academiejaar 2013 - 2014

UNIVERSITEIT
GENT

ISBN 978-90-8578-699-3
NUR 954
Wettelijk depot: D/2014/10.500/45

Preface

I have been wandering the halls, auditoria and offices of Ghent University for nine consecutive years now. Not much has changed in these years. The buildings are all in the same worn out state as I've found them. Even the motivational posters in the Plateau (word ingenieur!) are still showing the same smiling faces. Only the perception of things change. Instead of sitting behind the (too small) desks and complaining about the doctoral students supervising exercises, I'm now that very same course assistant, no doubt receiving my fair share of remarks and grievances.

Of those nine years, the last four are conveniently summarized in the book you are about to read (or flip through, looking at some of the pictures). They were spent "doing research", which means (independent) learning, programming, experimenting, measuring, computing, processing, writing and traveling. But what it comes down to is pursuing different paths, trying out new or different ways and then, ultimately, stepping back when you realize it won't work. Of course, over time, with a combination of determination, good timing and a hefty dose of luck, enough progress was made to justify this book's printing costs.

In the multidisciplinary field of biomedical engineering, getting things done requires many talents, of which I possessed none at the start of this PhD. But four years did give me ample opportunity to develop the two most important skills needed to write a thesis.

> *"I'm learning real skills that I can apply throughout the rest of my life ... Procrastinating and rationalizing."*
>
> *Calvin & Hobbes*

During this PhD period, I'm proud to say I've collaborated with (among others): the Centre for X-ray Tomography of Ghent University (UGCT), Dan Devos (M.D.) of Cardiovascular Radiology, Ghent University Hospital, Frank Vermassen (prof. M.D.), Isabelle Van Herzeele (M.D.) and Liesbeth Desender (M.D) of the Department of Thoracic and Vascular Surgery, Ghent University Hospital, the Polymer Chemistry and

Biomaterials Research Group, Ghent University, MPT Europe, FEOps, a spin-off of our department and Vascutek, a Terumo Company. None of these collaborations would have been possible without the networking skills and initial contacts of Matthieu, who could probably sell ice to an Eskimo, if wearing his lucky red sweater (Matthieu, not the Eskimo).

Getting to grips with cardiovascular device research, be it computationally or experimentally, is an easy task when starting a PhD having Matthieu, Peter and Michele around. Their PhD books and tips and tricks are the sole reason I could hit the ground running, and quickly lay the solid foundation for this research. Furthermore, I would also like to thank my promotors, Patrick, Benedict (& Matthieu), to guide this research in the first year and giving me the freedom to pursue the paths I wanted in the later years.

Giving your research a direction is no trivial task and as an engineer, academic research is riddled with paradoxes. Fundamental research and improvements in engineering techniques, while interesting and worth investigating, are often too complex and time consuming to be applied on real life, industrial (or in this case medical) problems. While a mere application of (state of the art) engineering principles is often rejected by the scientific community on the grounds of a lack of novelty, whether the work is actually useful or not.

A second paradox lies in publishing the work. Publications, conferences and meetings are used to share your research with the scientific community. Knowledge is a public good, but for which public? Competitive advantages should be hoarded, as they discriminate you from the pack. Everybody is rivaling and rushing (in the best case), or purposely delaying others (in the worst case), to be the first in getting things published. And the second one (to publish), if only few weeks later, has lost all "novelty". Of course, to be fair, more time is spent complaining about the reviewing process than in actually doing the needed revisions.

This however adds to the challenge of staying motivated and upbeat for four consecutive years. It takes a good share of arrogance to convince yourself you are good at what you do. Convince yourself that the scientific merit of these complex computational techniques will not go unnoticed and without consequence. Convince others that the data you generated could be of use to your peers or the occasional M.D. To manage this, staying motivated is key. And as cartoon tigers tell us:

> *"The secret to good self-esteem is to lower your expectations to the point where they're already met."*
>
> *Calvin & Hobbes*

Four years, meeting people, learning new things and going forward. I would like to thank everybody who has accompanied me to this point.

So let's go on, and continue in the art of growing old.

Contents

Samenvatting
Summary

Samenvatting

HOOFDSTUK 1: EEN KLINISCHE EN BIOMECHANISCHE INTRODUCTIE TOT HET ENDOVASCULAIR HERSTEL VAN EEN ANEURYSMA VAN DE ABDOMINAAL AORTA

Aneurysma's zijn lokale en onnatuurlijke verwijdingen van een slagader. Als deze verwijding optreedt in de aorta, tussen het middenrif en de bifurcatie van de aorta naar de benen, spreken we van een Abdominal Aorta Aneurysma of AAA. Deze ziekte verzwakt het weefsel van de aorta en een scheur van dit verzwakte weefsel leidt tot een levensbedreigende inwendige bloeding, met een mortaliteitsgraad tot 90%. Een onbehandeld aneurysma is dus niet zonder gevaar.

Een alternatief voor de traditionele chirurgie - een zeer zware ingreep die vaak niet kan worden uitgevoerd bij oudere patiënten omwille van de risico's van de chirurgie - is de implantatie van een stentprothese. Dit is een minimaal invasieve techniek waarbij een *stent graft* via de liesslagader in het AAA wordt ontplooid. Een *stent graft* bestaat uit een (nitinol) metalen frame met een geweven omhulsel errond. De prothese schermt het AAA af van de hoge bloeddruk in de aorta, waardoor de kans op scheuren sterk afneemt. De huidige procedure kampt echter nog met enkele langetermijncomplicaties zoals migratie van de prothese, lekkage en het falen van het stentmateriaal door vermoeiing.

De mechanische eigenschappen van de *stent grafts* hebben een invloed op het ontstaan van deze complicaties. Er zijn ook nog verschillende controversiële en onopgeloste kwesties rond endovasculair aneurysmaherstel. Zo is het niet voor elke patiënt duidelijk hoe en wanneer hij moet worden behandeld, aangezien elke behandeling een risico met zich meebrengt. Er wordt een stent geselecteerd met een grotere diameter dan deze van de aorta zodat het implantaat het aneurysma goed kan afsluiten. Hoeveel groter de stent moet zijn om zijn taak te vervullen verschilt voor elke afzonderlijke patiënt en *stent graft*. Een grotere *stent graft* heeft zowel voor- als nadelen.

Experimentele onderzoeken en computersimulaties van de plaatsing van een *stent graft* in anatomisch realistische modellen van de aorta kunnen meer info verschaffen rond het mechanisch gedrag van deze devices. Dit doctoraatsonderzoek heeft tot doel het mechanisch gedrag van *stent grafts* voor het behandelen van AAA te onderzoeken. Hiervoor werden volgende deelonderzoeken behandeld:

- Vier commerciële *stent grafts* worden door middel van μCT-scans opgemeten. De geometrie wordt gediscretizeerd voor gebruik in computersimulaties.
- Het mechanisch gedrag van de implantaten wordt experimenteel vastgesteld. Een vlakkeplaat- en radialekrimptest worden gekoppeld met eindige-elementensimulaties om de computermodellen en materiaaleigenschappen bij te werken.
- De computermodellen van de *stent grafts* worden gebruikt om een parametrische studie uit te voeren. Het effect van nekangulatie, neklengte en de extra grootte van de *stent grafts* op de stabiliteit van de ontplooiing wordt onderzocht.
- Met een experimentele ontplooiing en CT-scan van een device in een nagemaakt silicone aneurysma wordt een virtuele computersimulatie van de ontplooiing van de stent gevalideerd.
- De virtuele ontplooiingsmethode wordt verder ontwikkeld voor het gebruik met *in vivo* patiëntspecifieke data. Het resultaat wordt vergeleken met postoperatieve CT-data.

Het laatste hoofdstuk geeft een samenvatting van het onderzoek en de daaruit volgende conclusies. Mogelijkheden tot verder onderzoek worden aangereikt.

HOOFDSTUK 2: GEOMETRISCHE ANALYSE EN OPSTELLEN VAN EINDIGE-ELEMENTENMODELLEN

Een vaatchirurg heeft de keuze tussen verscheidene commercieel beschikbare *stent grafts* van verschillende producenten. In dit hoofdstuk worden 4 veel gebruikte *stent grafts* onderzocht: de Talent (Medtronic), Excluder (Gore), Zenith Flex en Zenith LP (Cook). Beschikbare exemplaren worden opgemeten door middel van μCT-scanning en metingen met een schuifmaat. Het is duidelijk dat deze toestellen geen regelmatige en herhaalde vorm hebben en slechts bij benadering cylindervormig zijn.

Uit de μCT-data wordt de geometrie van de metallische stents geëxtraheerd door middel van een algoritme in pyFormex, een programma voor het genereren en manipuleren van geometrische modellen. De graft, het synthetische, geweven materiaal is niet goed zichtbaar op de μCT scans en wordt daarom digitaal toegevoegd door de stentringen te omgeven met een kromme, en deze krommen te verbinden tot oppervlakken.

De digitaal gereconstrueerde modellen worden verder aangepast voor gebruik in eindige-elementensimulaties. Dit houdt in dat de stents worden gediscretizeerd door polylijnen met variabele lengte, waarbij de gebogen delen in kleinere lijnstukken worden onderverdeeld dan de relatief rechte delen van de stent. De oppervlakken van de graft worden onderverdeeld in kleine driehoekige segmenten.

Hoewel de gediscretizeerde modellen opgebouwd worden uit scans met hoge resolutie, worden toch enkele vereenvoudigingen en abstracties toegepast. Deze worden aan het einde van dit hoofdstuk besproken.

Hoofdstuk 3: mechanische testen en materiaalkarakterisatie

Dit hoofdstuk bespreekt het mechanisch gedrag van *stent grafts*. Hoewel deze devices reeds jaren op de Europese en Amerikaanse markt beschikbaar zijn, is over de mechanische eigenschappen tot nu relatief weinig bekend. Om deze kloof in kennis te dichten, wordt een gecombineerde experimentele en numerieke methode gebruikt om het materiaalgedrag van deze endoprotheses te onderzoeken.

Het gedrag van de vier *stent grafts*, waarvan in hoofdstuk twee de geometrie werd bepaald, wordt onderzocht. De metallische stents zijn gemaakt van het superelastische nitinol, of van roestvast staal. De kracht die nodig is om deze toestellen te vervormen wordt opgemeten met een experimentele testopstelling. De opgelegde vervormingen zijn een vlakkeplaatcompressie en een radiale compressie, met reductie van de diameter.

Deze experimentele testen worden gecombineerd met computersimulaties die deze testen nabootsen. Door een inverse modelleertechniek kunnen de materiaaleigenschappen van zowel de metallische stent als de geweven graft geschat worden. Het gelimiteerd bereik van de experimentele radiale krimptest wordt hier ook door uitgebreid. Doordat we gebruik maken van twee onafhankelijke experimenten, en aangezien de materiaaleigenschappen van roestvast staal bij benadering bekend zijn, zorgt de goede overeenkomst tussen experiment en simulatie voor een beperkte validatie van onze methode.

Een parametersensitiviteitstudie wordt opgesteld om het effect van variaties in ontwerp en bepaalde aannames te onderzoeken. Hieruit blijkt dat het toevoegen van de graft aan de simulatiemodellen cruciaal is om accurate resultaten te krijgen.

Het rapporteren van deze mechanische eigenschappen kan bijdragen tot het ontwerp van nieuwe stents en kan het verwerken en interpreteren van klinische trials ondersteunen. Toekomstige numerieke studies kunnen van deze data gebruikmaken om realistisch mechanisch gedrag toe te kennen aan deze *stent grafts*.

HOOFDSTUK 4: EEN MECHANISCH INZICHT IN DE INSTRUCTIES VOOR GEBRUIK VAN *stent grafts* IN GEKROMDE EN PROXIMALE ANEURYSMANEKKEN

Elk medisch implantaat heeft instructies voor gebruik, waarin aangegeven wordt in welke omstandigheden het device veilig gebruikt kan worden. Voor stents en *stent grafts* zijn dit voornamelijk morfologische en geometrische criteria rond de plaats van implantatie. Hoewel veel patiënten volgens deze criteria niet geschikt zijn voor endovasculair herstel, worden deze vaak toch behandeld. Het gebruik van *stent grafts* buiten hun instructies voor gebruik is dan ook een voortdurend onderwerp van debat.

In dit hoofdstuk wordt het eerder ontwikkeld model van de Zenith LP *stent graft* (hoofdstuk 2 & 3) gebruikt om een inzicht te verwerven in de risico's geassocieerd met het ontplooien van een endoprothese in een korte proximale nek met grote kromming. In de virtuele omgeving wordt het effect van een wijziging in geometrie onderzocht. De angulatie, neklengte en diameter van de proximale nek worden gevarieerd.

Na het berekenen van de vervormingen en krachten na het ontplooien van de *stent graft* worden enkele maatstaven berekend die gerelateerd zijn aan de stabiliteit van de stent na de endovasculaire procedure: de aansluiting van de endoprothese met de wand, de afname van de doorsnede van de graft, de assymetrie van contactkrachten en de afsluiting van het aneurysma worden onderzocht.

Uit de resultaten blijkt dat de meeste problemen kunnen worden verwacht bij een combinatie van korte en gekromde nekken. Een *stent graft* met een grotere diameter heeft een positief effect op de stabiliteit, maar dif effect is niet voldoende om de korte en geanguleerde nekken te compenseren. Verder maakt dit onderzoek duidelijk dat voor hoeken groter dan 60°, de *stent graft* kan *knikken*, wat de stabiliteit zeer sterk negatief beïnvloedt.

De gebruikte methode toont hoe computersimulaties een snel en goedkoop alternatief kunnen bieden bij parameterische testen. Dit hoofdstuk bekijkt de morfologische limieten van endovasculair aneurysma herstel vanuit een ingenieursstandpunt, waarbij de mechanica van het toestel een grote rol speelt.

HOOFDSTUK 5: IN VITRO VALIDATIE VAN DE VIRTUELE ONTPLOOIING VAN EEN *stent graft*

In dit hoofdstuk wordt een commercieel *stent graft* design (de Talent *stent graft*) virtueel geïmplanteerd in een realistisch aneurysmamodel. Een experimentele ontplooiing van het exemplaar in een nagemaakt siliconemodel wordt vergeleken met het resultaat van de gesimuleerde procedure.

De *stent graft* geometrie werd reeds eerder verkregen (hoofdstuk 2). De materiaaleigenschappen van de nitinoldraad op kamertemperatuur worden bepaald door een uniaxiale trektest op een draadsample, verkregen door het opofferen van een exemplaar van de Talent *stent graft*.

Het silicone aneurysmamodel werd met een hoge resolutie ingescand. Door het hoge contrast tussen de siliconewand en de lucht is het mogelijk zowel binnen- als buitenwand van het model te digitaliseren. De materiaaleigenschappen van de silicone gebruikt in het model zijn onbekend. Een inverse analyse van een inflatietest wordt uitgevoerd, waarbij het model met water onder druk wordt gezet en door middel van een ultrasoon toestel verplaatsingen worden gemeten. Hierbij worden materiaaleigenschappen in een eindige-elementen model gewijzigd tot de verplaatsingen overeen komen met deze opgemeten in het in vitro model.

Vervolgens wordt een stentonplooiing gesimuleerd, waarbij de *stent graft* wordt gekrompen en vervormd om de arteriële geometrie te volgen. Vervolgens zet de stent weer uit en sluit deze het aneurysma af. Er wordt een kwalitatieve visuele vergelijking gemaakt tussen het gesimuleerde en het experimentele resultaat. Voor een kwantitatieve vergelijking wordt de oppervlakte van verschillende doorsnedes opgemeten voor en na ontplooing van een *stent graft*, dit voor zowel het experiment als de simulatie. De toename in oppervlakte van de doorsnede, door de uitwaartse kracht van de stent, is vergelijkbaar in beide gevallen.

HOOFDSTUK 6: IN VIVO CASUS VAN DE GESIMULEERDE IMPLANTATIE VAN EEN *stent graft*

In hoofdstuk 5 werd de eindige-elementenontplooiingsmethode gevalideerd met een *in vitro* silicone aneurysmamodel. In hoofdstuk 6 wordt deze studie voortgezet en aangepast voor het gebruik van *in vivo*, patiëntspecifieke data en modellen.

Volgens de routineprocedure voor aneurysma's van de abdominale aorta wordt voor elke patiënt zowel voor als na endovasculaire behandeling een CT-scan genomen. Deze driedimensionale geometrische data van het arterieel stelsel worden gecombineerd met populatiegemiddelde materiaaleigenschappen van de aortawand, trombus in het aneurysma en aanwezige calcificaties.

Met het gebruik van accurate *stent graft* modellen en een virtuele ontplooiingsmethode kan er, zonder enig risico voor de patiënt, een inzicht verworven worden in de situatie na implantatie van de endoprothese. Het simulatie resultaat is zeer vergelijkbaar, zoweel kwalitatief als kwantitatief, met de postoperatieve CT-beelden van de patiënt. Opmerkelijke vervormingen, zoals het slecht aansluiten van het proximale deel van de stent met de wand en een ovalisatie van de benen van de prothese, worden gereproduceerd in het computermodel.

HOOFDSTUK 7: CONCLUSIES EN PERSPECTIEVEN VOOR TOEKOMSTIG ONDERZOEK

Het laatste hoofdstuk geeft een overzicht van het onderzoek dat voor deze doctoraatsthese ondernomen is, en vat de resultaten en conclusies samen. Enkele suggesties en vooruitzichten voor verder onderzoek naar deze endovasculaire *stent grafts* worden gemaakt.

Summary

CHAPTER 1: CLINICAL AND BIOMECHANICAL INTRODUCTION TO ENDOVASCULAR ANEURYSM REPAIR

Aneurysms are local and unnatural dilatations of an artery. If this dilatation occurs in the aorta, between the diaphragm and the bifurcation of the aorta, it is referred to as an Abdominal Aortic Aneurysm or AAA. The disease weakens the aortic tissue, and a tear in this weakened tissue can lead to life threatening internal bleeding, with an associated mortality rate as high as 90%. Not treating the aneurysm is thus not without danger.

An alternative to traditional open surgery - a straining procedure which is often not feasible in the elderly patient population because of the associated risks - is the implantation of a stent graft. This is a minimally invasive technique in which the stent graft is inserted through the femoral artery, and deployed in the AAA. A stent graft is a (nitinol) metallic frame (the stent) with a woven, covering membrane attached to it. The endoprosthesis shields the AAA from the high arterial blood pressure, strongly reducing the risk of rupture. The current procedure is still associated with long term complications such as migration of the device, leakage and fatigue failure of the stent material.

The mechanical properties of stent grafts have an influence on the prevalence of these complications. Several controversial and unresolved issues concerning endovascular aneurysm repair still exist. For instance, it is not clear when and how each individual patient should be treated, as every treatment carries inherent risks. Also, each stent graft is selected to be oversized, relative to the aortic diameter, to be able to thoroughly seal the AAA. Yet the optimal degree of oversize is unclear, as a larger oversize has both disadvantages as well as benefits.

Computer and experimental research on the deployment of a stent graft in anatomically realistic models of the aorta can provide more data concerning the mechanical behavior of these devices. This doctoral research had the goal of investigating this mechanical behavior of stent grafts for the treatment of AAA. To accomplish this, several partial investigations were carried out:

- 4 commercial stent grafts are measured by μCT scanning. The geometry is discretized for use in computer simulations
- The mechanical behavior of the devices is determined experimentally. Flat plate and radial compression tests are coupled with finite element simulations to calibrate the computer models and material properties.
- The digitized stent graft models are used to perform a parametric study. The effect of proximal neck angulation, length and device oversize on the stability of stent deployment is investigated.
- The device is deployed in a silicone mock aneurysm and a μCT scan of the deployed configuration is made. A virtual computer simulation of the endovascular repair procedure is validated against this computational data.
- The simulation method is further developed for use with *in vivo* patient specific data. The result is compared with post operative CT scans.

Finally, the work is summarized and some conclusions are drawn. Future research perspectives are given.

CHAPTER 2: GEOMETRICAL ANALYSIS AND MODEL CREATION

A vascular surgeon has to make a choice from a large variety of available stent grafts of different manufacturers. In this chapter, 4 commonly used devices are investigated: The Talent (Medtronic), Excluder (Gore), Zenith Flex and Zenith LP (Cook). Available specimens were measured by μCT scanning and a micrometer caliper. It is clear that these devices do not have a regular and repeated design, and are only approximately cylindrical.

From the μCT data, the geometry of the metallic stents is extracted using an algorithm developed in pyFormex, an in-house developed open source program for the generation and manipulation of geometrical models. The graft, the synthetic woven material, is not well visible on the μCT slices. It is digitally added by fitting a spline around the stent rings, and connecting these curves to form surfaces.

The digitally reconstructed models are processed for use in finite element simulations. The stents are discretized using polylines of variable length, with the curved parts being subdivided in more linear segments than the relatively straight sections of the stent rings. The surface of the graft is subdivided in small triangular segments.

Although the models are recreated from high resolution scans, some simplifications and modeling abstractions are made. These are discussed at the end of this chapter.

CHAPTER 3: MECHANICAL TESTING AND MATERIAL CHARACTERIZATION

This chapter discusses the mechanical behavior of stent grafts. Although these devices are approved for use in Europe and the US for many years, mechanical properties have never been reported by (or to) the scientific community. To fill this void, a combined numerical and experimental approach is used to investigate the material behavior of these endoprostheses.

The behavior of the 4 devices, of which the geometry was determined in chapter 2, is investigated. The metallic stents are typically made from the superelastic nitinol material, or stainless steel. The force required to deform the devices is measured using an experimental set-up. The applied deformations are a flat plate compression, and a radial compression i.e. a reduction in diameter.

These experimental tests are combined with computer simulations, mimicking the tests. Using an inverse analysis, the material properties of both metallic stent and woven graft are estimated. The limited range of the experimental radial crimping test is extended using the simulations. There is a good match between the experimental and simulated response. Because of the known properties of stainless steel and the use of two independent experiments, our method is validated.

A parameter sensitivity study allows to investigate the effect of variations in design and model assumptions. The study demonstrates the need of including the graft material in the simulations to achieve accurate results.

The availability of these mechanical properties can assist in the design of novel stents, and can assist in the interpretation and processing of clinical trial data. Future numerical studies can use these data to incorporate realistic mechanical behavior for the stent grafts.

CHAPTER 4: A MECHANICAL INSIGHT INTO STENT GRAFT INSTRUCTIONS FOR USE IN ANGULATED PROXIMAL ANEURYSM NECKS

Each medical device has its instructions for use, which state under what circumstances the device is safe for use. For stents and stent grafts these are mainly morphological and geometrical criteria concerning the area of implantation. Although many patients are, according to these criteria, not fit for endovascular aneurysm repair, they are often treated regardless. The use of stent grafts outside their instructions for use is thus a continuous topic of debate.

In this chapter, the previously developed model of the Zenith LP stent graft (chapter 2 & 3) is used to gain insight into the risks associated with the deployment of an endoprosthesis in a short and angulated proximal aneurysm neck. In the virtual environment, the effect of changing geometry is investigated. The angulation, neck lenght and aortic diameter are varied.

Following the calculation of deformations and forces caused by the deployment of the stent graft some derived metrics, related to the stability of the endovascular procedure, are determined. The apposition of the stent graft with the aortic vessel wall, the decrease in graft area, the asymmetry of contact forces and the ability to achieve a good circumferential seal of the aneurysm are investigated.

The results show that most problems can be expected for a combination of short and angulated aortic necks. A larger oversize of the device has a positive effect on the stability, albeit not enough to compensate for the instability caused by short and angulated necks. Furthermore, the study shows that at angles of angulation above 60°, the device can kink, with detrimental effects on stability.

The employed method shows how computer methods can offer a fast and cheap alternative to in vitro experiments, for parametric testing. The chapter investigates the morphological limits of endovascular aneurysm repair from an engineering point of view, taking into account the mechanics of the device.

CHAPTER 5: IN VITRO VALIDATION OF THE VIRTUAL DEPLOYMENT OF A STENT GRAFT DEVICE

In this chapter, a commercial stent graft design (Talent) is virtually deployed in a realistic aneurysm model. The deployment of the specimen in an experimental silicone mock aneurysm is compared with the result of the simulated procedure.

The stent graft geometry was previously obtained (chapter 2). The material properties of the nitinol wire, at room temperature, are determined from a uniaxial tensile test on a wire sample, obtained after sacrificing a specimen of the Talent stent graft.

The silicone aneurysm model was scanned at high resolution using CT. The high contrast between silicone and surrounding air makes it possible to extract both the inner and outer vessel wall from the images. An inverse analysis of an inflation test was performed, pressurizing the model under water pressure, while the wall displacement was measured using an ultrasound machine. The material properties of the silicone were altered in the finite element model until the simulated displacements agreed with the in vitro measured displacements.

The stent graft deployment procedure is simulated, with crimping of the device, deformation of the stent graft to follow the arterial geometry, and subsequent expansion and sealing of the aneurysm. A qualitative, visual comparison is made between the simulated and experimental result. As a quantitative comparison, the cross sectional area of the vessel is measured, both for the experiment and simulation, before and after stent deployment. The increase in area, caused by the radial expansive force of the stent, compares well in both cases.

Chapter 6: In vivo case study of the virtual deployment of a stent graft device

In chapter 5, the finite element deployment method was validated *in vitro* using a silicone mock aneurysm model. In this chapter, the study is advanced and adapted for use with *in vivo*, patient specific data and models.

As per routine procedure for the treatment of AAAs, each patient is subject to both a pre and post operative CT scan. This three dimensional geometrical data of the arterial system is combined with population averaged material properties for the aortic wall, thrombus in the aneurysm and the numerous calcifications.

Using the accurate stent graft models and the virtual deployment method we are able to gain insight into the mechanical situation after stent graft implantation. The simulation compares well, both qualitatively as quantitatively, with the post-operative CT images of the patient. Remarkable deformations, such as a bad apposition of a proximal part of the device to the wall, and an ovalization of the prosthesis legs, are both reproduced in the computer model.

Chapter 7: Conclusions and future perspectives

This last chapter gives an overview of the research performed, and summarizes the results and conclusions. Some suggestions and perspectives towards further research on endovascular stent grafts are presented.

List of Figures

List of Tables

Abbreviations and Symbols

Abbreviations and acronyms

α angle	Angle between aneurysm and the proximal neck
β angle	Angle between infra and suprarenal aorta
μCT	Micro Computed Tomography
2D	Two dimensional
3D	Three dimensional
4D	Four dimensional (three spatial dimensions plus time)
AAA	Aortic Abdominal Aneurysms
ACE	Anevrysme de l'aorte abdominale, Chirurgie versus Endoprothese
ADAM	Aneurysm Detection and Management
ASTM	American Society for Testing and Materials
CAESAR	Comparison of surveillance vs. Aortic Endografting for Small Aneurysm Repair
CFD	Computational Fluid Dynamics
COBYLA	Constrained Optimization BY Linear Approximation
CPU	Central Processing Unit
CSM	Computational Solid Mechanics
CT	Computed Tomography
CTA	Computed Tomography Angiography
DICOM	Digital Imaging and Communications in Medicine
DREAM	Dutch Randomised Endovascular Aneurysm Management
DSC	Differential Scanning Calorimetry
EVAR	Endovascular Aneurysm Repair
FE	Finite element
FEA	Finite element analysis
FEM	Finite element method
FOV	Field of view
FSI	Fluid structure interaction

IFU	Instructions For Use
LP	Low Profile
nitinol	NIckel TItanium Naval Ordonance Laboratory
OSR	Open Surgical Repair
OVER	Open Versus Endovascular Repair (Veterans Affairs Cooperative Study)
PET	PolyEthylene Terephthalate
PIVOTAL	Positive Impact of Endovascular Options for treating Aneurysms Early
PTFE	PolyTetraFluoroEthylene
SMA	Shape Memory Alloy
STL	Triangulated surface (SurfaceTessellationLanguage)
US	Ultrasound
VDISP	User displacement subroutine
vmtk	Vascular Modeling ToolKit
wt%	weight percentage

Symbols

α	Angle
α	Thermal expansion coefficient
ϵ	Strain
λ	Stretch ratio
μ, α	Material parameters Ogden strain energy function
ν	Poission's ratio
σ	Stress
%	Percentage
A	Area
A_f	Austenite transformation finish temperature
A_s	Austenite transformation start temperature
C	Stress influence coefficients
D	Diameter
E	Young's Modulus, Elastic modulus
F	Force
Fr	French (catheter size)
M_f	Martensite transformation finish temperature
M_s	Martensite transformation start temperature
P	Pressure
r	Radius

t	Thickness

Operators

$\sum$	Sum

Units

$^\circ$	Degree (angle)
$^\circ$C	Temperature (Celcius)
GHz	Gigahertz (frequency)
GPa	Giga Pascal (1e9 Pa, E-modulus)
K	Kelvin
kPa	kilo Pascal (1e3 Pa, pressure)
mm	milimeter
mmHg	milimeter of mercury (pressure)
MPa	Mega Pascal (1e6 Pa, stress, E-modulus)
N	Newton (force)
Pa	Pascal (force per area)

One

An introduction to endovascular aneurysm repair

CHAPTER 1

Clinical and biomechanical introduction to endovascular aneurysm repair

1.1 ANEURYSMS

1.1.1 Epidemiology

Statistics for Flanders [1] show that in 2011 31% or 17729 of all of deaths were caused by cardiovascular disease, with the cause of death in 334 cases (251 men, 83 women) ascribed to the rupture of an aortic aneurysm. An aneurysm (from Greek: $\alpha\nu\epsilon\upsilon\rho\upsilon\sigma\mu\alpha$: widening) is, by definition, a local dilatation of an artery by more than 50% [2]. These aneurysms can occur in all arteries, but most common locations are the abdominal aorta and cerebral vessels.

Aortic Abdominal Aneurysms (AAA) develop in the lower aorta, between the diaphragm and the bifurcation to the iliac arteries, which provide blood to the legs. This degenerative vascular disorder has prevalence rates estimated between 1.3% and 8.9% in men and between 1.0% and 2.2% in women [3]. The discrepancy between men and women is mostly contributed to behavioral differences between sexes, smoking being one of the most important risk factors for AAA (90% of AAA patients have been smokers [4]).

A self-explanatory graph is shown in figure 1.1, which shows the resemblance between per capita cigarette consumption and AAA mortality. With the number of male smokers decreasing, and the number of female smokers rising, the sex ratios for AAA prevalence will likely change as well [3]. Similarly, with the adoption of Western diets, a high number of smokers and increased life expectancy, AAA prevalence in Asian populations is comparable to the Western world [5].

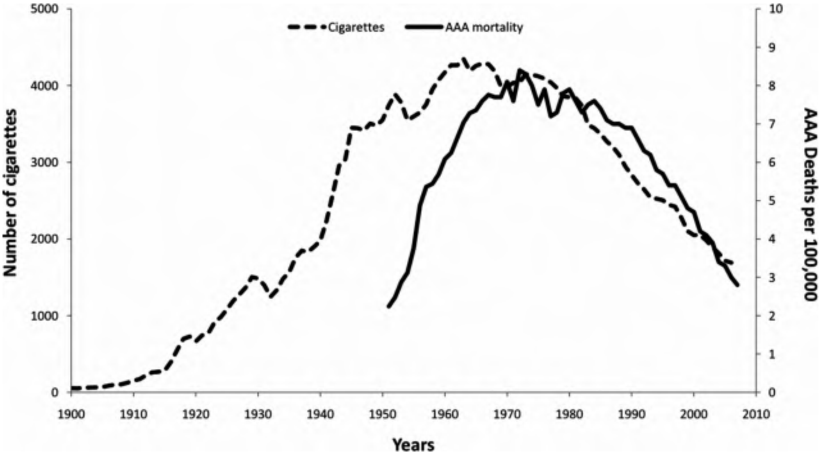

FIGURE 1.1: US annual adult per capita cigarette consumption and US age-adjusted AAA mortality per 100 000 white men by year. Reproduced with permission from [6], Copyright American Heart Association.

1.1.2 Classification

Aortic aneurysms are typically classified according to size, location and geometry.

AAA are grouped according to size in *small* and *large* aneurysms, with a threshold diameter of 5.5 cm. Large aneurysms are often treated, while small aneurysms are managed with rigorous surveillance.

Depending on the location of the AAA relative to the renal arteries, aneurysms are given the classification:

- **Infrarenal** for AAA distal to the renal arteries
- **Suprarenal** for AAA proximal to the renal arteries
- **Juxtarenal** for AAA at the location of the renal arteries

A geometrical and morphological categorization is the difference between fusiform aneurysms with a symmetrical and cylindrical shape, and saccular aneurysms which are more eccentric and bulge out to one side.

1.1.3 Pathophysiology

AAA is a multifactorial disease, affecting elderly patients, with a positive correlation between the presence of AAA and other cardiovascular disorders [4]. Aneurysm formation is associated with structural degradation of the vessel wall. During formation and progression, proteolytic enzymes such as matrix metalloproteinases degrade elastic fibers and collagen [7]. Elastic and collagen fibers are the main contributors to the mechanical properties of the vessel wall, and the loss of elastic fibers plays an important role in aneurysm formation, while collagen degradation seems to be a necessary condition for aneurysm rupture [8]. Furthermore, AAAs are associated with a reduction in smooth muscle cell density [9], and chronic inflammation of the vessel wall. Risk factors for AAA formation are smoking, male sex, age, hypertension, hyperlipidaemia and family history of the disorder.

1.1.4 Symptoms and diagnosis

Unruptured AAA are usually asymptomatic. Most AAA are diagnosed incidentally during medical imaging for other (cardiovascular) diseases. Population screening using ultrasound (US) is safe and effective, and has been shown to be beneficiary for patients [10]. US is used not only for population screening, but also largely for the initial assessment and long term follow-up. Computed Tomography (CT) or CT-angiograms (CTA) are usually the next step to a) determine which treatment to use, and b) perform pre-operative planning. In figure 1.2 an US diagnostic scan of a AAA is shown. Figure 1.3 shows a CT slice of a AAA. In rare cases, AAA are diagnosed after initial symptoms such as chronic abdominal pain and lower back pain without a clear cause. Symptomatic AAA are usually immediately treated.

Symptoms for ruptured AAA can include sudden abdominal pain, shock and a pulsatile abdominal mass. Survival rates depend on the size and location of the tear, but have been reported to be between 35 and 10% [7].

1.2 ANEURYSM TREATMENT

When managing AAA, there are two major questions. A first question is when to intervene. In asymptomatic patients, the 5.5 cm maximum diameter criterion is used. This 5.5 cm is based on treatment criteria for asymptomatic patients, according to the trial criteria for the UK Small Aneurysm Trial [12] and the Aneurysm Detection and Management (ADAM) study [13]. For this diameter, the risk of rupture exceeds the risk of perioperative mortality. Smaller aneurysms ($<$5.5cm) are sometimes

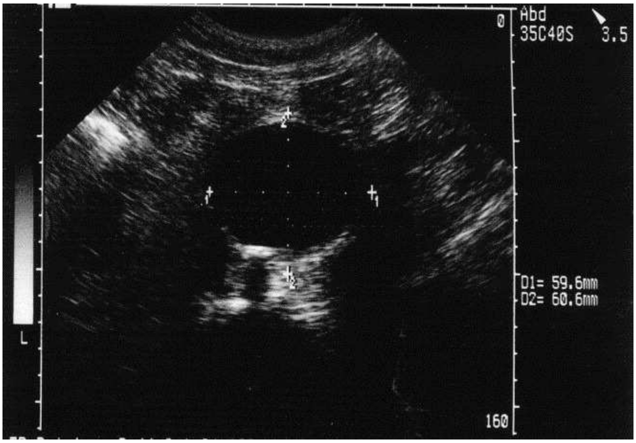

Figure 1.2: Transverse view of an abdominal aortic aneurysm measuring approximately 6 cm in the antero-posterior and transverse dimensions. Reproduced with permission from [11], Copyright Elsevier.

Figure 1.3: Measurement of aneurysm dimensions on a CTA slice. Reproduced from James Heilman, MD under the CC BY-SA 3.0 license.

treated if they have an estimated higher risk of rupture, e.g. in the case of rapid growth, female sex and a family history of AAA rupture. Figure 1.4 shows a possible management plan for asymptomatic AAA.

When the decision is made to treat the patient, a second question arises: how to treat the aneurysm. Before 1991, the only option was open surgical treatment. But since then, physicians (or patients) can opt for an endovascular aneurysm repair. Both techniques are described in the following sections, with an emphasis on the endovascular approach.

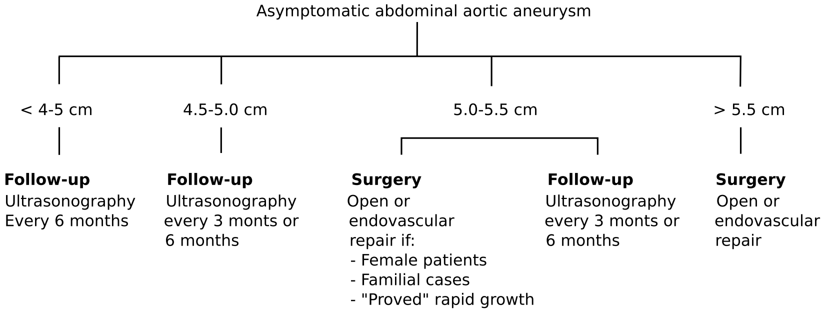

FIGURE 1.4: Possible management of an asymptomatic abdominal aortic aneurysm. Reproduced with permission from [3], Copyright Elsevier.

1.2.1 Conventional open surgical treatment

> *"The patient's rapid recovery made me think that the surgery for aortic aneurysm may become infinitely simple"*
>
> Sir Astley Cooper, 1817

Physician Sir Astley Cooper commented on his patient Charles Hutson after the first surgery of an aortic aneurysm in 1817. The patient died 48 hours after surgery [14].

Open repair is still considered the gold standard treatment for AAA since the first resection of an aneurysm with the use of an arterial graft by Dubost and colleagues in 1952 [15]. During open aneurysm repair, the abdominal aneurysm is exposed through a long midline or wide transverse surgical incision. The proximal unaffected region of the aorta is clamped to stop blood flow into the aneurysm. A vascular graft, a knitted, synthetic textile coated with albumin or collagen, is used to repair the dilated aorta. It is sutured to the healthy aorta, and can be either tubular or bifurcated, depending on the aneurysm morphology and distal suture location.

This invasive therapy is performed under general anesthesia. The repair is durable and rarely requires subsequent aneurysm-related secondary procedures. The conventional surgery is associated with short term mortality risks of less than 5% [16], and a rate of graft failure of about 0.3% per year [7]. Complications related to open surgery include left colon ischaemia and renal failure [3]. Long term aneurysm related complications can be graft or wound infections and thrombo-occlusive diseases.

Because of co-morbidities and higher surgical risks, some patients are less suitable candidates for open surgery. These patients are often treated using minimally invasive endovascular surgery.

1.2.2 Minimally invasive treatment

Endovascular aneurysm repair (EVAR) was developed, and first performed by Parodi et al. [17] in 1991, as a less traumatic alternative to open surgical repair. In EVAR, the risk of aneurysm rupture is reduced by removing the blood pressure load on the aneurysm wall. This is done through catheter based deployment of a stent graft, which does not require large surgical incisions or aortic clamping (and the related risks). Reduced operative risks, shorter lengths of hospital stay and less pain have quickly led to an increase of the use of EVAR. In 2006, 15 years after the first homemade stent graft implantation by Parodi et al., 21725 patients were treated with EVAR in the United States, exceeding the number of open surgical AAA repairs for the first time [18].

EVAR is only feasible for patients with suitable anatomical morphology of the aneurysm, proximal neck and iliac landing zones. Pre-operative measurements of vessel diameters, angulations and healthy attachment lengths are performed on CTA images and are required to size the stent grafts. Figure 1.5 shows the measurements required for sizing a Gore Excluder prosthesis.

The procedure can vary, based on the specific device used. The typical stent graft is a modular, bifurcated design. The device has two main components. The first component deployed is a main body consisting of an aortic trunk and one (ipsilateral) iliac leg. The main trunk has an opening or short contralateral iliac prosthesis leg to connect with the second component. This second component is a contralateral limb prosthesis, for deployment in the contralateral iliac artery. The stent graft can be extended proximally with aortic extender cuffs, or distally using iliac extenders. Figure 1.6 shows the components of the Medtronic Talent stent graft.

The stent graft is, as the name suggests, an aortic graft textile, supported by metallic stent struts. The stent struts are needed to deploy the endograft and stabilize the device against the aortic vessel wall. An EVAR procedure is typically as follows: Bilateral access to the femoral arteries is needed, and is achieved by a surgical cut-down, although in some cases and with some devices, EVAR can be performed percutaneously [19]. The main body is introduced from the largest and/or less tortuous iliac artery, as determined on pre-operative CTA images. The first component of the modular endograft is inserted by a delivery system through one of the femoral arteries, over a (stiff) guidewire.

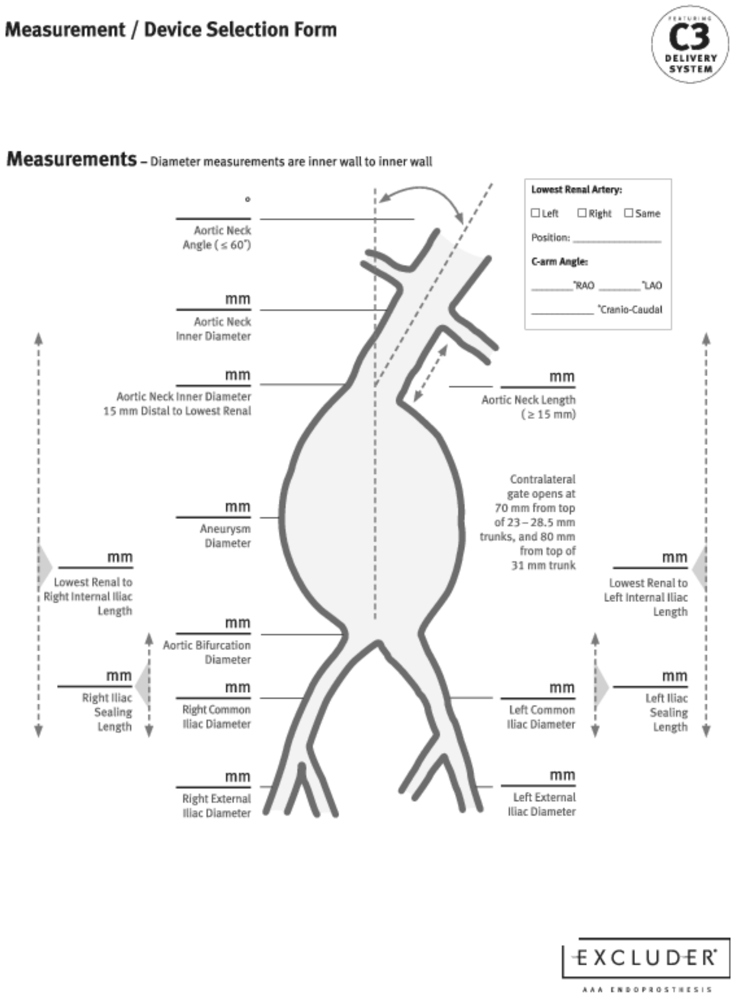

FIGURE 1.5: Measurements needed for sizing an AAA stent graft, adapted from Excluder device selection and measurement form, W. L. Gore & Associates, Inc

The main trunk is pushed up and advanced until the proximal neck. The device is positioned under fluoroscopic guidance. Before endograft deployment, an angiogram is performed to verify the position of the device relative to the renal arteries and aneurysm. If the position is deemed correct, the self expanding main body is released. Current devices (Excluder, Zenith, Endurant; see section 1.3) allow a partial deployment, where the most proximal endograft segment is held compacted to enable repositioning of the device. The deployment of the prosthesis main body opens up the contralateral leg opening.

This opening is cannulated from the contralateral femoral access. The contralateral limb is introduced over a stiff guidewire. Again the compo-

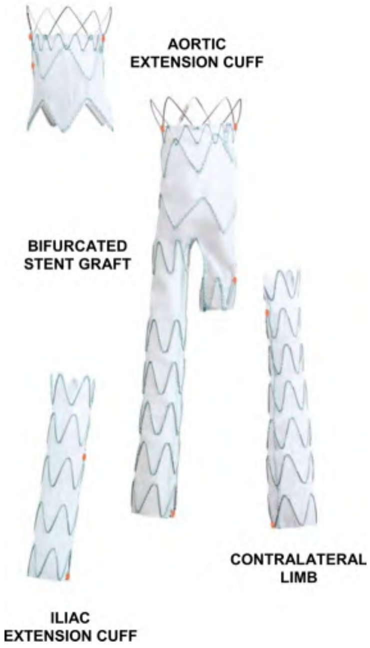

Figure 1.6: Components of a modular stent graft device, adapted from the Instructions For Use of the Talent device, Medtronic Inc.

nent is positioned under fluoroscopy, taking advantage of radio-opaque markers on the main body and contralateral limb. After contralateral limb deployment, if no extenders are needed, the stents are ballooned at the proximal landing site, the overlap between main body and limb component, and at the iliac landing sites. A completion angiogram is performed to confirm good anchoring and no endoleakage. Figure 1.7 shows an EVAR procedure, including two iliac extensions.

1.2.3 Complications after EVAR

EVAR has proven to be a valid alternative to open repair for high risk patients. Stent graft related complications are, however, relatively frequent, and cause problems in the short and (mostly) long term. Aneurysm related re-intervention rates as high as 29% have been reported [20]. Complications include graft migration, endoleakage [20, 21], material failings [22, 23], thrombo-occlusive disease, endotension and infection.

Historically, stent grafts have a poor track record, with a development path riddled with failure modes and even device market withdrawals [24]. Stent strut and hook breaks have been frequently reported [25–29]. To eliminate (fatigue) strut breaks, devices have been changed and

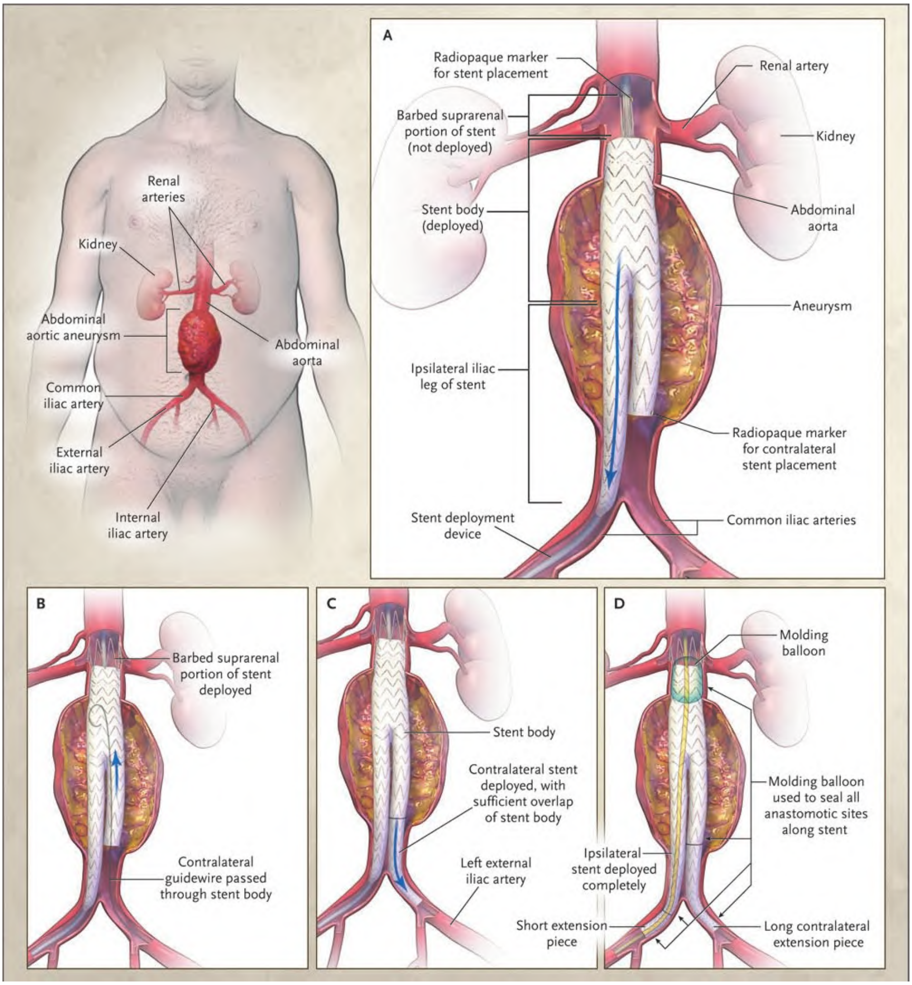

FIGURE 1.7: Panel A shows the insertion of the endograft. The proximal end of the endograft is deployed proximally to the neck of the aneurysm. Devices often have barbs or hooks to help achieve adequate fixation of the device and prevent distal migration (Panel B). The device is only partially deployed to allow repositioning. The contralateral iliac artery limb is deployed from the other access site (Panel C). Extensions are placed in a similar manner. A molding balloon is inflated at multiple sites to ensure fixation(Panel D). Blue arrows indicate movement of the guidewire. Reproduced with permission from [4], Copyright Massachusetts Medical Society.

redesigned. These metallic structural failures can occur because of the geometry of the receiving aneurysm, imposing local stresses onto the stent. Cyclic loading from aortic pulsations can then induce fatigue failure over time [27]. Electro-polishing techniques have been used to improve the stent strut surface [30].

Not only the metallic stent can fail. The graft textile has been shown to fail in fulfilling the endograft's goal of blocking blood flow and pressure to the aneurysm wall. Early devices were highly porous, some even showing blood leaking into the aneurysm sac [30]. Abrasion of the stent struts against the fabric causes graft wear and accelerated breakdown of the fabric. Jacobs et al. [27] found evidence of graft fatigue in 15% of 404 reviewed patients.

Material failure (stent or graft) usually is not a life threatening complication with direct clinical consequences. Strut and hook breaks can however lead to device migration, while holes in the fabric can cause endoleakage that re-pressurizes the aneurysm sac. Endoleak is the main problem for stent grafts. It is defined as the leakage of blood in the excluded aneurysm. This leakage can increase the mechanical pressure on the weak aneurysm wall, and can cause aneurysm rupture. The severity of endoleak, and the related choice of reintervention, is coupled with the location where the blood is leaking past the device. Endoleaks are classified into four types, shown in figure 1.8.

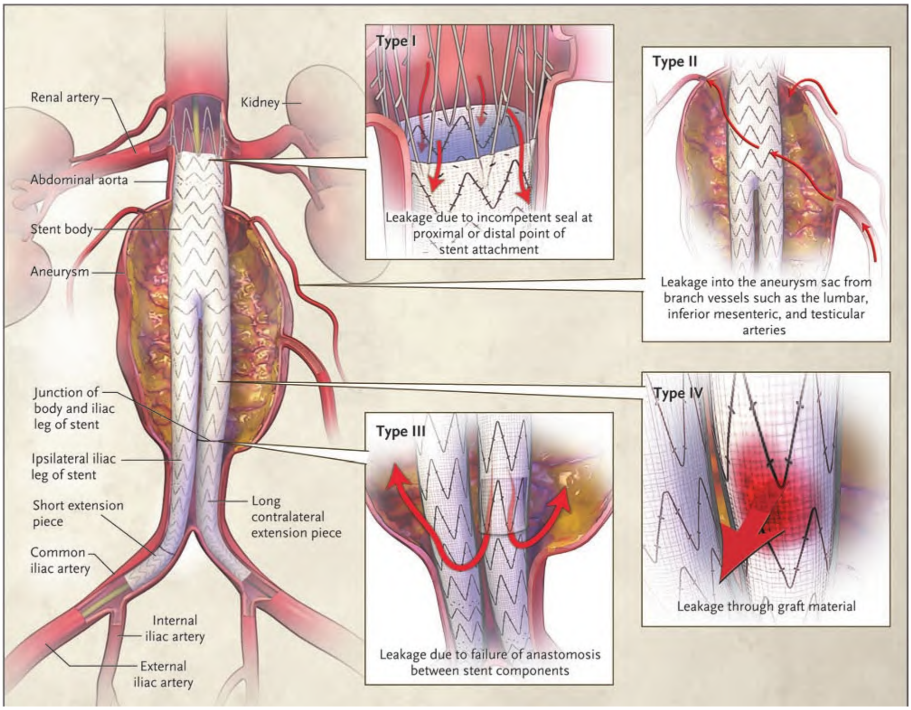

Figure 1.8: The four types of endoleakage, classified by the location of blood leakage. Reproduced with permission from [4], Copyright Massachusetts Medical Society.

Type I endoleaks occur at the proximal or distal landing sites of the device. This can happen because of a bad seal between the endograft and vessel wall, or because of device migration. Migration is usually defined as a distal movement of the prosthesis over more than 10 mm. If the proximal neck was short, the device might no longer cover the complete aneurysm, and type I endoleak occurs. Although modern devices have hooks and barbs to limit device migration, migration is still observed in all approved devices [31]. Detection of Type I endoleak results in immediate reintervention, either endovascular, with the use of extender cuffs, or with conversion to open repair.

Type II endoleaks are caused by reversed flow into the aneurysm from collateral arteries such as the inferior mesenteric and lumbar arteries. These endoleaks sometimes resolve spontaneously. Increased surveillance is often performed to monitor these endoleaks and the aneurysm size. Treatment of these endoleaks can be performed by embolization or thrombin injection into the branch vessels.

Type III endoleak can be either intermodular, at the connection of the stent graft components, or through the device, because of the earlier mentioned material failure. As in type I endoleaks, treatment can be performed with endovascular application of extenders and cuffs, or through conversion to open repair.

Type IV endoleaks occurs because of the porosity of the devices. After the endovascular procedure, thrombosis of the graft and lining with endothelial cells reduces porosity quickly, and treatment is generally not required.

When an increase of aneurysm size is detected during follow-up, without apparent endoleakage, endotension is frequently to blame. It is caused by a transmission of pressure through thrombosed endoleaks or porosity of the graft. Endotension can be caused by any of the causes for each type of endoleakage, but without any visible leak on CTA images. An increase in aneurysm size is often ground for reintervention.

Another frequent complication is thrombo-occlusive disease, where kinking of the iliac stent graft limbs obstructs blood flow, causing lower extremity ischaemia [32, 33]. Tortuous iliac vessels are especially susceptible to to this complication. Occlusion can occur shortly after device implantation, but changes of device position and aneurysm geometry over time can also cause long term complications, such as endoleakage or endograft kinking [34].

1.2.4 Controversies and unresolved issues in EVAR

How to treat

Four randomized studies (EVAR-1[35, 36], DREAM[20, 37], OVER[38], ACE[39]) have investigated the outcome of EVAR compared with open operations, with a total of 2747 patients. All trials are remarkably consistent in many aspects. There is a consensus on improved operative mortality with EVAR, with only the ACE trial reporting similar 30-day perioperative mortality between EVAR and open repair. Likewise, there is a similar 2 year (3 years for the OVER trial) survival rate across the trials, with a "mortality catch-up" offsetting the initial reduction in mortality and morbidity for the EVAR group [40], as shown in figure 1.9. EVAR is also associated with increased (graft-related) re-intervention rates, contributing to higher overall costs. Advantages of endovascular treatment include decreased transfusion requirements, decreased hospital and intensive care lengths of stay, and shorter recovery times after surgery.

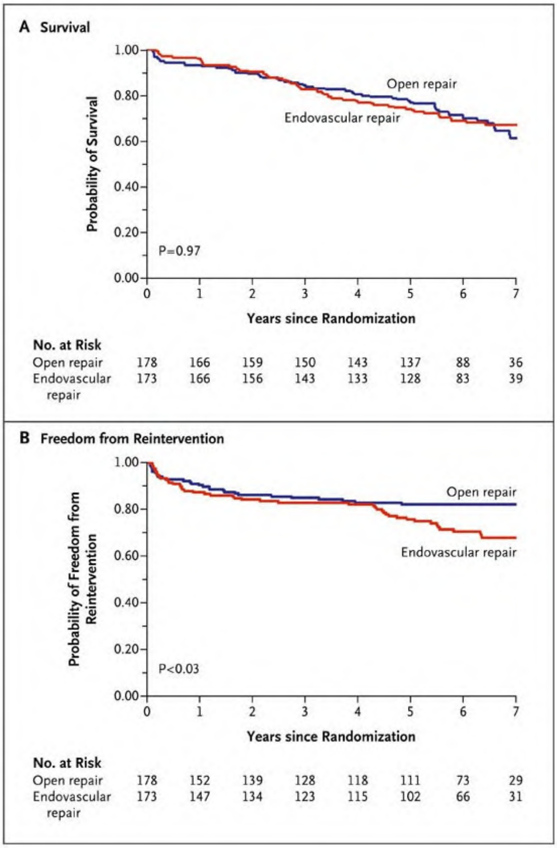

Figure 1.9: Kaplan-Meier estimates of survival (Panel A) and freedom from reintervention (Panel B). Reproduced with permission from [20], Copyright Massachusetts Medical Society.

This would indicate that open repair is as safe as EVAR in the long term, with a lower rate of reinterventions. In an editorial, De Rango and

Cao [41] listed some important points that should be considered when comparing the two therapies. Since the patients have been randomized and treated, over a decade has past. Device design has evolved and has been improved. Surgeon experience with EVAR has increased while at the same time, exposure to open surgery has been reduced.

Similar long term outcomes do allow the patient preference to be taken into account. Perioperative advantages can be weighted by the patient against the need for lifelong surveillance and the higher risk for reinterventions. The unsettling fact remains that whether the patient was treated using EVAR or open surgery, other (non-aneurysm) smoking-related illnesses are the major killers in the long term.

When to treat

In the 4 randomized trials, patients were treated when the AAA diameter was higher than 5.5 cm (EVAR 1), 5.0 cm (DREAM, ACE, OVER), 4.5 cm (ACE for women) or 4.5 cm plus signs of rapid growth (OVER). For open repair, two trials (UK Small Aneurysm Trial[12], and the US Aneurysm Detection and Management trial[13]) failed to show improved survival for earlier treatment, at smaller aneurysm diameters.

Expecting benefits using endovascular treating, with a reduced risk of surgery, the CAESAR (Comparison of surveillance vs. Aortic Endografting for Small Aneurysm Repair [42]) and PIVOTAL (Positive Impact of Endovascular Options for treating Aneurysms Early [43]) randomized studies were started. These studies concluded that both early treatment and rigorous surveillance (and selective treatment) are safe alternatives when treating small AAAs. Over time, most small AAAs grow to require intervention, with the risk of losing morphological suitability for EVAR.

Treating outside instructions for use (IFU)

Not all patients are suitable candidates for EVAR. Anatomic characteristics, such as the morphology of the aneurysm sac, proximal neck and iliac arteries, can restrict the use of EVAR. The most frequent cause for ineligibility for EVAR is unfavorable neck geometry, such as the one visible on figure 1.10. The neck can be too short, too angulated or too calcified and thrombosed. These limitations are given in each device's instructions for use (IFU), as identified by the manufacturer. IFUs are based on bench top engineering tests, preclinical and animal tests and early phase clinical trials. Most device IFUs state that the aortic neck should be greater than 15 mm in length and have an angulation of less than 60°.

While there are many reports on the adverse effects for *off label* use [45–47], some authors report comparable mid-term outcomes between

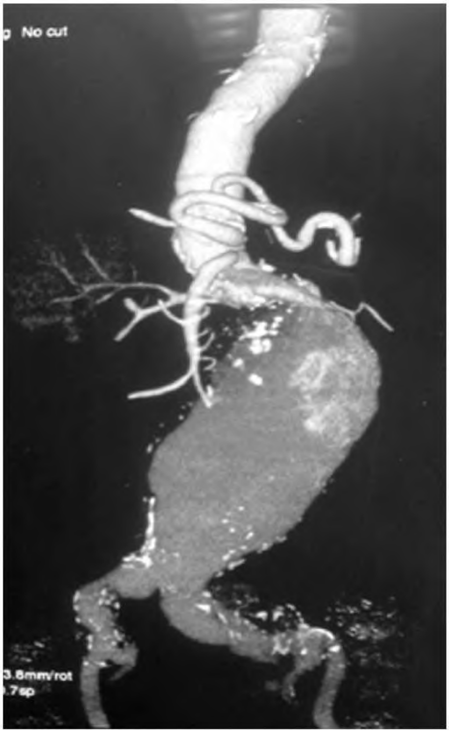

FIGURE 1.10: A short and angulated aneurysm neck, which clearly falls outside the instructions for use. Reproduced from [44] under the CC-BY 3.0 license.

patients with favorable and hostile aneurysm necks [48, 49]. Similar to the comparison between open surgery and EVAR, improved stent graft designs and increased specialist experience are often cited in explaining this discrepancy. Lack of standardized and homogeneous measurements cloud the results of these single-center studies. The heterogeneous patient pool and devices used are other confounding factors.

Adverse effects and benefits of oversizing

Proximal oversizing is needed to ensure good contact and sealing between stent graft and aortic wall. An oversized stent graft also exerts an outward radial force onto the wall, assisting in anchoring the stent and resisting migration. Excessive oversize could however cause stent graft infolding or, in the long term, accelerate neck dilatation.

Neck dilatation, followed by stent graft migration or type I endoleak, raises concerns on the long-term durability of EVAR [50]. Proximal neck dilatation is also observed after open repair, but is significantly greater after EVAR [51]. Wall degradation and continuation of the aneurysmal disease are sure to play a role in degradation, but it is believed that EVAR contributes in two ways: an immediate dilation after placement, possibly correlated with the percentage of oversize (and outward radial force), and a long term dilation over time [52].

A systematic review of benefits and risks associated with oversizing [53] established that most reports use unsuited (or poorly described) measurement techniques and lack repeatability analyses. No strong correlations are found, and data often conflicts. The authors conclude that an oversize of 25% could decrease the risk of endoleak, and while infolding of a stent graft has been reported, data on the risk of infolding and other adverse effects when oversizing more than 30%, were inconclusive [53].

The effect of suprarenal fixation on renal function

Besides choosing when and how to treat, the risk of treating patients outside IFU and the adverse effects or benefits of oversizing, another topic without clear consensus and conclusive data, is the effect of suprarenal fixation on renal function [54]. Post-EVAR renal dysfunction is likely a multifactorial problem, with use of contrast, emboli dislodgement and possibly suprarenal fixation playing a role. For patients treated with stent grafts with suprarenal fixation, about one third had a stent strut located at the renal artery ostium [55]. While the diameter decrease caused by this covering is likely negligible, the impact on the local flow field and shear stress could cause renal artery stenosis, or accumulation of thrombotic material on the stent strut could further reduce the functional cross flow. In a review and meta-analysis, Walsh et al. [54] state: “the current clinical paradigm on the use of suprarenal fixation remains based on an absence of evidence that the technique causes harm, rather than concrete evidence that it is harmless.”

1.3 Stents grafts

Stents are tubular “mesh” structures used to keep arteries open in the case of a stenosis. The goal in EVAR is not to keep the aneurysm open, but to protect the aneurysm wall from the systemic blood pressure, creating a artificial lumen for the blood to travel through. For this a metallic stent mesh is combined and covered with a polymer graft, blocking blood flow.

Since the first homemade device was implanted by Parodi et al.[17] in 1991, over two decades have passed. In 1994 the first commercial devices were launched and since then, have been continuously improved. Today, many commercial options are available, which are distinguishable by the materials used and specifics of the design. For the stent structure, materials used are either stainless steel, nitinol (a nickel titanium alloy) or cobalt chrome. The graft material is either woven PolyEthylene Terephthalate (PET, commonly referenced under the brand name Dacron®) or expanded PolyTetraFluoroEthylene (PTFE, or brand name Teflon®).

All current devices have modular, bifurcated designs, while some of the earlier stent grafts had an aorta uni-iliac configuration. Devices are bimodular or trimodular. They can also differ by the type of fixation: passive, relying on friction forces or the aortic bifurcation for stability, or active, using hooks and barbs to keep the device in place. Fixation type is also subdivided into infrarenal and suprarenal, depending on the location of the anchoring. Supra-renal devices have an uncovered "bare" proximal stent part, allowing blood flow to the renal arteries.

In the following paragraphs, a brief overview of past and currently available devices is given based on information from [56–58], focusing on the designs investigated in this PhD study (Talent, Zenith Flex, Zenith LP, Excluder), yet giving a complete overview of the situation in March 2014. A debate on which stent graft is "the best" is mostly meaningless, as no strong evidence exists in assessing the different stent graft types, or as the authors from the Cochrane Collaboration [59] state: "There are no high quality RCTs comparing one stent graft type with another for the repair of abdominal aortic aneurysms".

Medtronic Talent

The **Talent** (Medtronic Corporation, Santa Rosa, Calif.) stent graft was one of the first devices to use nitinol stents and a woven, thin polyester fabric. The device has passive, suprarenal fixation and has a modular and bifurcated design. It has a high longitudinal stiffness, caused by two longitudinal wires connecting the individual stent rings. The device and its components are shown in figure 1.6. The device has both CE and FDA approval. In Europe, it is now seldom used and has, from 2012 on, been gradually replaced by the Endurant device by the same manufacturer.

Cook Zenith Flex

The **Zenith Flex** device (Cook Medical, Bloomington, Ind.) is a traditional modular and bifurcated design. It has a woven PET graft, with supporting stainless steel Z-stent rings, sutured to the fabric. The design has active, barbed, suprarenal fixation. Notable features are the large number of apices - twelve V-segments over the circumference - and a "top cap", holding the proximal bare stent confined until release, allowing for repositioning after partial deployment. It has CE and FDA approval, and is still frequently used in the USA. The device is shown in figure 1.11.

Cook Zenith Low Profile (LP)

The modular and bifurcated **Zenith LP** (Cook Medical, Bloomington, Ind.) is similar to the Zenith Flex device, but with a lower deployment profile. For this, the stainless steel stents of the Flex are replaced with nitinol stents. Two types of stents are used. The top two stents, a bare suprarenal stent (including hooks) and the first covered stent, are lasercut with a specific geometry. The other stent rings in the main body and iliac legs are made from nitinol wire. The device has a CE mark, but is limited in the USA to investigational use.

Gore Excluder

The **Excluder** (W.L.Gore and Associates, Flagstaff, Ariz.), again a modular and bifurcated design, is different from the previously mentioned devices in many ways. The graft membrane is made from expanded PTFE, which is heat sealed to a spiral nitinol wire. The complete spiral nitinol frame consists of only few wires, which at the proximal side end in hooks. Deployment position is infrarenal with active fixation caused by these hooks. The device is CE and FDA approved, and the device design did not have any recent changes. The delivery has been improved and reduced in diameter with the C3 delivery system (FDA approval in 2010). The device is shown in figure 1.11

Other traditional devices

The first commercial device was the **Vanguard** (Boston Scientic, Natick, Mass.), using a nitinol frame and woven PET membrane, hand sutured to the stent. It was never used in the United States.

The **Ancure** (Guidant Corporation, Indianapolis, Ind., since 2006 part of Boston Scientific and Abbott Labs) was the first device to be FDA approved. The device is bifurcated but not supported by stents in the center. It is implanted below the renal arteries and has both proximal as distal “zigzag” and hook-like fixation made from elgiloy (a cobalt - chromium - nickel alloy). The device was removed from the market for business reasons.

A significant number of patients have been treated with the **AneurX** stent graft (Medtronic Corporation, Santa Rosa, Calif.), shown in figure 1.11. The device has a nitinol, diamond shaped stent exoskeleton and woven PET graft. It was the first truly modular device, including proximal cuffs and iliac extenders.

The latest device by Medtronic is the **Endurant II**. It has active suprarenal fixation and is approved for use in short necks ($>$ 10mm). It is modular and bifurcated, made from nitinol wire stents and high density

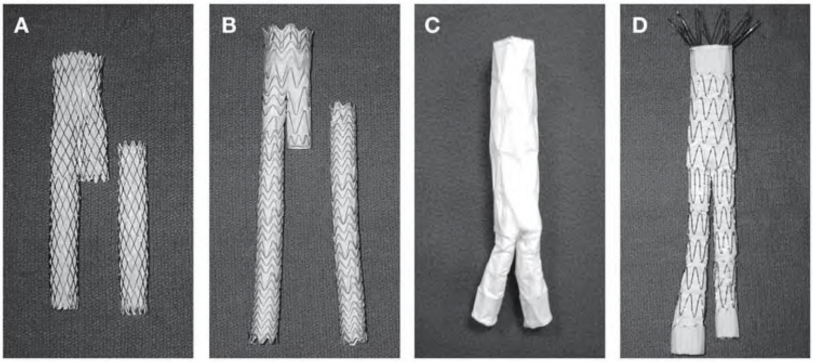

Figure 1.11: FDA-approved endovascular stent graft devices in use in 2007, (A) AneuRx, (B) Excluder, (C) Powerlink, (D) Zenith Flex. Reproduced with permission from [60], Copyright Nature Publishing Group.

polyester graft. Compared with e.g. the Talent stent graft, the Endurant has shorter M-shaped stent rings, with more “hills and valleys”.

Endologix (Irvine, Calif.) has two similar devices: the **Powerlink**, shown in figure 1.11, and its successor, the **AFX** device. Both feature an ePTFE graft with a cobalt chromium alloy stent cage. They offer passive suprarenal fixation and a completely supported graft with diamond shaped nitinol stent. While the Powerlink is a unibody stent graft, the newer AFX device has a main body consisting of two parts, with the distal one deployed first, and resulting in a better anatomical fixation. These devices are not fully “traditional”, as the graft is only sutured to the nitinol frame at the proximal and distal locations. This causes the graft to float away from the stent after deployment and would contribute to a better seal.

Newer devices, under investigational use, are the **Incraft** (Cordis Corporation, Bridgewater, N.J.) and **Treovance** (Bolton Medical, Sunrise, Fla.), both composed of woven polyester fabric and nitinol stents and relying on active suprarenal fixation.

Nontraditional design

Instead of the previously used M or Z shaped stent rings, or a diamond shaped stents, two devices have opted for a radial support only stent, the **Anaconda** (Vascutek, Inchinnan, Scotland) and the **Aorfix** (Lombard Medical, Oxfordshire, England). These devices have circular nitinol rings that offer radial support, and flex into a saddle shape when reduced in diameter. The lack of longitudinal support has the advantage of being very flexible in angulated proximal neck geometries. The Aorfix is licensed in Europe to treat AAA with neck angulations up to 90°.

The **Ovation** (Trivascular, Santa Rosa, Calif.) is a device with a nitinol, active, suprarenal fixation. After deployment, sealing and support is achieved by filling inflatable rings with a hardening polymer. These rings can be seen on figure 1.12.

FIGURE 1.12: The Ovation abdominal stent graft system. Reproduced with permission from [61], Copyright Elsevier.

The **Nellix** (Endologix, Irvine, Calif.) stent graft is a balloon expandable endoprosthesis, consisting of two PTFE tubes supported by cobalt chrome stents. These flow lumens are surrounded with endobags, which are filled with a hardening polymer, filling the entire aneurysm and providing a final anatomical fixation. A schematic illustration of the system can be seen in figure 1.13

Finally, **Aptus/HeliFx** system (Aptus Endosystems, Sunnyvale, Calif.) offers a stent graft device which is, after deployment, anchored with so-called “endostaples”. Using a steerable catheter, these endoanchors fix the graft to the vessel wall. A minimum of 4 helical needles are needed to fixate the Aptus device. The HeliFx system can also be used to treat e.g. type I endoleak with other devices.

1.4 STENT GRAFT MATERIALS

As shown in the overview of existing devices, most stent are made from nitinol and the graft from expanded polytetrafluoroethylene (ePTFE) or polyester (PET, Dacron). Some devices are made from stainless steel or a cobalt chrome alloy. They are used in the elastic domain, and are typical engineering materials. Nitinol on the other hand is a *strange* metal, and its behavior is explained in the next section.

1.4.1 Nitinol

Nitinol is an equiatomic shape memory alloy (SMA) of nickel and titanium. It exhibits both a shape memory effect, and superelasticity. It

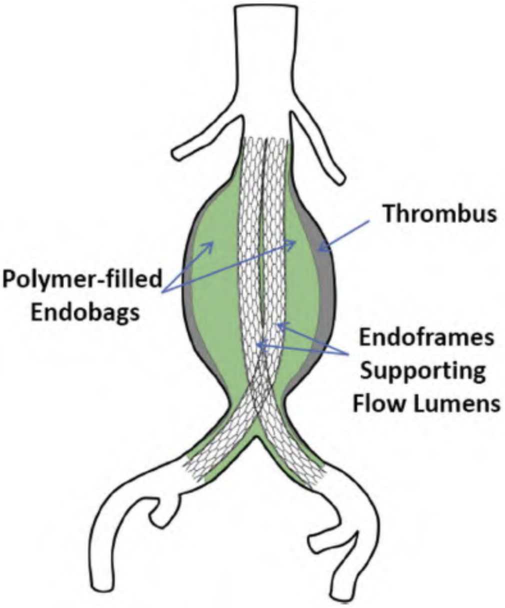

FIGURE 1.13: Schematic illustration of the sac-anchoring endoprosthesis. Reproduced with permission from [62], Copyright Elsevier.

shows good resistance to corrosion by the formation of a titanium oxide (TiO_2) layer on the surface and is biocompatible, making it a great candidate for (endovascular) medical application. Nitinol for surgical implants has between 54.5 and 57.0 wt% nickel (ASTM F2063). Examples of medical applications for SMA include orthodontic archwires, which have been in use since the 1970s. The pseudoelastic behavior of the alloy allows an almost constant exertion of force over a large strain range. Nitinol is often used for cardiovascular applications. Examples include clot filters, such as the Simon vena cava filter, or carotid embolic protection devices. Self-expanding stents and stent grafts are of course a prime example of devices using either the shape memory or superelastic properties of nitinol, or both. The following briefly introduces and explains the unique shape memory and superelastic properties of nitinol, and is based on the book chapter by Hartl and Lagoudas (2008) [63].

Thermomechanical properties

Nitinol has two stable solid phases: an austenite and a martensite crystal structure. These phases have very different material and crystal properties, and transformations from one phase to the other can occur under stress or temperature loading, or a combination.

Austenite nitinol has a certain Young/E-modulus E_A. When loaded, the material transforms into martensite, with an associated Young's modulus E_M (figure 1.14.left). Each phase has a Poisson ratio ν_A and ν_M and coefficients of thermal expansion α_A and α_M (the slope of the strain/temperature curve for fully austenitic or martensitic states as seen on figure 1.14.right).

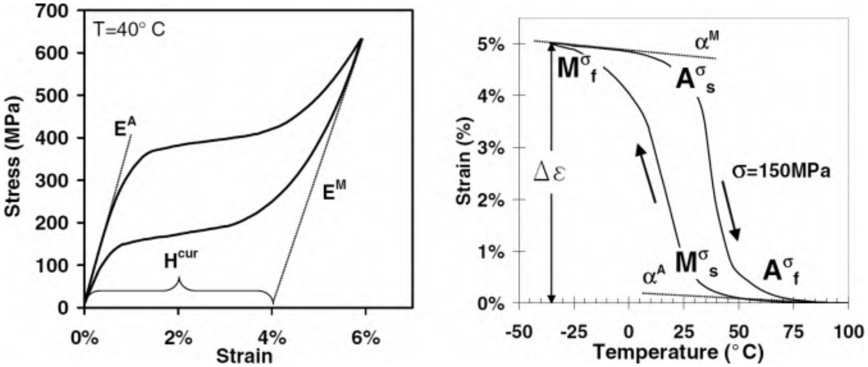

FIGURE 1.14: Examples of (left) the pseudoelastic effect, (right) the shape memory effect. Adjusted with permission from [63], Copyright Springer.

Similarly, when cooling, austenite transforms to martensite, a transformation that starts at a martensite start temperature M_s^σ, ending at the finish temperature M_f^σ, with both temperatures depending on the current stress σ. Subsequent warming would again transform the material to an austenite state, starting at an austenite start temperature A_s^σ, ending at the finish temperature A_f^σ. These temperatures are indicated on the graph displaying the shape memory effect (figure 1.14.right)

In figure 1.15 a constant temperature stress strain curve is considered, for temperatures above A_f^σ. During loading, at a certain stress level σ_{Ms}, the stiffness is reduced and we reach a "stress plateau" as the material transforms. This transformation ends at a stress level σ_{Mf}. Similarly in unloading, the material transforms back to austenite at a stress level σ_{As}, the transformation and associated stress plateau is finished at the stress level σ_{Af}. At temperatures above A_f^σ, the complete shape is recovered, and with allowable strain up to 10%, the material can truly be called *super*elastic. Small permanent strains occur, mainly because of an R-phase in the material. These strains (and the R-phase) are of little relevance in medical grade nitinol and not discussed further.

Higher temperatures will increase these stress levels, which can be seen in figure 1.15.right. The reason for this is more clear when looking at a *phase diagram*, showing the transformation temperatures and their

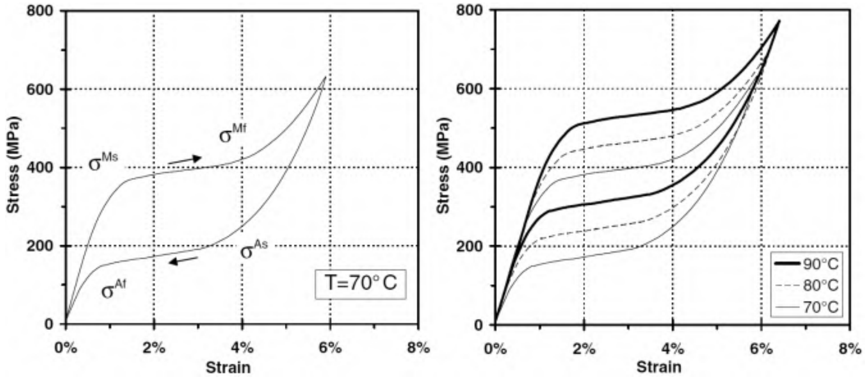

Figure 1.15: Constant temperature nitinol transformations for (left) a single temperature of T = 70°C, (right) multiple temperatures. Adjusted with permission from [63], Copyright Springer.

dependence on the applied load. Figure 1.16 indicates the zero stress transformation temperatures. Transformation temperatures depend on the applied load, with a positive slope: the "stress influence coefficients" C_M and C_A.

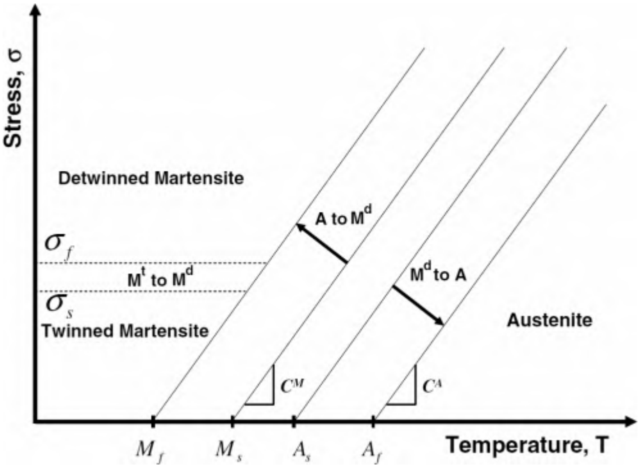

Figure 1.16: Schematic representation of the phase diagram with possible material properties define. Adjusted with permission from [63], Copyright Springer.

At temperatures below M_f^σ, martensite exists in two forms: twinned and detwinned martensite. Twinned martensite is a (random) combination of martensitic variants (a crystal's orientation direction), while after detwinning, one variant is dominant. This reorientation only occurs at high enough stresses, which are indicated in figure 1.16. This detwinning process happens with an “inelastic strain”, and thus causes permanent deformations. It is the basis of the shape memory effect.

To finalize, figure 1.17 shows a stress-strain-temperature curve of nitinol showing the shape memory effect. Starting at A, austenite nitinol is cooled below M_f^σ, transforming to twinned martensite (B). Under a load, the martensite is detwinned, with an inelastic deformation (to C). Unloading the detwinned martensite happens elastically to point D (with an elastic modulus E_M), and a permanent deformation at zero stress. Heating the detwinned martensite will again transform it to an austenite phase, with a complete shape recovery.

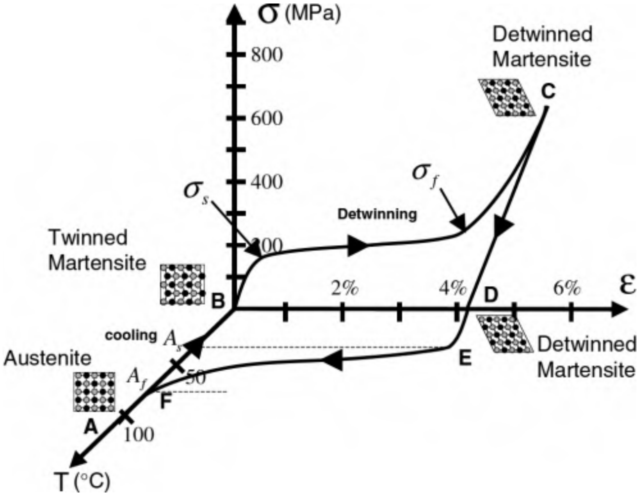

FIGURE 1.17: Stress-strain-temperature data exhibiting the shape memory effect. Adjusted with permission from [63], Copyright Springer.

1.4.2 Graft materials

The main characteristics of the ePTFE and PET grafts used in current devices are discussed in the following sections.

PET

PET is a commonly used and versatile polymer. Uses include soda bottles and packaging containers. When spun to (high strength) fibers, it is often referred to by the trademarked name Dacron. The Dacron fibers can be woven (most common) or knitted to make the graft. Beneficial properties of PET include biocompatibility, durability and good resistance to sterilization and degradation. Properties of PET, such as mechanical strength, porosity and thickness can vary widely and are dependent on the filament size, type of weave and bundling of the yarns

[64]. Anisotropic behavior of a woven Dacron graft (for the Anaconda stent graft) has been demonstrated [65]. The degree of anisotropy of each graft will depend on the manufacturing specifics of each graft.

ePTFE

PTFE is another polymer with many uses. It was patented by chemical company DuPont in 1937 under the brand name Teflon, mostly known as the coating material for non-stick frying pans. In 1969, W.L. Gore's son, Robert, discovered a new state of PTFE, caused by rapid expansion. This expanded PTFE (or ePTFE) is strong, porous (*"breathable"*) and waterproof. Under the brand name GORE-TEX, it is well known as an outdoor clothing fabric. Its properties also make it very suitable for use in medical applications. It has a low friction coefficient, high melting point, low thrombogenicity and is chemically stable [64, 66].

Although the difference between PET and ePTFE can already be seen macroscopically, Scanning Electron Microscopy (SEM) clearly shows the individual fibres of a woven Dacron graft (fig 1.18.A) and the porous structure of an ePTFE graft (fig 1.18.B).

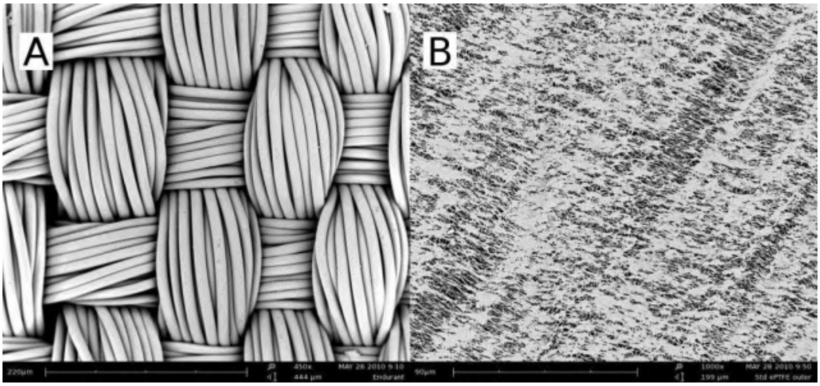

FIGURE 1.18: SEM image of a dacron (450 times enlarged) and ePTFE graft (1000 times enlarged). Adjusted from [67].

1.5 NUMERICAL AND EXPERIMENTAL TECHNIQUES USED IN ANEURYSM BIOMECHANICS

1.5.1 Aneurysm rupture risk assessment

Presumably, the first engineering technique used to investigate AAAs was Laplace's law. It gives the circumferential stress for pressurized thin walled cylinders, which is proportional to pressure (P), radius (r), and inversely proportional to the wall thickness (t) (equation 1.1). This gives an intuitive explanation on why AAAs are prone to rupture: under the same pressure load, the aneurysm wall will, with the vessel having a higher radius, experience a higher stress. If the stress surpasses the material strength, rupture is inevitable.

$$\sigma_{circumferential} = \frac{F_{circumferential}}{A_{circumferential}} = \frac{P \cdot r}{t} \tag{1.1}$$

While providing a theoretical basis for the “maximum diameter criterion”, the use of Laplace’s law is not accurate in predicting rupture risk [68]. A AAA is not a cylindrical tube, or sphere, but a complex and heterogeneous structure with multiple curvatures. Secondly, to accurately predict rupture, both wall stress and wall strength are needed, the latter being disregarded in the use of a maximum diameter criterion.

Since the first FE analyses on wall stress in AAA [69–71], model complexity has increased. Anisotropic material properties of the aneurysm wall have been implemented, and have shown significant differences compared with isotropic wall behavior [72, 73]. Inclusion of thrombus [74, 75] and calcifications [76, 77] have also shown to alter the computed stress state. Finally, when considering patient specific geometries obtained from medical imaging, the obtained geometries are not in a stress free state. They are under (variable) load from the blood pressure. Pre-stressing methods [78–80] change the geometry to its stress free state by inverse analysis. Reeps et al. (2008) [81] showed the impact of these material and geometric model assumptions on patient specific wall stress distributions. Fluid structure interaction (FSI) has also been used to study AAA wall stress [82, 83]. Leung et al. (2006) [84] showed however that including the dynamic interaction of the pulsatile flow with the aortic wall did not significantly alter the peak wall stress.

The previous summary only touches the subject of AAA rupture risk assessment. For the interested reader, more extensive reviews are given in [68, 85, 86].

1.5.2 Experimental studies on AAA stent grafts

Most experimental studies on AAA stent grafts involve the “pull-out force”, i.e. the force that is required to dislodge the device from the proximal neck, or the iliac component from the main body. This has been investigated in human cadaver aortas [87–90], in animal models [91, 92] and in silicone mock vessels [93] for various commercial or self-made devices. These experiments have made it clear that the inclusion of hooks and barbs greatly increase the migration resistance of the device in the proximal neck, and that, for the iliac components, sufficient overlap is needed to ensure good fixation.

Albertini et al. (2005) [94] showed experimentally for a custom device that type I endoleak increased with increasing aneurysm angle, larger than 30°. The influence of endoleaks [95] and endotension [96] on the pressure in the aneurysm sac has also been experimentally determined.

Lin et al. (2012) [97] evaluated folding in the infrarenal Excluder stent graft due to oversizing, barb angle, and barb length using CT images of stent grafts deployed in an animal model. They concluded that folding was possible when the stent graft has an oversize of more than 30%. Changing barb length and angle did not increase the folding risk when oversized within the normal range of 10-20%.

Mechanics of stent grafts have been experimentally investigated. Radial force has been determined for custom devices [98] and smaller stent grafts designs (not used for treatment of AAA) [99] using a loop method (figure 1.19). Radial force for a fenestrated Cook Zenith device was determined by cutting open a stent ring and testing the V segments [100]. This resulted in a circumferential ring stiffness of 0.4 $\frac{N}{mm}$. These experiments did not take into account the graft material. The radial stiffness of tubular stent grafts with diameters ranging from 8 to 24 mm, including the fabric, has been measured using the loop method and a mylar film [101].

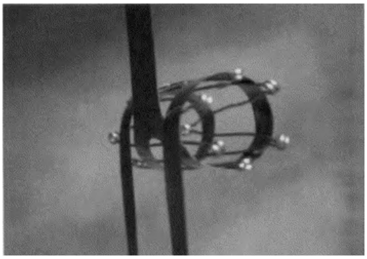

Figure 1.19: Test using loop method and a foil strip to measure radial force exerted by Gianturco stents. Reproduced with permission from [98], Copyright Elsevier.

Yao et al. (2013) [102] developed an in vitro test method for predicting the abrasion resistance of textile and metal components of endovascular stent grafts. Two types of graft fabric material, and two types of stents, a nitinol lasercut and wire stent were investigated in dry and wet conditions. An interesting result was that the laser cut nitinol stent was more aggressive in creating holes and breaking yarns in the graft fabrics than the round stent wire.

Finally, Mestres et al. (2012) [103] determined the most optimal oversize and stent graft combination to use in parallel stenting, with the goal of minimizing gutters (gaps between the main stent graft and the (smaller) chimney or snorkel stent grafts) and stent graft infolding. They found that there is better apposition and smaller gutters with an excessive endograft oversizing (30%), but that stent graft compression and the optimal oversize are device specific.

1.5.3 Numerical studies on AAA stent grafts

Although not as extensively studied as AAA rupture risk, a solid body of literature exists on the computational biomechanics of EVAR. In the following sections, these are grouped by the numerical technique used.

Computational solid mechanics

Using FEA, the wall stress before and after EVAR was investigated [104]. Kleinstreuer et al. (2008) [105] was the first to look into the mechanics of the stent graft device. The mechanical and fatigue behavior was examined, including FE deployment in a straight tube. The device under investigation had a generic diamond shape design and consisted of a nitinol frame with a covering membrane. The effect of different material properties were examined.

Prasad et al. (2012) [106] used FE solid mechanics to model the interaction between the aorta and endograft, calculating the displacement forces using Computational Fluid Dynamics (CFD). A metric for the positional stability of the device was introduced, and the framework was used to assess the effect of neck angle, neck length and oversize on the device stability.

Demanget et al. published multiple papers [65, 107, 108] on the subject of the bending behavior of iliac limbs using device specific geometries and realistic (but equal) material properties. This resulted in a comparison of the unconstrained bending for eight marketed stent graft devices [108]. The work included accurate geometric computer discretization of the different devices, and biaxial material testing on a Dacron graft, determining the anisotropic material behavior.

Prior to stent graft implantation, a (stiff) guidewire is inserted in the vasculature. The interaction of the guidewire with the vessel, and the resulting vessel deformations have been investigated using FEA [109, 110]. Auricchio et al. (2013) [111] performed a computer based analysis for the treatment of an ascending pseudo-aneurysm with a custom-made stent-graft. Medical images were analyzed and a patient specific simulation was performed. The finite element result was compared with post-operative CT images, with encouraging results.

Von Sachsen et al. (2013) [112] developed post-processing software as a stent graft visualization and planning tool, for patient specific finite

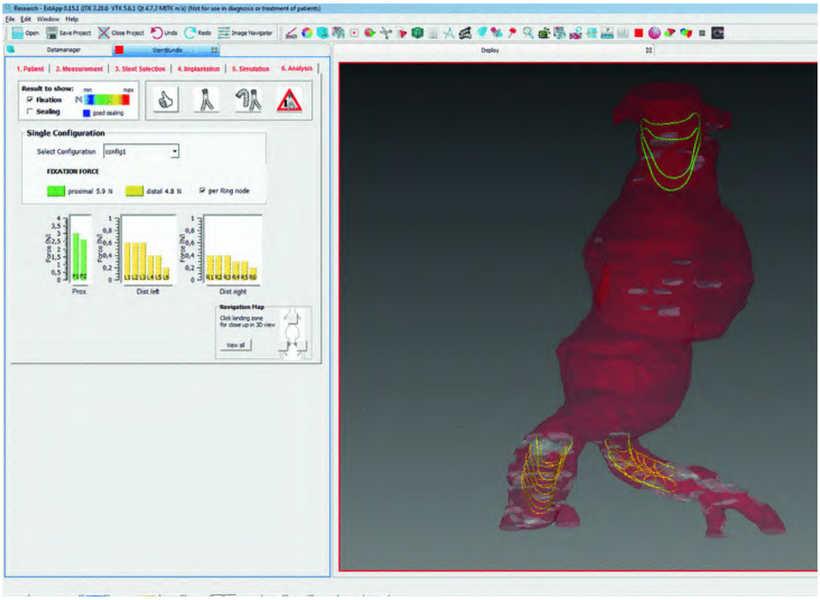

Research - ExtApp 0.15.1 (ITK 3.20.0 VTK 5.6.1 Qt 4.7.3 MITK n/a) (Not for use in diagnosis or treatment of patients)

Result to show: ☑ Fixation ☐ Sealing

Select Configuration: config1

FIXATION FORCE

proximal 5.9 N

distal 4.8 N

☑ per Ring node

FIGURE 1.20: Medical post-processor visualizing FE result. Reproduced with permission from [112], Copyright Springer.

element stent ring crimping and deployment. Unfortunately the actual finite element procedure is not well described, but the software progress in visualizing and presenting finite element results clearly to endovascular specialists is well worth mentioning (figure 1.20).

An example of virtual prototyping using FEA is given in [113] by Arokiaraj et al. In this work, a novel large self-expanding endovascular stent was designed which is incorporated into the aneurysm wall and which, after tissue overgrowth, reduces the peak wall stress caused by the systolic blood pressure.

Computational fluid dynamics

CFD has been mostly used to calculate migration forces after EVAR. The vascular wall and devices are considered as rigid boundaries. Fluid dynamics in bifurcated stent grafts have been examined [114, 115].

Figueroa et al. (2009) [116] investigated the effect of curvature on the magnitude and direction of these forces, caused by the blood flow. Frauenfelder et al. (2006) [117] looked at haemodynamic changes after EVAR, and included an experimental setup for the validation of the non stented aneurysm flow lines.

Xiong et al. (2012) [118] devised a way to perform a “virtual intervention”, for subsequent CFD calculations. The influence of taking into account the individual struts of the device on migration forces was calculated. Applications included EVAR and coronary bypasses. Recently, Morris et al. (2013) investigated the influence of device compliance and geometry on the flow conditions after EVAR, confirming the intuitive notion that abrupt changes in cross-section cause greater migration forces, and a tapered device would be more beneficial.

Fluid structure interactions

Li et al. performed many FSI simulations, coupling the (dynamic) blood flow with vascular wall and stent graft mechanics. The stent graft device mechanics are considered by using an “equivalent” elastic modulus and Poisson’s ratio. The behavior of the device (nitinol frame and fabric) is simplified to a single mechanical property. Contact between the device and vessel wall is fixed and no separation is allowed. These simplifications are needed conditions to allow a complex 3D FSI simulation. Li et al. investigated the pressure and wall stress reduction after EVAR [119] and the effects of type I [120] and type II [121] endoleaks.

Similarly, the reduced wall stress and fluid forces after EVAR were calculated by Molony et al. (2009) [122]. Finally, using coupled FSI analysis, Amblard et al. (2009) [123] analyzed the effect of oversizing on the biomechanics of the proximal neck, showing that a reduction in radial force could induce type I endoleak, and oversize could prevent endoleakage.

Mathematical modeling

Using straightforward mathematical formulas, Liffman et al. (2001) [124] showed that analytical modeling, neglecting dynamic and viscous flow effects, yields similar results as numerical (CFD) simulation of migration forces. These simplified theoretical methods can be very useful in providing an insight into the haemodynamic forces associated with EVAR.

Showing that simpler (faster) mathematical modeling can provide good alternatives for expensive FSI calculations, Wolters et al. (2010) [125] modeled aneurysm intrasac pressure in the presence of an endoleak using both FSI and a lumped parameter model, with good agreement between the results.

1.6 THESIS RATIONALE AND OUTLINE

The work described in this thesis was motivated by the unresolved issues in EVAR, as discussed previously. The question on when to treat, i.e. an alternative to the maximum diameter criterion, has been extensively studied in the past (see section 1.5.1). Rupture risk indexes have been, and are being developed and are already available in product form (`http://www.vascops.com/`). AAA wall stress and rupture prediction are not the focus of this work.

The research shown in the following chapters sheds a light on the mechanics of EVAR, assisting in difficult topics such as the adverse effects and benefits of oversizing, the treatment outside of the IFU, and the objective mechanical comparison of commercial devices.

Previous work on the mechanics of stent grafts (see section 1.5.3) has been limited by the use of generic, parametric geometrical models and material properties, or were limited to the iliac leg components of the modular devices. The performed experimental and numerical modeling aimed to better capture the mechanical behavior of available devices, and simulate the behavior of the device during and after deployment.

The dissertation is organized as follows:

1. Four commercial devices are accurately modeled and discretized. Starting from μCT scans, the device geometry is recreated for use in numerical simulations

2. The mechanical behavior of the devices is determined using bench top experimental testing. Coupling the tests with FE simulations, the mechanical properties of the devices are reflected in the computer models and material properties.

3. A parametric study investigates the effect of neck angulation, neck length and oversize percentage to stent graft deployment stability. Several metrics are suggested to quantify positional stability.

4. The Talent stent graft is both virtually and experimentally deployed in a AAA. High resolution CT scans of the silicone mock aneurysm are used a) to create the virtual aneurysm model and b) after deployment, to validate the finite element deployment against the experimentally deployed device.

5. Finally, the deployment method is adapted for use in patient specific virtual aneurysm treatment. The finite element result is validated using the post-operative medical CT data.

6. The research work is discussed and concluded, and possible perspectives towards future biomechanical research are given.

Two

Computational mechanics of stent grafts

CHAPTER 2

Geometrical analysis and model creation

Stent graft devices have previously been modeled as regular, parametric and perfectly cylindrical. After examining bifurcated device samples, it was clear that this is not the case, the design and the hand made nature of these endografts being prime causes. In this chapter, the creation of (FE) models from device samples is detailed.

2.1 INTRODUCTION: μCT SCANNING OF MEDICAL DEVICES

Microtomography (micro Computed Tomography, μCT) uses X-rays to non-destructively determine an object's three dimensional geometry. Different from plain X-rays, a large number of two-dimensional radiographic images are taken around a single axis of rotation, often visualized in a sinogram (figure 2.1). A single "slice" or tomographic image is generated from these images using a filtered backprojection or the iterative Algebraic Reconstruction Technique.

Stent graft devices were scanned in cooperation with the center for X-ray tomography (UGCT, `http://wwww.ugct.ugent.be`). In the setup used, the devices were rotated (figure 2.2). This in contrast to a medical CT scan, where the X-ray source and detectors are rotated around the patient. The maximum resolution of the scan is determined by the number of pixels in the detector row and the distance from the X-ray source to the object. The size of the object has a direct influence

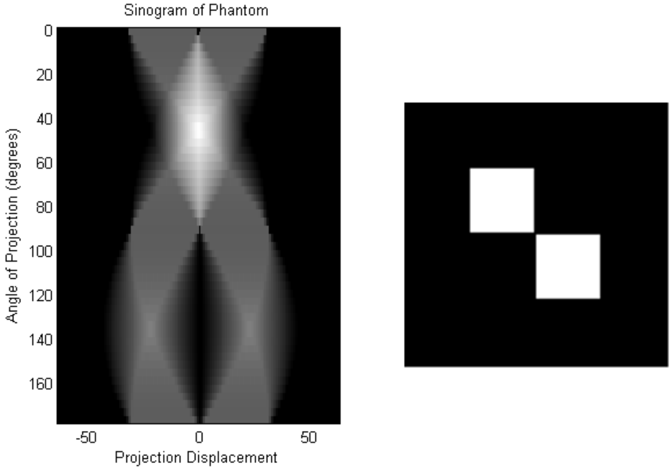

Figure 2.1: Sinogram (left) obtained from a 2D virtual phantom (right), taken at 50 angles.

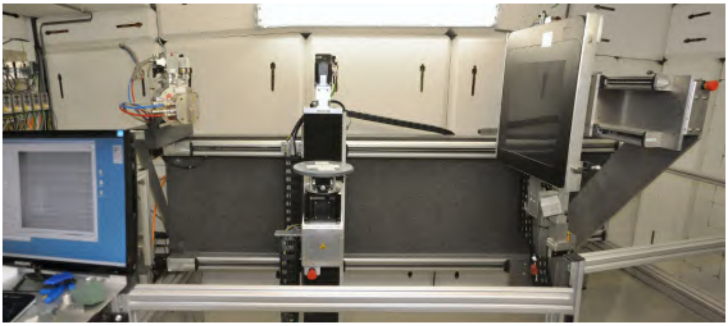

Figure 2.2: μCT set-up, with X-ray source (left), position for the (rotated) specimen (middle) and the flat panel detector (right).

on the obtainable resolution. For the endoprostheses scanned, the final, isotropic, voxel size was between 100 and 120 μm.

The DICOM (Digital Imaging and Communications in Medicine) data, a set of stacked 2D images can be processed by dedicated software such as Mimics (Materialise, Leuven, Belgium) or 3Dslicer (`http://www.slicer.org/`[126]). The good contrast between metal and surrounding air allows to separate the stent wires and export them as a triangulated surface (STL). Figure 2.3 shows a full range (high contrast) slice (left), an elimination of most noise and scattering by a better selection of window level and width (middle), and a good threshold choice to separate the nitinol wires (right). Manual corrections are sometimes needed at the location of the radio-opaque markers. Image masks after segmentation are converted to a three dimensional STL result, as shown in figure 2.4 for the Zenith device.

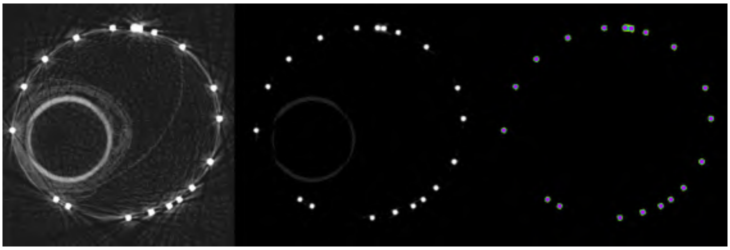

FIGURE 2.3: μCT slice of a scanned stent graft. Full ranged window view (left), altered window level and reduced width (middle), rainbow color lookup table, showing a good threshold for wire separation.

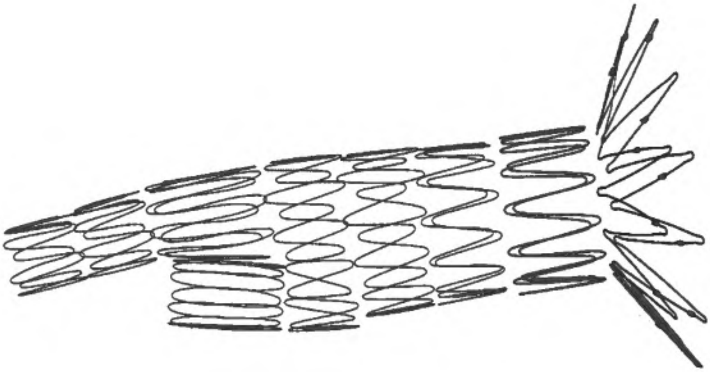

FIGURE 2.4: Visualization of the Zenith STL model.

2.2 EXTRACTION OF INDIVIDUAL WIRE CENTERLINES FROM THE STL

STL surfaces can be used almost directly for simulation if they have a sufficient quality and smoothness, and have the correct dimensions. Despite the high resolution scans, this is not the case for the devices investigated (figure 2.5.a). For most devices and wires, the centerlines were extracted using a self developed algorithm within the open-source pyFormex framework (http://www.pyformex.org). In the following, this algorithm is (graphically) explained.

A single stent segment (figure 2.5.a) is separated from the STL. This ring is unrolled by the use of a coordinate transformation. The stent is now two dimensional, with a horizontal and vertical axis. The M

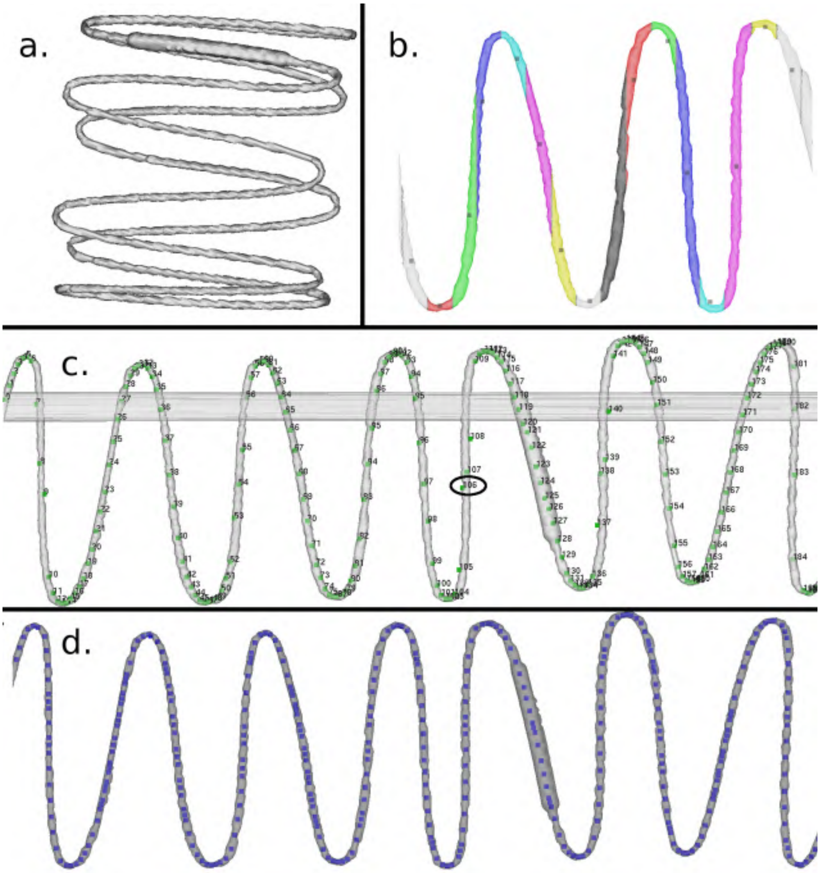

Figure 2.5: Extraction of stent wires from STL surfaces. a) Separated STL of one stent ring. b) Illustration of one dimensional split of an unrolled stent ring and determination of centroids. c) Resulting centroid nodes after a horizontal division in 200 parts. d) Resulting centroids after a two dimensional division, using the points from c).

shaped wire is divided in multiple parts by the horizontal coordinate (as illustrated in figure 2.5.b for a limited number of divisions). The centroid of each part is calculated and saved. Figure 2.5.c shows the 200 centroids after splitting the complete flattened ring in 200 parts. Using these calculated centroids to interpolate a centerline is not accurate for two reasons: the points are not consistently located in the center of the wire (i.e. point 106 in figure 2.5.c), and while there are more (wanted) points in the curved regions, some vertical legs of the M-shape are only sampled 4 times.

The following step in the algorithm is, again, dividing the M-shaped unrolled stent, now based on the previously found points. While in the first division, the split was in one direction, the found centroids now allow a direction (the difference between two subsequent points) and limits (each point) to be defined in both dimensions. If the distance between two points is large, multiple splits are made. The resulting centerpoints (figure 2.5.d) are well placed in the center of the wire. A first interpolation is made using a smooth second order B-spline (figure 2.6.left). The spline is then approximated by a piecewise linear polyline. To reduce the total number of elements in the later FE model, straight sections are approximated by fewer lines than the curved regions, with a limit to the maximum element length (figure 2.6.right).

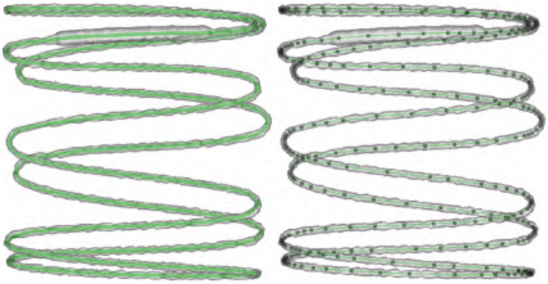

Figure 2.6: Result of the extracted centerline, overlaid with the semitransparent STL, spline curve (left) and polyline, with indicated nodes (right).

The main advantage of the method is the robustness of the algorithm and computations. The computation does not depend on STL quality or properties. Gaps or inverted triangles in the structure are handled without any problem. In some cases, the first, horizontal split was easily altered to allow for manual adjustment of points.

In two special cases, a different approach was followed. The Excluder device is not made from individual rings, but of long continuous wires (figure 2.7). Extracting the centerline of these wires was performed using the Vascular Modeling Toolkit (vmtk, `http://www.vmtk.org`).

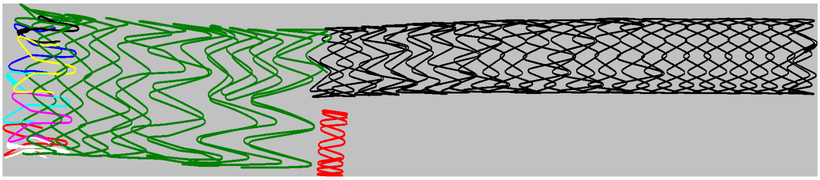

Figure 2.7: Different wires for the Excluder stent graft, each wire is given a different color.

The vmtkcenterlines script takes an STL surface as input, and returns a centerline and the Voronoi diagram, used to determine the centerlines.

The method is fast and reliable, but requires a higher quality STL file. Gaps and irregularities have to be fixed in the segmentation phase in order to use the vmtk centerline extraction. The resulting centerline (figure 2.8) is again approximated with polylines of varying lengths.

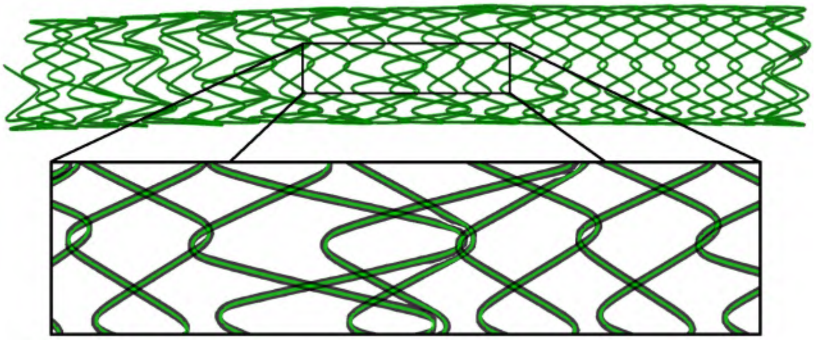

Figure 2.8: Centerline extraction with vmtk for the Excluder device, overlay of the STL with the resulting centerline (green).

The two proximal segments of the Zenith LP stent graft are lasercut from nitinol tubing. A strategy previously used by our group (see e.g. [127, 128]) was followed to get an accurate stent geometry. Using caliper measurements on the sample, measurements on the μCT images and using the unrolled STL as a reference, a basic unit of the stent shape was modeled. Replication of this basic unit and a cylindrical transformation create the complete lasercut segment. These lasercut stents are not perfectly regular (figure 2.9), but the regular replication of the basic unit offers acceptable results.

2.3 Adding the graft to the model

The graft, covering the stent, is only faintly visible on the μCT images (figure 2.3). It is interrupted by the stent struts and ray scatters from both struts and radio-opaque markers. Reconstructing the fabric directly from the images is therefore not feasible. The devices are not regular, and the graft splits at the bifurcation to the iliac limbs. The graft is digitally recreated by a series of spline fits around the stent rings, which are connected to form a surface.

Figure 2.10 shows the creation of a graft membrane around the Talent stent. The first ring (left-hand side) is uncovered for suprarenal fixation, the membrane starts few millimeters before the distal end of this ring. The location of the bifurcation is between the third ring, and the first small iliac stent ring. For this, the spline fit on the third ring is translated

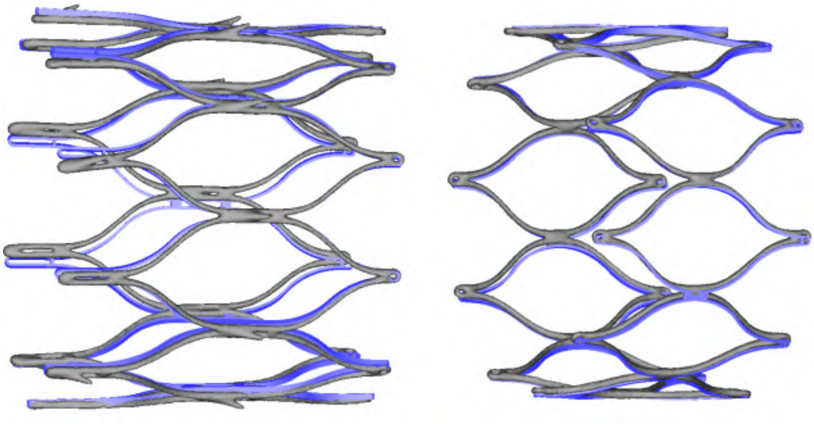

FIGURE 2.9: Modeling of lasercut segments for the Zenith LP device. Overlay of STL surface (black) and FE model (blue).

distally, and contracted radially, by amounts based on visual inspection of the device sample.

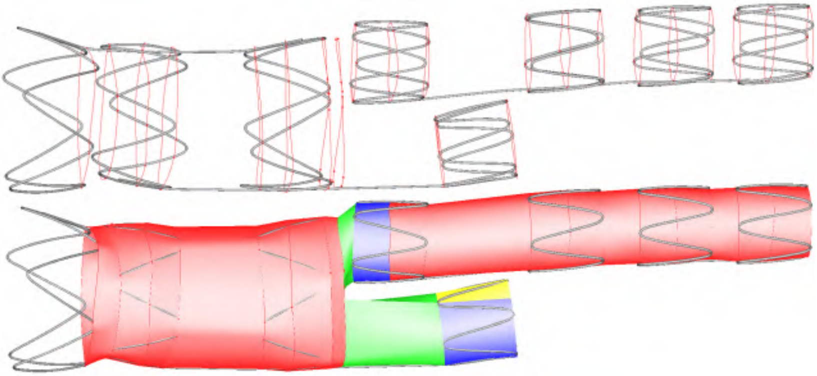

FIGURE 2.10: Modeling of the covering stent membrane. Spline curves are fit through points on the stent rings (top), and are connected to form surfaces (bottom). Visualization of the method for the Talent stent graft.

The splines are discretized by polylines and connected. The result already closely fits the stent rings and allows numerical calculations. Using a shaded rendering of the graft (figure 2.11), changes in angles along the membrane are emphasized. Global and local smoothing combined with manual adjustments reduces these angles and finalizes graft model creation.

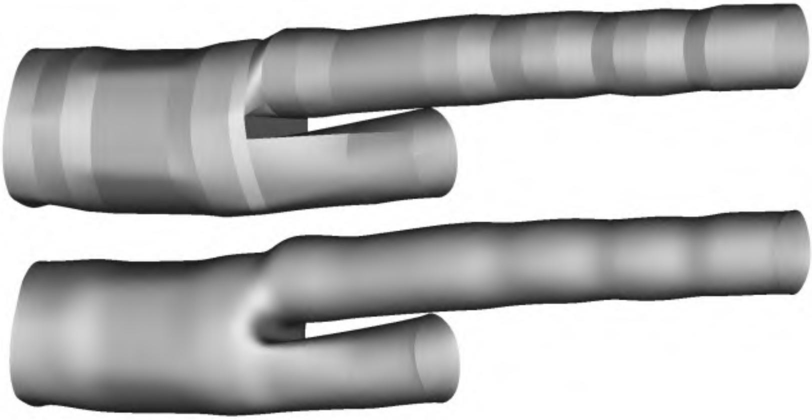

Figure 2.11: Model of the graft after connecting the splines fitted to the stent rings (top). Model after smoothing and processing the graft (bottom).

2.4 Geometrical simplifications and their potential impact on FEA

The discretized models, ready for FE use, accurately reproduce the geometry of the samples. However, some simplifications were made during the model creation. The metallic stents, directly recreated from imaging, almost perfectly match the actual shape. For use in FE simulations, the following abstractions were made:

- Wire stent rings (for Talent and Zenith devices) are made from a single wire, wound in an M-shape and clamped at the ends to form the cylindrical spring. This clamping (presumably with tantalum clips) occurs in a straight part of the M-shaped rings. For this reason, the two overlapping and clamped wires (e.g. visible as the thickening in the rings of figure 2.6 and 2.12) are simplified in the model as one continuous wire.

- Related to the above, and displayed in detail in figure 2.12, is the clamping of the Talent device's longitudinal wire to stent rings. This connection is also modeled without the actual clip. The longitudinal wire is attached to the stent ring wire (which is the simplified representation of the two overlapping ends) by a no slip, "tied" connection. No relative movement of these wires at the location of the connection is allowed.

- The hooks of the Zenith devices (Flex and LP) were not taken into account in the FE models. For the Excluder, the hooks are the ends of the wires used for the proximal stent part, and are modeled as such.

- As shown in figure 2.9, the irregularities of the lasercut stents are not modeled. The non-constant cell sizes are assumed to be different for each sample, and modeling them as regular is an acceptable assumption.

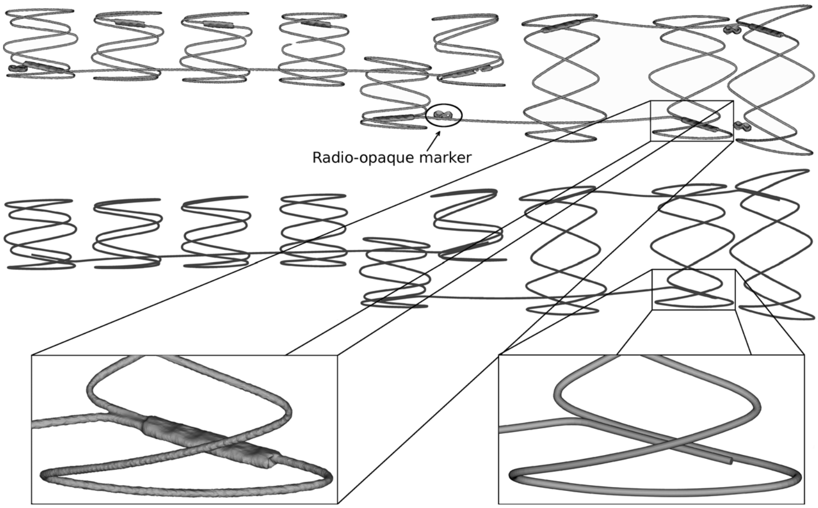

FIGURE 2.12: μCT (top) and FE (bottom) rendering of the Talent stent. Visible on the μCT are radio-opaque markers, gaps in the wires, and the clips that clamp the wires, which are not present in the FE model.

The graft model is not based on 3D imaging techniques, but on geometrical approximation. While the modelled graft will connect and tie the different stent rings in the same way as it does for the sample, notable simplifications exist.

- The PET grafts are sewed to the stent by hand. The graft is not regularly fitted to the stent. Loose fits or small pretensioned areas are frequently present, for all devices. The ePTFE of the Excluder fits the stent more closely, and the FE model of this device represents the sample best.

- The PET grafts are not made from one continuous fabric. They present multiple seams where the graft was closed. These are not modeled in the FE representations.

- The graft is sutured to the stent at discrete locations. Any slack or elasticity of these sutures is disregarded, where in the FE model, stent and graft are assumed to be rigidly tied.

Finally, concluding this chapter, it is noted that the geometrical representations of these commercial devices are based on a single sample, with unknown variability between samples.

CHAPTER 3

Mechanical testing and material characterization

The mechanical behavior of stent grafts has, to the best of our knowledge, never before been thoroughly examined by the scientific community. Material properties, assigned to parametric structures, have not been taken from actual stent graft nitinol material behavior. The following chapter aims to fill this gap, and employs a combined experimental and numerical method to examine stent graft material behavior. The mechanical response to a flat plate compression and radial crimping of the devices is derived and related to geometrical and material features of different stent designs. Finite element evaluations of the mechanical behavior match well with experimental findings and are used as a quantitative basis to discuss design characteristics of the different devices.

This chapter is based on: “Filling the void: A coalescent numerical and experimental technique to determine aortic stent graft mechanics” as published in the Journal of Biomechanics [129].

3.1 INTRODUCTION

Abdominal aortic aneurysms (AAA) are dilatations of the aorta between the renal arteries and the aortic bifurcation. This weakened bulge can continue to expand, increasing the risk of rupture, a life-threatening scenario. The pathology can be repaired through open surgery or, less invasively, by endovascular aneurysm repair (EVAR) with a stent graft

(SG). The endograft deployment technique and SG devices have advanced greatly in the last decade, yet they are still associated with long term problems, including graft migration or endoleakage [20, 21] and material failings [22, 23].

A large number of competing SG devices have been approved for use in Europe. This offers different treatment opportunities for vascular surgeons and patients, yet, it also brings a challenge, as choosing and differentiating between devices is not always straightforward. In general, published comparisons between stent graft outcome are sparse [130, 131] and difficult to relate to actual patient morphology.

A factor that generally lacks in device comparisons are differences in stent graft designs related to the overall mechanical behavior of the device, leading to differing biomechanical forces at the implantation site. Stent grafts need to be oversized to have enough radial force to enforce adequate graft-wall contact [53]. Amblard et al. (2009)[123] confirmed, using finite element analysis, that a decrease in radial force can induce type I endoleak, and that oversize could help prevent endoleakage. On the other hand, increased radial force could have adverse effects on the aortic neck such as wall degeneration and neck dilation [53]. Recently, Sincos et al. (2013) [132] demonstrated in a porcine model that larger oversizing of thoracic stent grafts can lead to increased injury to the aortic wall.

A report on the mechanical properties of stent graft devices can: (1) assist in the design of new devices; (2) support the processing and interpretation of clinical trial data, e.g. when relating neck dilatation to the specific radial force of each stent design and oversize; and (3) move forward numerical studies on stent fatigue [105], or fluid structure interaction [106, 123] to devices used in clinical practice. To our knowledge, there are no studies published investigating mechanical properties of clinically approved bifurcated aortic stent grafts.

In the present work, we use experimental and computational methods to assess and compare the behavior of the main body of 4 different SG designs: three nitinol based devices: Talent (Medtronic, Santa Rosa, Calif), Excluder (W.L.Gore and Associates, Flagstaff, Ariz) and Zenith LP (Cook, Bloomington, Ind) and one stainless steel device: Zenith Flex (Cook, Bloomington, Ind). Experimental set-ups are used to derive the mechanical response to a flat plate compression and radial crimping of the devices. Results from a computational modeling study are compared with the experiments to: (1) obtain the stent graft material properties via reverse engineering; (2) extend the loading range of the experimental radial crimp set-up and (3) extract the radial force for each individual segment. The use of 2 different experimental tests serves as a limited validation of the numerical method.

3.2 MATERIAL AND METHODS

3.2.1 Stent graft devices

Stent grafts in general feature a membrane of polymer material that is supported by a metal frame or stent. They are crimped into a delivery device, inserted via the femoral artery and then advanced into position in the aortic aneurysm, where they are deployed.

The SG devices investigated in this study differ greatly in design and materials used. All devices are self-expanding. The devices differ in method and location of fixation. Suprarenal fixation is achieved by bare (uncovered) stent rings. Active fixation is achieved by outward pointing hooks at the proximal side of the devices while passive fixation relies on radial outward force and friction for proximal fixation. Table 3.1 lists the characteristics of the different devices included in the study. The listed diameters are the diameters of the investigated samples. Devices were visually inspected and measured using a caliper. High resolution μCT scanning was performed to get the 3D geometry of all devices, as shown in chapter 2 of this thesis.

TABLE 3.1: Stent graft characteristics: stent material, graft material, fixation method, outer diameter, delivery system diameter and FDA status (March 2014) (1 Fr. = 1/3 mm).

	Stent	**Graft**	**Fixation**	**Diameter**	**Fr. size**	**FDA status**
Talent	Nitinol	Woven PET	Passive suprarenal	28 mm	22 Fr.	Approved
Excluder	Nitinol	ePTFE	Active infrarenal	26 mm	18 Fr.	Approved
Zenith Flex	Stainless steel	Woven PET	Active suprarenal	30 mm	20 Fr.	Approved
Zenith LP	Nitinol	Woven PET	Active suprarenal	30 mm	18 Fr.	Investigational

3.2.2 Mechanical testing

The 4 devices were first subjected to a flat plate compression test. Tests were performed at body temperature (37 °C) using an Instron 5944 electromechanical test system (Instron, Norwood, MA, USA) with a BioBox temperature controlled air chamber. The system was equipped with a 50 N load cell and two flat compression plates. The devices were compressed from their original diameter to 9 mm clearance between the plates. The complete main body of the device was tested.

The stent graft sections proximal to the bifurcation of all devices were subsequently subjected to a radial compression test, at body temperature. For this, a radial crimping head (MPT Europe, Leek, The Netherlands) was mounted on the electromechanical test system. The radial crimping head features an 8-segment iris to reduce the diameter of the inserted stent. The crimping head was limited to a maximum diameter of 22 mm. In this study, we were limited to one sample of each device. As they are self-expandable, one device can, however, be repeatedly mechanically tested without any permanent deformations. The devices were manually inserted into the crimping head and compressed to a diameter of 8 mm (nitinol devices) or 9 mm (stainless steel device) to avoid permanent deformations and material damage.

The first 2 segments of each device were inserted into the crimping head, as shown in figure 3.1. For the Excluder device, which consists of a continuous wire, the first 38 mm were inserted, until the start of the bifurcation. Unless specified differently, in all further use, diameters reported are those of the inscribed circle of the 8-segment iris.

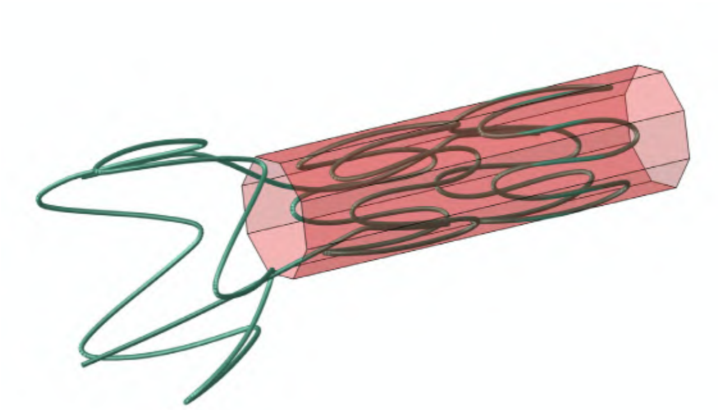

FIGURE 3.1: Example crimping of first two stent rings. Finite element rendering for the Talent device, fabric not shown.

3.2.3 Computational modeling

Finite element (FE) models of the metallic stents were reverse engineered from μCT scans. The wires were modeled using circular, linear Timoshenko beam sections. A comparison with solid elements was performed for a single segment, showing element type insensitivity for radial force, confirming previous results by Hall and Kasper (2006) [133]. The laser cut proximal stents of the Zenith LP device were modeled using rectangular beam sections. The graft covering the stent was added to the FE models by spline fitting circumferences of subsequent stent rings. The fabric was discretized with general purpose finite membrane strain triangular shell elements, using Simpson's rule for the shell section integration. In this study, shell thickness is reduced to have negligible bending stiffness. The choice for shell over (computationally more efficient) membrane elements was done to have a better contact behavior: membrane elements exhibit sharp folds between elements when compressed, causing difficulties in solving this already challenging contact problem. The covering membrane was connected to the stent frames using discrete, rigid connections.

A linear elasticity model was assigned to the stainless steel, with an estimated elastic modulus of 193 GPa and Poisson ratio of 0.25. This is consistent with wires used in medical devices of stainless steel alloys 302, 304LV or 316LVM [1].

The exact material properties of the nitinol devices are unknown. The superelastic behavior of nitinol was modeled using a material subroutine, available in Abaqus, based on the model described by Auricchio and Taylor (1997) [134]. In an isothermic environment, assuming a Poisson ratio of 0.3, it has 8 parameters that describe its material response (see Rebelo et al., 2001 [135] and Auricchio and Taylor, 1997 [134] and further in this chapter: table 3.5 and figure 3.3). Fabric materials were modeled using a linear elastic material, with assumed Poisson ratio of 0.3. Flat plate and radial crimp head were considered rigid. The FE calculations were performed using Abaqus/Explicit 6.12 (SIMULIA, Dassault Systèmes), in a quasi-static dynamic analysis with negligible kinetic energy (less than 5% of internal energy).

Compressing plates (flat and radial) were modeled as rigid surface elements, and moved in displacement control. Boundary conditions on the devices were: contact with these rigid plates, contact between stent struts and membrane, and self-contact between different stent struts and membrane elements. All contact was enforced using the penalty contact algorithm with finite sliding.

For the flat plate numerical simulation, one node of the device was fixed in the y and z direction (x being direction of compression), while for the radial crimp simulation, one node of the device was fixed in the z direction (xy being the crimping plane). This was done to avoid rigid body movement.

Compression force output (to be related with experimental output) were the discrete contact forces, integrated over the nodes of the compressing plate(s). The radial force exerted by each segment was calculated by summing only the force vectors at the location of that segment. For the continuous Excluder device, the radial force of the first 20 mm was separated for an easier comparison with the other devices.

In the flat plate compression simulation, the complete stent graft is modeled. In the radial crimp test, the unstressed parts are left out for computational efficiency. The stent segment adjacent to those being

---

[1] Technical binder Fort Wayne Metals. Retrieved from: `http://www.fwmetals.com/assets/files/FWM_TechBinder.pdf`

crimped is still included (see figure 3.2). For the Excluder device, the next 30 mm is included.

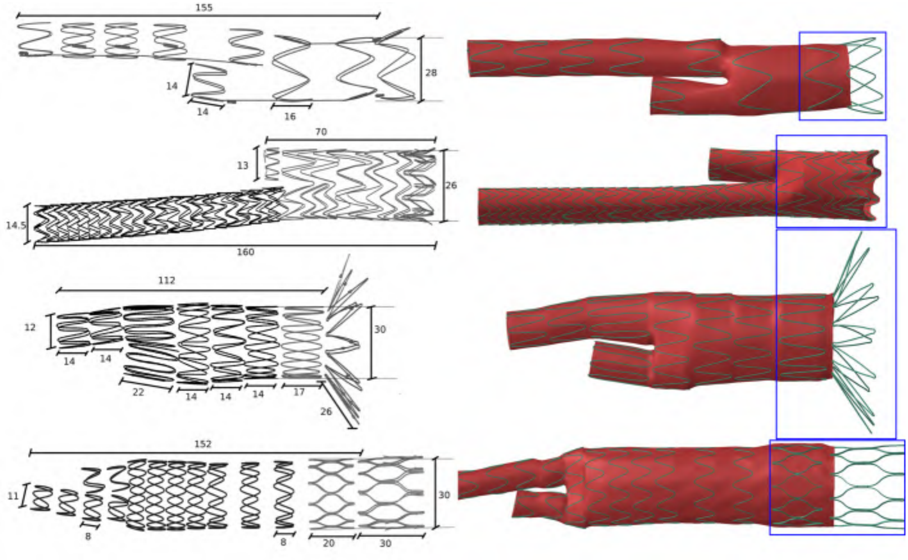

FIGURE 3.2: Surface rendering of CT scans of (top down) Talent, Excluder, Zenith Flex and Zenith LP. All dimensions are in mm. Similar rings are only dimensioned once. Total lengths are those of the covered part of the stent graft. Gray and black colors differentiate between wires of different thickness. On the right are finite element model renderings, including the graft material. The blue box indicates the segments inserted into the radial test set-up.

3.2.4 Parameter Study method

To assess the sensitivity of the simulations to the assumed dimensions, design parameters and finite element parameters, we first performed a sensitivity study to assess how the variability of these parameters and modeling assumptions influences mechanical response. The sensitivity study also ensured insensitivity of mesh density on the resulting forces.

Next, we used the results and experience obtained by this sensitivity study to estimate the material parameters of the actual devices (model calibration). Material properties were manually adjusted until finite element experiments reproduced both the experimental force-clearance (flat plate testing) and force-diameter (radial force testing) relationships. For the stainless steel stent graft, only the fabric parameters required calibration; all other stent grafts required calibration of both the nitinol and fabric model parameters. Simulation results for the stainless steel Zenith Flex device serve to some extent as a validation of the modeling approach, as computations are done with a priori known properties for the stainless steel wire frame.

When performing finite element modeling, automatically, assumptions are made regarding material and simulation parameters. It is good practice (F2514-08 - ASTM International, 2008) to assess the influence of these parameters on the solution results. Furthermore, in this study, the sensitivity study presented allowed an informed manual calibration of material properties to match experimental results.The sensitivity study is performed for the nitinol Talent stent graft. The following assumption was made a priori:

- Start of transformation stress in compression was assumed equal to the start transformation stress in tension, plus 200 MPa. This is based on the findings of Henderson et al. (2011) [136] for wire used in the Anaconda stent graft.

Table 3.2 shows the parameters that were adjusted from their original values, after calibration. From Kirchoff thin shell theory, doubling and halving fabric shell thickness while keeping stiffness (E-modulus times thickness) constant will multiply/divide bending rigidity by 4. In all radial crimping simulations, the stent was crimped using an 8 blade diaphragm, mimicking the experimental approach. The influence of this was investigated using a circular crimping tool, discretized with 60 segments over the circumference. The influence of the polymer fabric was investigated by simply leaving the shell elements out of the simulation.

TABLE 3.2: Adjusted material and simulation specifics in the parameter study, changes from original values. Numbers indicated between brackets are linked to figure 3.3.

Parameter	+	−
E-modulus fabric	$E - modulus \cdot 2$	$E - modulus/2$
Fabric thickness (constant stiffness)	$thickness \cdot 2$ $E - modulus/2$	$thickness/2$ $E - modulus * 2$
E-modulus austenite nitinol (1)	+5500 MPa (+10%)	−5500 MPa (−10%)
Start transformation (compression) (2)	Equal to start of transformation in tension	
No fabric	Removal of shell elements from simulation	
Tranformation plateau level (3)	+100 MPa	−100 MPa
Friction	0.5	frictionless
Wire thickness	10%	−10%
Circular crimping	Circular crimping instead of 8 plates	
Tranformation plateau slope (4)	100 MPa	10 MPa
E-modulus martensite nitinol (5)	+5500 MPa	−5500 MPa
End martensite transformation (6)	1%	−1%

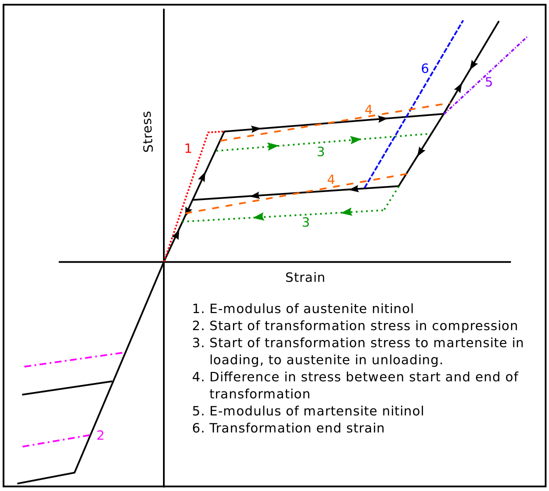

FIGURE 3.3: Visualization of the material parameter changes, shown on the nitinol stress train curve.

3.3 RESULTS

3.3.1 Stent graft geometry

Surface renderings of the CT scans and derived finite element models can be seen in figure 3.2. Diameters were measured at the most proximal part of the stent still covered by the fabric. For the Excluder, a completely covered stent graft, diameter measurement was done at the location of the hooks, disregarding the outward pointing hooks.

The stent grafts are mainly constructed from thin wire. An exception is the Zenith LP stent graft, with the top two segments laser cut from nitinol tube. These segments are approximately rectangular. Wire thickness and laser cut segment dimensions are noted in Table 3.3.

TABLE 3.3: Wire thickness (diameter; d) and laser cut dimensions (width; w and height; h) for all designs as measured by micrometer caliper. Proximal (gray) and distal (black) as indicated on figure 3.2

	Proximal dimension (gray)	**Distal dimension (black)**
Talent	Wire d=0.50 mm	Wire d=0.50 mm
Excluder	Wire d=0.32 mm	Wire d=0.26 mm
Zenith flex	Wire d=0.45 mm	Wire d=0.35 mm
Zenith LP	Laser cut w=0.25 mm h=0.5 mm	Wire d=0.36 mm

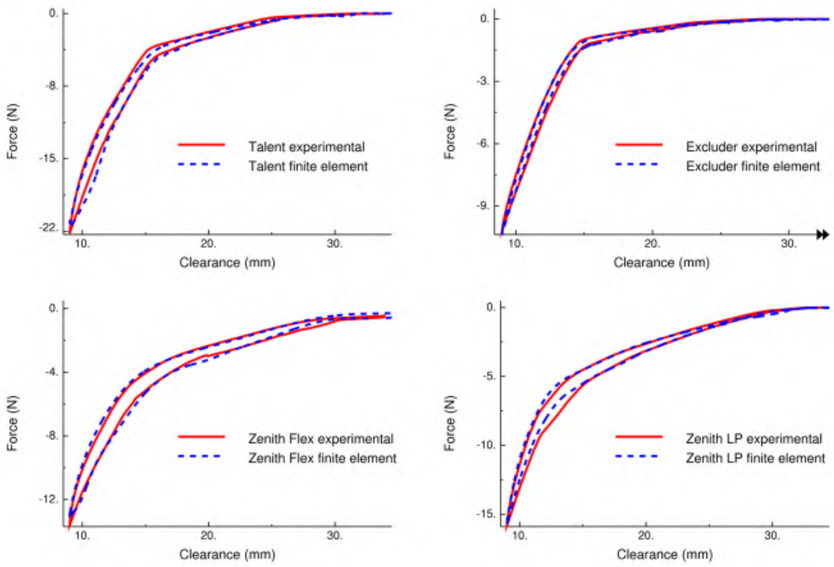

FIGURE 3.4: Flat plate compression curves for the investigated devices.

3.3.2 Mechanical tests: experiments and simulations

Figure 3.4 shows the results of the flat plate compression results, performed at 37°C. The Excluder device (26 mm diameter) requires the least force to compress to 9 mm clearance. In general, a bilinear result can be observed, with a steeper slope starting at the clearance where the iliac legs are coming into contact with the flat plates. Finite element results (after material calibration) match well with experimental data for all devices. The integrated force has the same magnitude for the top and bottom plate at each time increment (less than 0.1% difference), confirming the quasi-static nature of the simulation, i.e., low system inertia.

Results of the radial crimping test are shown in figure 3.5. Values for the integrated radial force during loading and unloading for 20 and 50% oversize are given in Table 3.4. The contribution of each segment (the first 20 mm for the Excluder) is given. Figure 3.2 displays the lengths of the segments (data is not rescaled).

By study design, again the finite element results overlap with experimental data. Experimental data for diameters larger than 22 mm are not available because of the limitations of the available experimental set-up. We note that at the given diameter of devices (figure 3.2), there is already a buildup of force caused by the outward flaring of the proximal

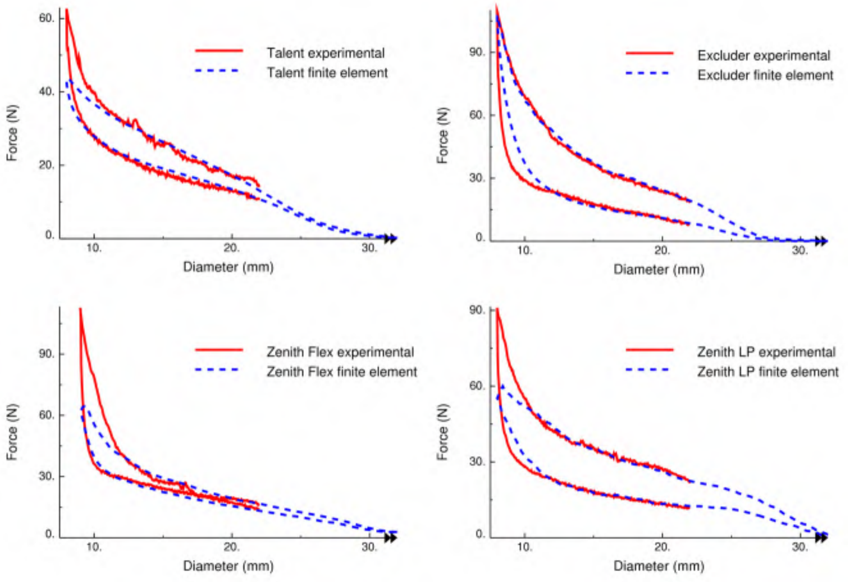

FIGURE 3.5: Force - diameter curves for the radial crimping response of investigated stent grafts.

TABLE 3.4: Radial force values at 20 and 50% oversize during loading and unloading, for the investigated devices

	20% oversize		50% oversize	
	Loading (N)	**Unloading (N)**	**Loading (N)**	**Unloading (N)**
Talent	10.1	8.7	20.1	15.1
proximal	5.7	4.8	8.9	7.0
distal	4.1	3.7	9.5	7.8
Excluder	20.0	8.8	30.0	13.3
prox 20 mm	14.4	6.1	21.5	8.3
distal	5.6	2.7	8.5	5.0
Zenith Flex	12.4	10.0	19.4	15.6
proximal	4.2	4.5	5.1	5.2
distal	8.1	5.5	14.1	10.3
Zenith LP	18.7	11.3	26.5	13.5
proximal	3.8	3.1	6.1	4.2
distal	14.7	8.0	19.2	9.0

segments of the stents. The finite element simulations and experiments start to diverge for low diameters (<12 mm).

Resulting material properties (after calibration) are given in table 3.5, 3.6 and 3.7. The parameter sensitivity study was performed on one device (Talent), and results are provided in figures 3.6 and 3.7.

TABLE 3.5: Nitinol material properties for the Talent, Zenith LP and Excluder devices.

	Zenith LP	**Talent**	**Excluder**
Austenite elasticity (MPa)	44000	55000	38000
Martensite elasticity (MPa)	35000	35000	35000
Transformation strain	0.05	0.05	0.05
Start of transformation loading (MPa)	450	600	450
End of transformation loading (MPa)	530	680	530
Start of transformation unloading (MPa)	250	380	150
End of transformation unloading (MPa)	200	330	100
Start of transformation in compression (MPa)	650	800	650

TABLE 3.6: Stainless steel material properties for the Zenith Flex device.

	Zenith Flex
Elasticity (MPa)	193000
Poisson's ratio	0.25

TABLE 3.7: Graft material properties for all devices

	Zenith LP	**Talent**	**Excluder**	**Zenith Flex**
Elasticity (MPa)	6000	1800	4000	2400
Thickness (mm)	0.02			

3.3.3 Parameter study

Figure 3.6 shows the results of the flat plate solution sensitivity study. Figure 3.7 shows the results of the radial crimping solution sensitivity study. Results for the grayed out parameters in table 3.2 are not shown, as they did not have a significant effect on the resulting force. Table 3.8 gives a concise summary of solution sensitivity for the investigated parameters.

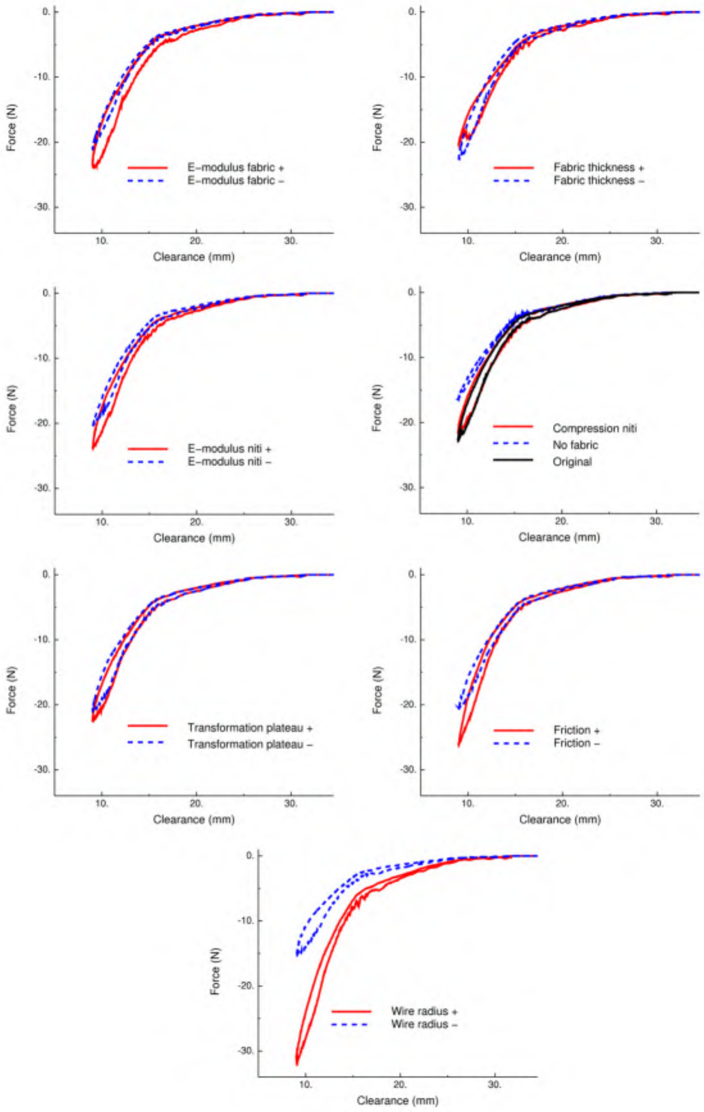

FIGURE 3.6: Force - clearance curves for the flat plate compression parameter study.

Based on these findings, and realistic values for nitinol [105, 137] the following values were used:

- Difference in stress between start and end of transformation (the slope of plateau) was assumed to be 80 MPa in loading and 50 MPa in unloading.
- The end martensite transformation strain was assumed to be 5%.

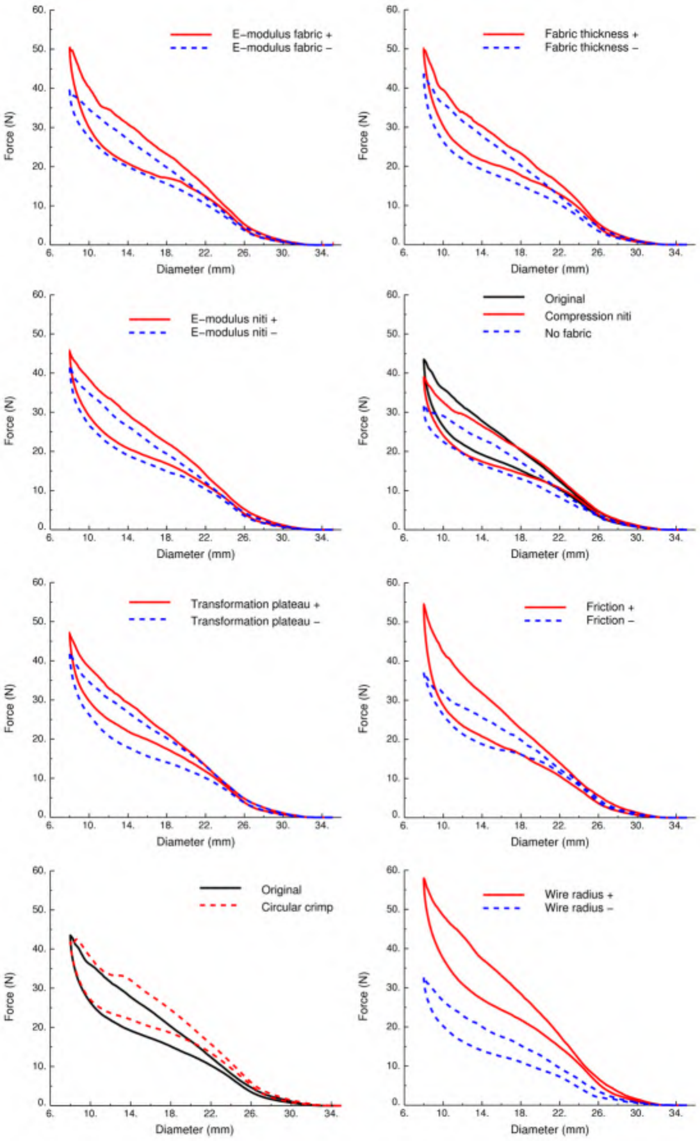

Figure 3.7: Force - diameter curves for the radial crimping parameter study.

- Martensite elasticity was assumed to be 35000 MPa.

Based on the findings and previous reports in literature (Petrini et al. 2005[138]: used a friction coefficient of 0.05 for a flat plate compression simulation)

- Friction was assumed to be relatively low, and set at a factor 0.1.

Table 3.8: Concise summary of solution sensitivity for the investigated parameters.

	Flat plate	**Radial Crimp**
Fabric thickness	Limited influence	Magnitude
E-modulus fabric	Hysteresis and magnitude	
E-modulus austenite nitinol	Magnitude	
Transformation plateau level	Limited influence	Magnitude
Start of transformation (compression)	Limited influence	Limited influence in ROI
Friction	Limited influence at low force Magnitude at high force	Limited influence at low force Hysteresis and magnitude at high force
Circular crimping	N.A.	"Right shift" of curve
No fabric	Hysteresis and magnitude	
Wire thickness	Hysteresis and magnitude	

Following influences were observed:

- Force hysteresis, the area within the force loop, is mainly influenced by the fabric and friction.
- Fabric thickness reduction did not influence the results at all, as thickness was previously chosen to have negligible shell bending rigidity.
- For flat plate compression, of all nitinol material parameters, only the austenite elastic modulus has a noticeable influence on results. As the nitinol wires during flat plate compression are not strained above 2%, this behavior is expected.
- For low radial compression, until 22 mm diameter, the nitinol material has not reached the plateau stress, and only austenite elasticity influences the results.
- Wire thickness did, as anticipated, greatly influence the results as, from elementary beam theory, bending stiffness is proportional to the radius to the fourth power.
- Friction only influences the solution significantly when high enough forces, and more contact, come into play.

3.4 DISCUSSION

The presented work details the mechanical behavior of 4 commercially available stent grafts, expressed via the behavior in flat plate and radial compression tests. As assessment of radial force is a requirement for FDA approval, device manufacturers are likely to have this data on file. To our knowledge, this is the first report of the radial force of commercial, aortic stent grafts in a peer reviewed journal. Oshin et al. (2011) [100] measured the circumferential spring stiffness of a V-shaped segment of a Cook Zenith fenestrated stent graft by removing the stent from the fabric and cutting the ring. The stiffness of 0.4 N/mm translates to a radial force of 7.5 N at 20% oversize. This is very similar to our finding for the distal segment (8.1 N).

Kleinstreuer et al. (2008) [105] performed a finite element radial force measurement for a stent with diamond cells, neglecting the covering membrane in compression. For the specific geometry, with length 9.5 mm, investigated they report a radial force of 6 or 4 N to achieve 50% oversize, depending on the used material properties. When rescaled to the lengths of the devices we tested, this falls within the range we report in Table 3.4.

From the data reported, some observations can be made. Although the Zenith Flex device is made from the stiffer stainless steel, it shows a low radial force in radial compression at a clinically relevant oversize (10 - 20%, Cook Zenith Instructions For Use). Twelve V-segments over the circumference, and relatively long struts of the top stent make it radially flexible. The Excluder has an opposite design strategy: the flexible nitinol wire, of a relatively low diameter, is helically wound, with short strut lengths and an average number of peaks, achieving a high radial force over a limited length. The Zenith LP also exerts a high radial force in the sealing zone (the distal, covered segment) because of its specific sigmoid laser cut design.

When crimped to a low diameter, the number of in-folding struts making self-contact cause the radial force to peak. This behavior can also be seen in the Zenith LP (10 segments over the circumference) and Excluder (8 peaks, helically wound), while it is almost absent in the Talent device (5 peaks). A higher force increases the risk of material (suture, fabric or stent) damage during this crimping phase. We speculate that this risk is removed during production of these commercial devices by cooling of the nitinol material, purposely folding the struts in an optimal pattern and an extensive quality control.

Radial force is one of the important mechanical characteristics of stents and stent grafts. The stent graft needs sufficient radial force to have enough fixation (passive or active). Contrariwise, an excessive radial force may trigger aneurysm neck dilatation and, in the long term, device migration [53] or aortic wall damage [132]. With this in mind, stent designs that offer a high radial strength at the sealing location, but lower radial force at the suprarenal fixation would have, from a mechanical point of view, a better long term outcome. This speaks in favor of the Excluder (no suprarenal forces), and Zenith devices (with low suprarenal force), while the Talent device needs the suprarenal force for a good migration resistance.

The long struts of the Zenith devices do cause the proximal segments to be longitudinally stiff, possibly exerting higher forces to the arterial wall when deployed in angulated (suprarenal) necks. However, vascular surgeons have reported to find the stiffness of the proximal stent of the Zenith device to be advantageous in angulated necks to achieve good apposition and fixation [49].

3.4.1 Parameter study

An important conclusion of the parameter study is that the covering polymer fabric influences both radial and flat plate compression results. Indeed, for flat plate compression, the fabric is the main source of hysteresis of the force loop. And in both flat plate and radial loading, a stiff polymer will increase the force required for compressing the stent graft. As such, results concerning radial force from studies ignoring the membrane should be interpreted with caution [105, 106, 139], as they can underestimate the force by 10 to 30%.

The membrane has an influence on the radial force as it limits the motion of the stent during deformation. From our findings, there are two main types of stent deformation inhibitions that contribute to this. We graphically show and explain these basic concepts in Figure 3.8. Radial compression compresses the V-segments of the stent, i.e. reduces the angle of the “V”. The stent strut lengths however, remain approximately the same length. When two subsequent stent rings have a mirrored position, we have situation as shown in figure 3.8, where the fabric between the stent rings gets stretched as the stent is radially compressed. In a flat plate compression, a different effect is observed. As the stent ring becomes more oval, because of the one sided compression, the circumference of the stent graft remains the same. A chord, connecting two points on the flattened side of the stent graft, does elongate during flat plate compression. A consequence of this is that, considering that this chord can be the graft connection between two “valleys” of the stent ring, this graft will experience an elongation. This is again schematically represented in figure 3.8. Different stent graft designs and more complex loading will show more complex tensioning of the membrane component.

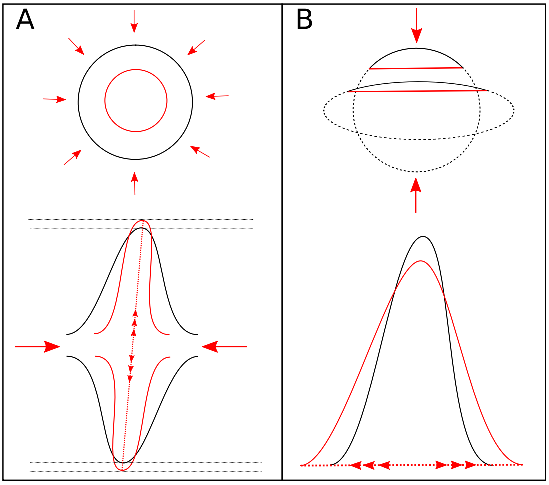

FIGURE 3.8: Schematic representation on how the graft influences radial force and flat plate results.

The use of 8 plates to crimp the device also influences the result, as the diameter difference between the inscribed and bounding circle is, by simple geometrical analysis, a factor 0.924. When using a larger number of segments to better describe a perfect circle, this factor increases, causing an imperfect "right shift" of the curve. This is an important consideration to keep in mind when mimicking experiments with finite element simulations. Also when performing in vitro testing, operators should be well aware that the bounding or inscribed circle are both different from the corresponding perfect circle with the closest force diameter behavior, which will have a diameter in between. This corresponding circle will be different depending on the stent design and the number of plates used to crimp the device. When comparing with a corresponding circle, e.g. the average between bounding and inscribed circle, the 8 plate radial compression will, at high diameter, overestimate the force, as the stent contacts the plates first. At low diameter and high crimp, the 8 plate test will underestimate the force, as the devices move to the corners of the crimping polygon.

Consequences for manual material calibration and validation method

From this analysis, material calibration started using the stainless steel device (Zenith Flex) and the flat plate compression experimental test. Indicated in green in table 3.8 are factors that have no, or limited influence on the resulting force. With known wire thickness and, for the stainless steel device, known elastic modulus of the device, only 1 material parameter remains - fabric elasticity.

This parameter influences both hysteresis and magnitude of force. This served as a first validation of our method, as calibrating the fabric elasticity for magnitude of force also gave a good result in force hysteresis (figure 3.4). Furthermore, using this elasticity and other, known, parameters gave a good fit between experimental and simulated radial crimping.

From the parameter analysis, we also know that friction only changes the result at higher forces. For the Zenith Flex, the experimental and simulated flat plate test gives a good match during the entire compression. Consequently, the chosen friction of 0.1 is acceptable. We note that the difference between frictionless and 0.1 is minor, only at higher friction the deformation patterns change considerably. For all stents, this friction coefficient is assumed equal.

For the nitinol devices, two unknown material parameters exist: nitinol and fabric elasticity. They were manually calibrated, changing fabric elasticity to match the hysteresis and nitinol elastic modulus to match force magnitude of the flat plate compression test. Transformation starting stress was then obtained by comparing simulated and experimental radial crimping tests. For high radial compression, we did not expect, or attempted to capture the radial force peak caused by complex (self) contact and deformations. The mismatch between simulation and experiment is discussed in the next section.

Investigating the sensitivity of the solution to different parameters in our finite element simulations allows us to assess the influence of manufacturing tolerances, e.g. on wire thickness and material parameters on the mechanical behavior of devices. It also demonstrates the applicability of FEA to fasten the design cycle of medical devices. Furthermore, specific to this study, it allowed us to perform an informed manual calibration of material properties, needing a relative low number of iterations to achieve a good fit. An important modeling aspect for an accurate description of radial force is the inclusion of the fabric material for these covered devices. We show that an experiment using a segmented radial crimp tool causes a “leftshift” of the force-diameter curve. This should be kept in mind when comparing different experimental setups. Finally, using the result of this parameter study, we verified that our validation method, using the stainless steel stent, is not muddled by confounding effects.

3.4.2 Modeling simplifications and study limitations

Modeling these complex, composite devices is not trivial, and some modeling abstractions and simplifications were made. The membrane material properties and thickness given in the tables are those obtained after optimization of material parameters. They should be treated as measures of the fabric stiffness (intrinsic elasticity of the material multiplied by the thickness). These values are obtained by ensuring similar mechanical responses between experiments and devices. As such, the values shown take into account polymer thread stiffness, stiffness of the sutures between fabric and stents (modeled as rigid connections) and differences in geometry between the samples and stents (i.e., small folds or loose areas). We believe this is a reasonable simplification, as modeling all these features individually is not practical and equally prone to error. It does mean, however, that comparing membrane properties to e.g. values in literature or the properties of bulk material is not meaningful. Note, however, that because of this approach, assessment of stresses in the graft material during radial crimping or other loading would be highly inaccurate.

Modeling simplifications also lead to a discrepancy between finite element and experimental radial force results at high crimping (visible in figur 3.5). The artificially reduced membrane thickness, coupled with complex (self) contact between membrane and stent causes an underestimation of the force required to tightly compress these devices. Additionally, the sutures tying graft and stent have, approximately, the thickness of the graft material. Neglecting these features also causes an underestimation in radial force at low diameter. To investigate the force or stress and strain in the material at high compaction, more complex modeling would be needed to capture folding patterns and complex (self) contact behavior.

Material properties for the wires used in these commercial stents have not been reported, except for the Talent device. In a different study [140] (chapter 5) we report an austenite elastic modulus of 35,850 MPa, while here we report a value of 55,000 MPa. As discussed in De Bock et al. (2012) [140], the small sample length used in that study could have caused an underestimation of the elastic modulus. More importantly, the uniaxial tensile test was performed at room temperature, which can explain this mismatch in results [137]. Note that the elastic modulus mentioned in this study is not the modulus inherent to the austenite nitinol phase, but the modulus fit to the material model of nitinol [134].

Quantification of strains in the stent wires is achievable using the method presented. Stent fractures have been widely reported, and could lead to type I or III endoleak, or a perforation of the aortic wall [141]. The modeling could therefore assist in fatigue risk assessment for abdominal SG and related devices. However, some inaccuracies remain: Firstly, the discrete connections between stent and graft could locally cause peaks in stress and strain. Preliminary investigations (not reported) indicate that, for the devices and deformations investigated, this is not the case for the nitinol wires, only for the fabric. Secondly, and more importantly, from physical inspection it is clear that certain rings are pretensioned for some devices (mainly the Talent). This means that they are constrained by the graft material and would, if cut loose, slightly open up further. In other devices this behavior is less pronounced or absent, yet in our view, this represents an important parameter for fatigue assessment, especially concerning the mean strain as used in constant life diagrams [142]. This topic deserves further investigation and more data on the manufacturing process, and is beyond the scope of this study.

By design, our method was validated in two ways. First, simulations of the stainless steel Zenith Flex device with assumed stainless steel material properties, allowed for a direct comparison between experimentally observed and simulated mechanical behavior of the device. Secondly, the use of two independent experiments to calibrate the material, further affirmed our modeling method, as during flat plate compression, the nitinol stress transformation parameters do not influence the result.

3.5 CONCLUSIONS

The presented study quantitatively documents the mechanical response of 4 commercially available stent grafts to a flat plate and radial crimp loading. Experimental and computational methods were used and combined and allowed us to provide radial stiffness and forces of the devices studied. Redundancy in the number of experiments, and known properties of stainless steel served to validate the methodology. Complex hybrid finite element models were used to conduct a solution sensitivity study, and highlighted the importance of including the stent fabric in the simulations to achieve realistic finite element simulations of stent graft devices undergoing flat plate and radial crimp loading. Further clinical or animal studies on the adverse, long term, effects of stent graft forces on the aortic wall could assist in determining an optimal value of radial force, and further assist in device selection and sizing.

Chapter 4

A mechanical insight into stent graft Instructions For Use in angulated proximal aneurysm necks.

Endovascular treatment for patients with a proximal neck anatomy outside instructions for use is an ongoing topic of debate in endovascular aneurysm repair (see section 1.2.4). This chapter employs the finite element method to offer insight into possible adverse effects of deploying a stent graft into an angulated geometry. The effect of angulation, straight neck length and device oversize was investigated in a full factorial parametric analysis. Stent apposition, area reduction of the graft, asymmetry of contact forces and the ability to find a good seal were investigated. Most adverse effects are expected for combinations of high angulation and short straight landing zones. Our analysis showed that for an angle between the suprarenal aorta and proximal neck above 60°, proximal kinking of the device can occur. The method used offers a engineering view on the morphological limits of EVAR for a clinically used device.

This chapter is based on: "What if you stretch the IFU? A mechanical insight into stent graft Instructions For Use in angulated proximal aneurysm necks." submitted for publication in Medical Engineering & Physics.

4.1 Introduction

Endovascular aneurysm repair (EVAR) has emerged as a safe alternative to open surgical repair for treatment of abdominal aortic aneurysms

(AAA). The technique has shown benefits in terms of operational mortality and hospital stay, and late results comparable to conventional surgery [36]. However, EVAR may not always be the best treatment option. An unfavorable aortoiliac morphology, especially related to the proximal neck, could restrict the use of EVAR. In particular, short and/or severely angulated aneurysm necks can complicate the endovascular procedure, or increase the risk for late, device-related complications [45].

Device manufacturers have identified certain anatomical requirements for the proximal neck. These instructions for use (IFU) are based on bench top engineering tests, preclinical and animal tests and early phase clinical trials. Most device IFUs state that the aortic neck should be greater than 15 mm in length and have an angulation less than 60°. Although there are many reports on the adverse effects for *off label* use [45–47, 143], some authors report comparable mid-term outcomes between patients with favorable and hostile aneurysm necks [48, 49]. With this study we aim to incorporate an engineering view on the morphological limits of the proximal sealing zone, as data on the mechanical side of the problem have been limited.

In a bench top in vitro test, Albertini et al. (2001) [94] used a silicone flow model and a custom made stent graft to investigate fluid leakage under different stent angles. Some computational studies have touched upon the subject. Prasad and colleagues [106] proposed a framework to determine the positional stability of aortic endografts. In the study, Computational Solid Mechanics (CSM) and Fluid Dynamics (CFD) are combined to determine contact properties (using CSM) and loads imposed by the blood flow and pressure (using CFD). The framework was used to investigate the effect of neck angle, length and device oversize for six cases: an angle of 0 and 16°, sealing length of 22 and 5 mm, and 10 and 15% oversize. The additional (lateral) load caused by a curved aneurysm neck had been previously demonstrated using CFD [116, 144]. Demanget and colleagues[107] performed a computational and experimental bending of iliac limb stent grafts. They demonstrated a device specific bending behavior and reduction in area for angles up to 180°for unconstrained devices.

In the presented study a “third generation” commercial stent graft (Zenith LP, Cook Bloomington, Ind) is virtually deployed in idealized geometries, using a CSM finite element method. Proximal neck angle, sealing location and degree of oversize are varied. Different output parameters, related to positional stability, are calculated from the CSM result.

4.2 MATERIAL AND METHODS

4.2.1 Stent graft

The stent graft device is made from series of nitinol z-stents in the graft body and iliac legs. The two top stent segments, making contact with the proximal neck, are laser cut from nitinol tube. A woven graft material is sewn to the stent segments. The stent graft is self-expanding, features an uncovered top stent ring with active fixation. The stent graft has a diameter of 30 mm, and the uncovered and first covered stent segment measure 30 and 20 mm respectively. 3D geometry and mechanical behavior of the device was obtained from a previous study [129].

4.2.2 Idealized vessel geometry

In the study, an idealised proximal neck geometry was used. The centerline of the vessel constisted of two angled, straight lines of 60 mm. The angle was rounded with a 15 mm fillet. This centerline was swept with a circle to create the vessel wall.

The proximal neck model was given linear elastic material properties, with a Young's modulus of 1.2 MPa, and a Poisson's ratio ν of 0.495, while vessel thickness was assumed constant at 1.5 mm. These material properties are in line with the standard FDA protocol (ASTM Standard F2477) [105]. The effect on the outcome parameters when deployed in a stiffer AAA neck (e.g. a calcified neck) was investigated by calculating a subset of the full parametric design with an aortic elastic modulus of 12 MPa. It is assumed that the effect will be the largest for the highest oversize, and only these cases are investigated.

As the study focusses on the proximal neck region, the model did not have an aneurysm region. This was done for computational efficiency, as it allowed to reduce the model to half of the stent graft, using the vessel to guide the device along the intended angle.

4.2.3 Computational modeling

Finite element calculations were performed using Abaqus/Explicit 6.12 (SIMULIA, Dassault Systèmes), while pre- and post-processing was done using pyFormex (http://www.pyformex.org). For the stent graft device, the same modeling strategy as in [129] was followed. The first two lasercut segments were modeled using rectangular beam sections, the wires using circular beam sections. The stent is made of nitinol. The superelastic behavior of this shape memory alloy was described by the constitutive model of Auricchio and Taylor [134], available as a user material subroutine in Abaqus. The graft material was modeled using triangular shell elements and a linear elastic material model. Material properties and dimensions are shown in table 4.1.

TABLE 4.1: Material and dimensional properties for the finite element stent graft.

Dimensional variables	Zenith LP
Lasercut stent width	0.25 mm
Lasercut stent height	0.50 mm
Wirestent diameter	0.36 mm
First lasercut stent length	30 mm
Second lasercut stent length	20 mm
Wirestent length	8 mm
Diameter	30 mm
Nitinol variables	
Austenite elasticity (MPa)	44000
Martensite elasticity (MPa)	35000
Transformation strain	0.05
Start of transformation loading (MPa)	450
End of transformation loading (MPa)	530
Start of transformation unloading (MPa)	250
End of transformation unloading (MPa)	200
Start of transformation stress in compression (MPa)	650
Graft variables	
Elasticity (MPa)	6000
Thickness (mm)	0.02

A computational procedure was devised to mimic the endovascular procedure. The simulation consisted of four steps, visualized in figure 4.1:

1. A cylindrical, rigid surface was placed outside the device. The radius of this surface was reduced and, because of contact between this cylinder and the stent graft, the device is crimped. Final crimping diameter was 16 mm, which is larger than the clinical delivery diameter. It was determined that crimping further did not influence the final finite element result, and the larger crimping diameter could be used to shorten computational time.

2. The cylindrical sheet was bent along the centerline of the vessel, forcing the stent graft to follow the curve. This was achieved using

a user-subroutine-defined boundary condition, giving analytical displacement values through the Abaqus Fortran interface. During crimping and bending, the most proximal apices of the stent were fixed in the axial direction.

3. The body of the stent graft is expanded by removing the cylindrical rigid surface. During this deployment, the most proximal apices of the lasercut, uncovered stent remain fixed. This mimics the actual deployment of this device, which allows for small corrections and some maneuverability, before releasing the top stent and engaging the hooks.
4. The apices of the uncovered stent are released, completing the procedure.

The contact algorithm used was a surface to surface penalty contact with finite sliding. Contact between the crimping/bending tool and the device was assumed frictionless. All (self) contact between and among device components was also assumed frictionless. Friction between the vessel and stent graft was set at 0.2 to limit slipping.

In total, 72 simulations were performed in a full factorial simulation strategy. Three geometrical parameters are independently varied:

1. **Diameter**; vessel diameter was adapted to have 10, 20 and 30% oversize of the stent graft: diameters of 23.08, 25.0 and 27.27 mm.
2. **Angle**; neck angle was increased from 20°to 80°in 4 steps: angles of 20, 40, 60 and 80°were considered.
3. **Position**: the vessel was moved in the axial direction, shortening the landing zone of the device in the straight part, i.e. before the curve. The starting position had a covering length of 21 mm (the length of the second lasercut, covered stent + 1 mm) and was moved in 7 mm steps: 0, 7, 14 and 21 mm down. The vessel was moved two more steps: 28 and 35 mm down. In these cases, there was a *negative* straight landing zone. This was done to change the angle under investigation from the infrarenal angle β, the angle between the infrarenal aorta and aneurysm, to the suprarenal angle α, the angle between the suprarenal aorta and infrarenal aorta (see figure 4.2). This is a purely conceptual difference, and does not change the simulation strategy or post-processing, and is only relevant in discussing the outcome and relating to clinical reality. In all further analysis these two anatomically different locations are investigated separately. To be intuitively consistent with the

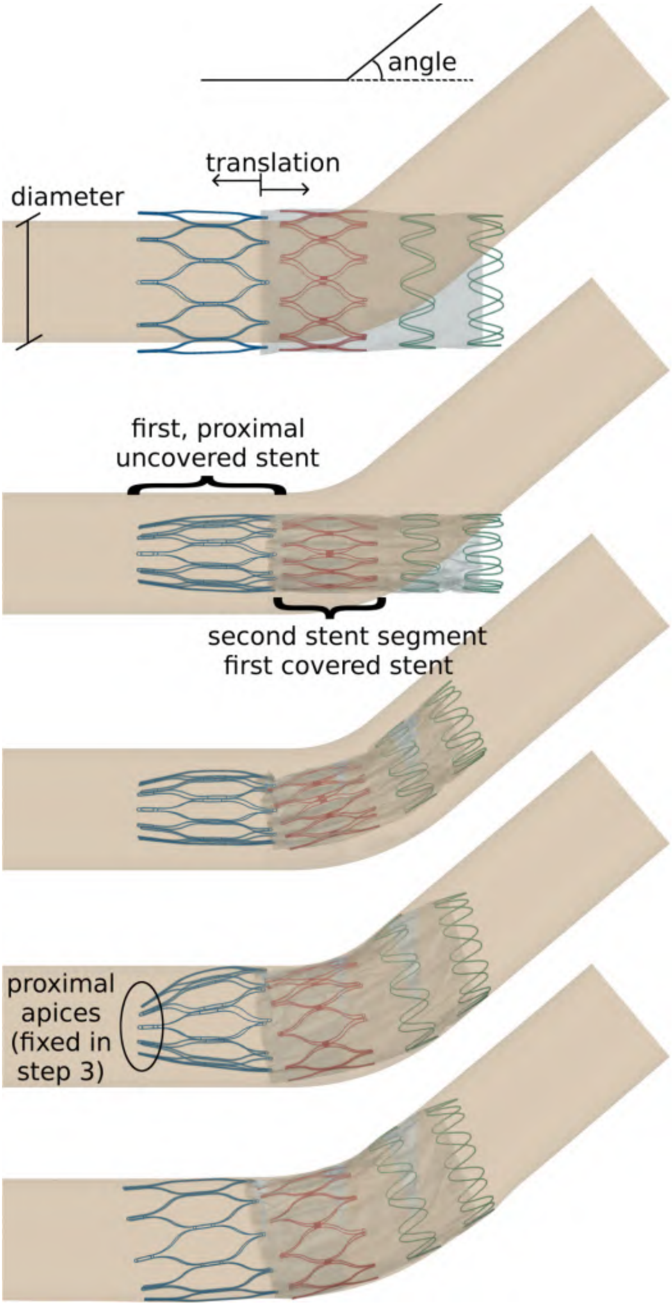

Figure 4.1: Finite element deployment procedure: 1. The stent is reduced in diameter and 2. bent to the vessel curvature 3. The distal part of the device is expanded while the most proximal apices remain fixed. 4. The entire device is deployed.

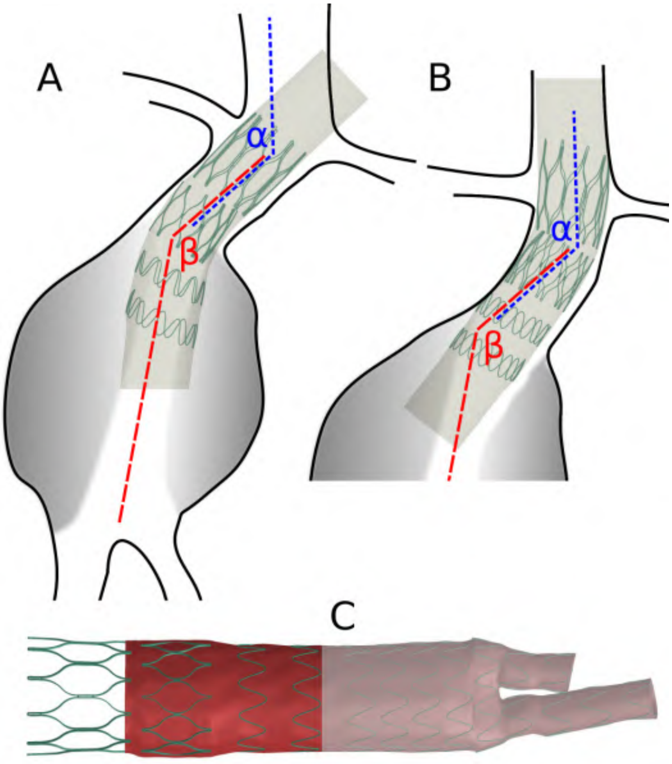

FIGURE 4.2: Location of the α and β angles. For position values of 0 - 21 mm, the β angle is investigated (A), for position values 28, 35, the α angle is examined, and the device again has a straight landing zone (B). The simulation result is overlayed with a conceptual sketch of an aneurysm geometry. Stent graft membrane is not shown. The complete Zenith LP device is shown (C). Only the opaque part is used in the finite element calculations.

other parameters (higher being worse), notation was as follows: 0 (21 mm straight landing zone), 7, 14, 21 (0 mm straight landing zone), *28*, *35 (α angles)*.

4.2.4 Post-processing

The goal of the study was to investigate device behavior in different proximal neck morphologies. In addition to the qualitative deformation output from the finite element simulations, we formulated and developed output parameters that could serve as measures of positional stability and could be related to the risk of complications during or after intervention.

- **Stent strut apposition**. The deformed configuration after finite element simulation was exported into *pyFormex*. The distance between the top two stents and the vessel wall was calculated for each beam segment. For comparison, the average distances to the vessel wall for each of the two stent segments were considered.

- **Lumen area reduction**. The deformed vessel and stent graft covering membrane were processed to calculate the lumen area reduction. The 3D geometries were sliced every 1 mm, along the length of the centerline, perpendicular to the centerline. This resulted in a series of 2D polygons. The percentage reduction of lumen area was calculated:

$$1 - \frac{Area_{graft}}{Area_{vessel}} \tag{4.1}$$

  The maximum area reduction was used for analysis.

- **Force asymmetry**. Inserting a stent graft into a curved artery causes an asymmetric loading, and can be conceptually compared with a three point bending test: the proximal and distal straight ends are pivots, while the inner angle acts as a pusher. To quantify the amount of asymmetry, the contact force is used. The vessel was split over the length, and divided in a top and bottom half (see Figure 4.3). For each longitudinal segment, the summed forces of the top and bottom half were compared. The asymmetry measure was defined as follows:

$$\sum_{i=1}^{n} \frac{|Force_{top} - Force_{bot}|}{Force_{bot} + Force_{top}} \bigg/ n \tag{4.2}$$

- **Complete circumferential sealing** In order to avoid endoleak (blood leaking into the aneurysm sac), a complete seal over the circumference of the vessel is needed for a successful endovascular procedure. To quantify this seal, the vessel was divided, longitudinally and circumferentially, into patches. The average contact force for each patch was calculated from nodal output. The patchwork allowed to project the 3D geometry onto a 2D grid. Using an A* path finding algorithm[145], a path along the circumference was searched, only connecting patches with an averaged force above 0. The path was restricted to the second lasercut stent, which is covered with the graft membrane. The heuristic used is the distance traveled, while the move cost was set to *1* in the circumferential direction and *100* in the longitudinal direction. This allowed to quantify the amount of "sidesteps" needed to find a path. A visual explanation is given in Figure 4.3. The size of the patches was chosen to get a good spread in results among all simulations, as larger patches make it easier to find a path, and vice versa.

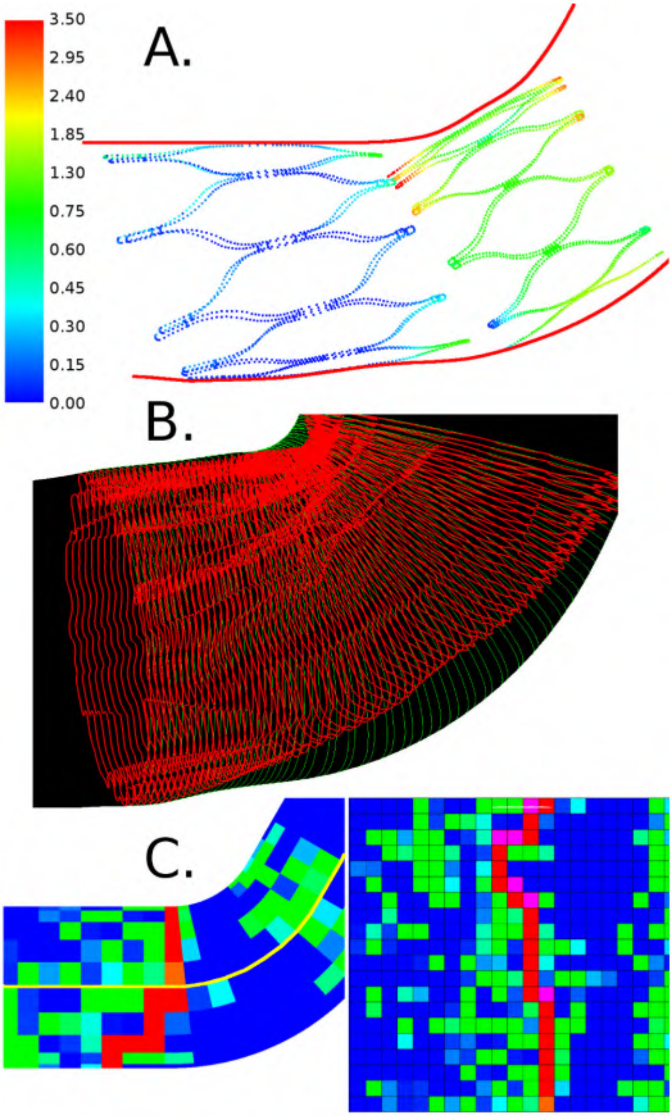

FIGURE 4.3: A. Visualisation of stent strut apposition for an oversize of 20%, angulation of 60°and translation of 21 mm. The color scale is bilinear and shows the distance to the vessel wall in mm.

B. Visualisation of area reduction calculation for an oversize of 20%, angulation of 80°and translation of 7 mm. Resulting value is an area reduction of 0.35

C. An example of a found path (red) in a patchwork projected on the vessel (left) and a cartesian grid (right). Blue to green colors indicate the averaged contact force. The orange square shows the starting position. In pink (on the bottom right figure) steps in the longitudinal direction (with cost *100*) are indicated, total cost for this example would be *619*. The yellow line on the left picture shows the split between top and bottom half used in the force asymmetry index.

Output from postprocessing was analyzed qualitatively using 3D bar plots. Using the statistical package R [146], a multivariate regression model was fit to the data using a least squares method. Although this fit could be used for interpolation purposes, the purpose of the analysis in this work is to estimate the association between predictors and responses, and assist in the discussion. To be consistent between responses, the regression fit was once performed with all three predictors, and once with three predictors and three interactions. Finding a sealing path and the cost associated is, in contrast to the other output parameters, not a continuous variable but an ordinal dependent variable and, consequently, we employed a proportional odds model to discuss trends.

4.3 Results

As it is not feasible to show deformed configurations for 72 simulation results, figures throughout the paper, illustrating methods, post-processing and results, are shown for different geometries with different parameters. These parameters are indicated in the captions of each figure.

4.3.1 β angle

The following sections discuss the finite element results when the β angle is under investigation, i.e. when the axial translation is between 0 and 21 mm. The uncovered stent lies in the straight part of the geometry, while the second lasercut stent has a straight landing zone length of 21 to 0 mm, respectively.

Stent strut apposition

The average distance from the stent to the vessel wall shows the same trend for both lasercut stent segments. Both bending angle and translation negatively impact the apposition values. From a multivariate linear regression analysis (supplementary data to this thesis), we find that for the distal segment (figure 4.4), the bending angle has the largest influence. The first segment lies in the straight artery, before the curve. Not surprisingly here, the translation has an increased influence on the average distance to the vessel wall, roughly the same as the angle (figure 4.4). High values for this uncovered stent are only seen with a translation of 21 mm (0 mm straight, covered, landing zone). Diameter is not a significant contributor to the apposition.

When considering interactions between parameters, we get more insight on why the regression analysis does not capture a diameter effect. For relatively straight artery segments, a high oversize (low diameter) wrinkles the membrane, increasing the distance to the vessel wall. At higher angles and with the stent closer to the curve, the higher oversize, and consequently higher force, helps the device in apposing better. In figures 4.4, this is also visually clear: for an angle of 20°, the average distance to the vessel wall is higher for high oversize (dashed line) compared with low oversize (dotted line), while for an 80°angle, the opposite is true.

Area reduction

From the linear regression analysis, only the angle significantly influences the area reduction. The maximum area reduction occurs where the membrane is not supported by the nitinol stents: either at the gap between the two lasercut stents, or between the second lasercut and first wirestent.

At 7 mm translation, the unsupported membrane between second lasercut and first wirestent is located at the angle in the vessel. As seen and indicated in figure 4.5, for 10 and 20% oversize, this resulted in a larger area reduction, even when compared with cases with smaller neck lengths.

Similar to the apposition output, diameter has an interaction with the angle, where the wrinkles at high oversize dominate the area reduction for

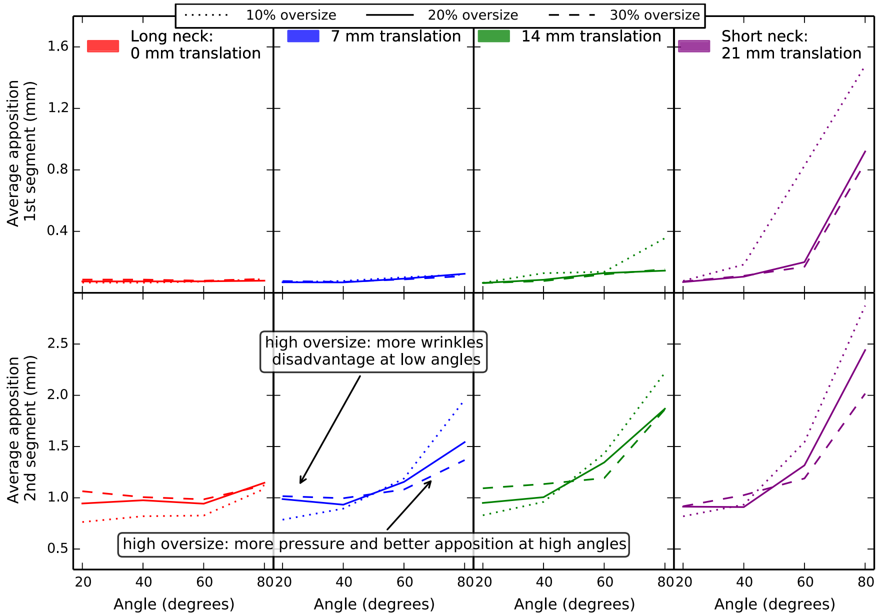

FIGURE 4.4: The distance to vessel wall, split for each segment (first segment: top, second segment: bottom). The x-axis shows the result for higher bending angles. Each column and color shows the result for a different straight neck length. Dotted, full and dashed lines show the results for 10%, 20% and 30% oversize, respectively.

relatively straight segments, while oversize assists apposition in curved regions.

Force asymmetry

The asymmetry of contact force vectors is very evident from figure 4.5, with values up to 0.7. All three parameters play an important role in the asymmetry measure. The angle of the geometry and the location of the stiff stent segments will increase the resemblance to the aforementioned three point bend test. The lower radial force associated with a lower oversize causes the index to rise, as the index is normalized to the total force.

Sealing path

The resulting costs of the path find algorithm can be seen in figure 4.5. All three independent variables influence the cost of finding a circumferential sealing path. For all angled cases (40°and more), the path found is located at the proximal side of the covered stent, as the device loses contact with the outer vessel wall curvature. See figure 4.3.b for an example of this detachment with the outer curvature and 4.3.c for the lack of contact force in that region.

4.3.2 α angle

When investigating the α angle between suprarenal and infrarenal aorta, different trends are observed. The first stent segment now shows the higher apposition values at a high curvature, as this segments now lies in the curved area (figure 4.6). The average distance to the vessel wall of the second segment to the wall increases less with angle, and improves with an increase in translation, as the stent ring lies again in a straight vessel segment.

The area reduction increases dramatically for an 80°angle. For this angle, a kink occurs between the two lasercut stents (see figure 4.7). The graft connection between these two lasercut stents is shorter, and behaves more stiff than the connection between the second stent segment and the following wire stent. With a radially confined stent (higher oversize), the graft is more wrinkled and allows somewhat more movement of the stent struts.

The asymmetery index scores relatively high. The 20°angle, 10% oversize case looks like an outlier (figure 4.8). A closer analysis showed that the value obtained from the algorithm was correct, and the result of the modest angle being sufficient to cause the pivoting effect, while the radial force for the low oversized proximal stent segment is very low. The high value is entirely due to the first stent segment having a value

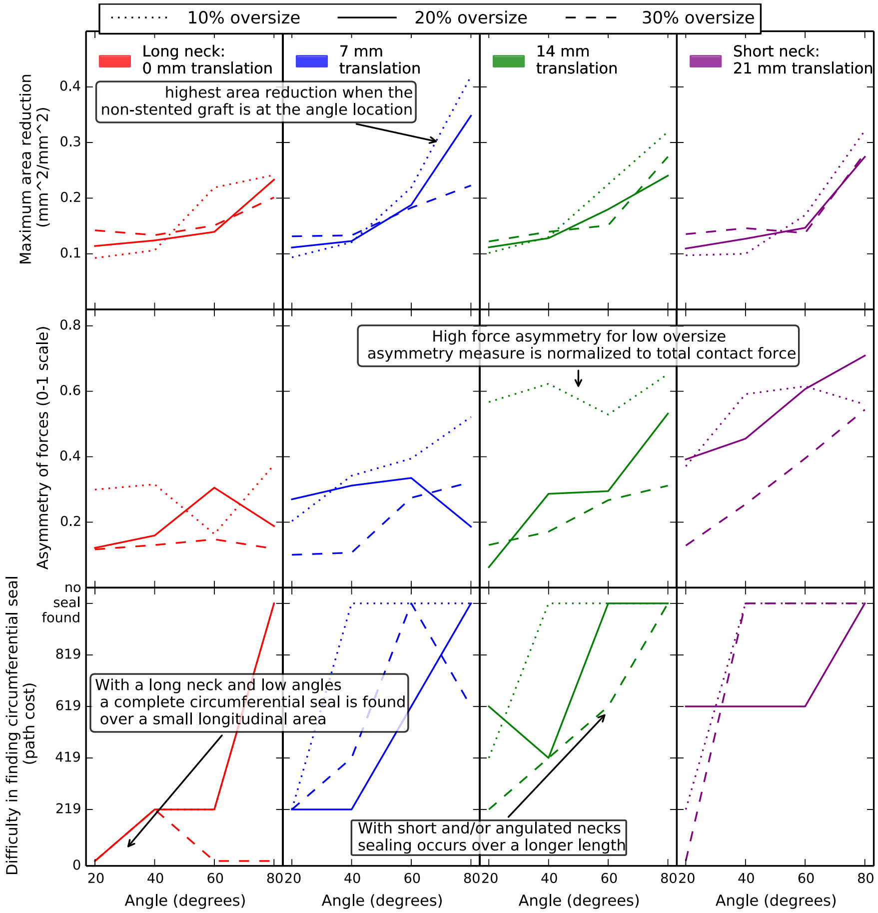

highest area reduction when the non-stented graft is at the angle location

High force asymmetry for low oversize asymmetry measure is normalized to total contact force

With a long neck and low angles a complete circumferential seal is found over a small longitudinal area

With short and/or angulated necks sealing occurs over a longer length

Figure 4.5: Top: the maximum area reduction of the flow lumen. Middle: asymmetry of contact forces. Bottom: difficulty (path cost) of finding a circumferential sealing. The x–axis shows the result for higher bending angles. Each column and color shows the result for a different straight neck length. Dotted, full and dashed lines show the results for 10%, 20% and 30% oversize, respectively.

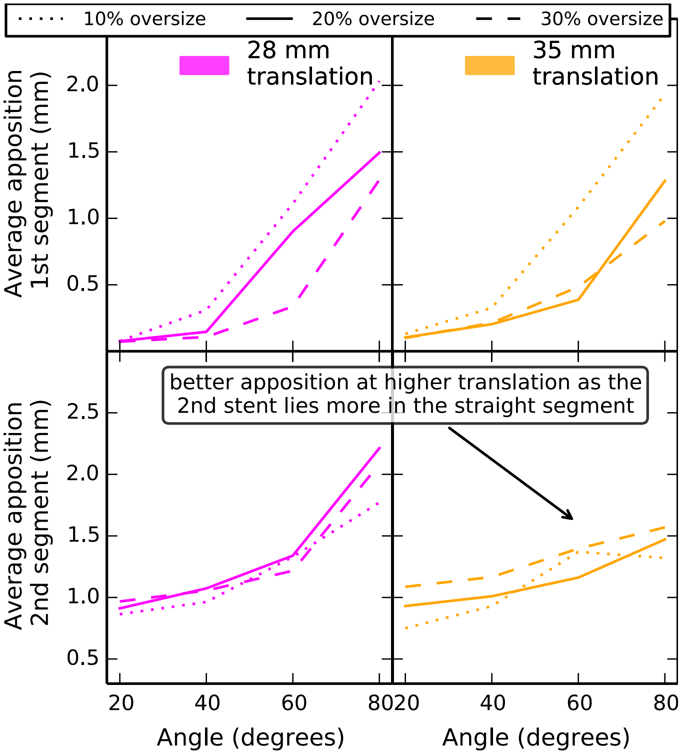

Figure 4.6: The distance to vessel wall, split for each segment (first segment: top, second segment: bottom). The x–axis shows the result for higher bending angles. Each column and color shows the result for a different straight neck length. Dotted, full and dashed lines show the results for 10%, 20% and 30% oversize, respectively.

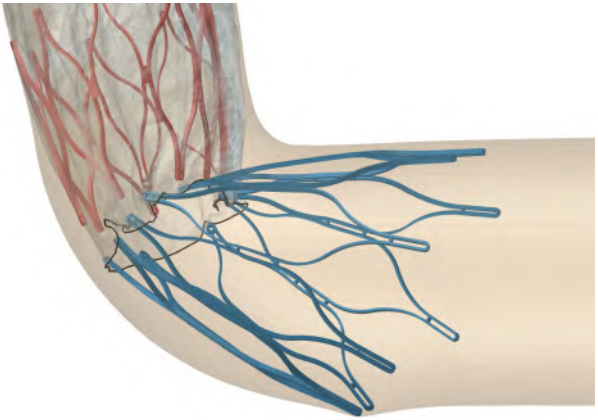

Figure 4.7: A finite element rendering of a deployed configuration of the device for the case of an oversize of 20%, angulation of 80.0°and translation of 35 mm (simulating a β angle). The device position is unstable, with a kink between the first and second stent segment, reducing the entry area of the graft (black outline).

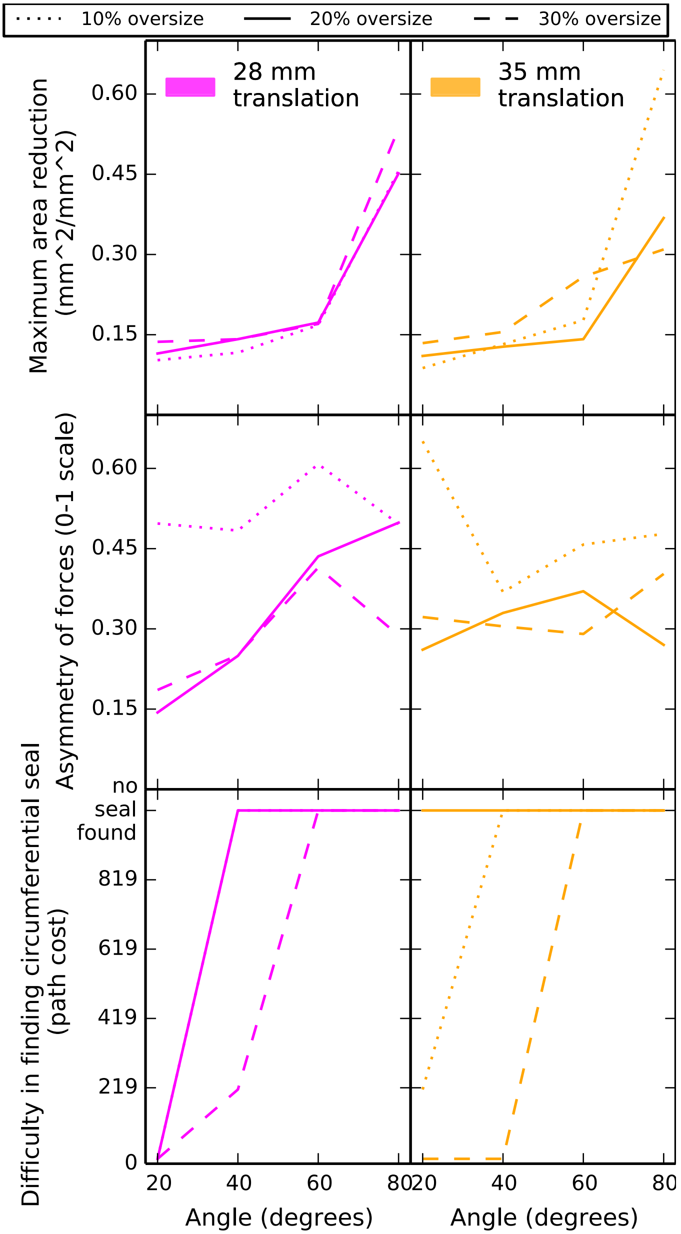

FIGURE 4.8: Top: the maximum area reduction of the flow lumen. Middle: asymmetry of contact forces. Bottom: difficulty (path cost) of finding a circumferential sealing. The x-axis shows the result for higher bending angles. Each column and color shows the result for a different straight neck length. Dotted, full and dashed lines show the results for 10%, 20% and 30% oversize respectively.

close to 1. Also in general this is the case, with the first stent causing a high asymmetry which is reduced by the second stent, which is now in a straight part of the vessel.

The pathfind algorithm does not find a circumferential seal in most cases. The reason is poor contact of the covered stent with the outer curvature, and for high bending angles, the kinking effect causing an ovalisation of the device.

4.3.3 Qualitative observation: stent strut grouping

During processing of the results, a relevant qualitative observation was made. With increasing bending angles, there is stent strut grouping at the outer curvature. This can be seen in figure 4.9. The effect is greater for higher oversize and a top stent closer to the curve.

4.3.4 Effect of a stiffer proximal neck

When the geometry is stiffer, the wall deforms less to the device. Because of this, the deformation metrics (apposition and area reduction) are worse in this stiffer neck (figure 4.10). As the wall is stiffer, the vessel diameter increases less under the stent's radial forces, which effectively causes a larger oversize when considering the deformed vessel diameter. The associated higher forces compensate adverse effects of the stiffer wall, and the force related metrics (force asymmetry and circumferential seal) do not consistently score better or worse.

4.4 DISCUSSION

In the present work, a finite element representation of the Zenith LP stent graft is virtually deployed in idealized geometries. The device has mechanical properties calibrated to experimental tests on a device sample [129]. The effect of varying geometry is investigated in a $3 \cdot 4 \cdot 6$ full factorial parametric analysis. Vessel angle and diameter are varied to reflect observed ranges of anatomical angles, and clinically used oversize percentages. A translation parameter changes the distance to the bend. This is related (but not equivalent to) changing the proximal landing zone length. A conceptual equivalence is an aneurysm with a lumen shaped as our geometry, i.e. an aneurysm filled with thrombus, leaving a cylindrical, angled lumen. The idealized vessel and used material properties mimick the silicone mock vessels used in preclinical investigations.

The 4 calculated parameters (distance to vessel wall, area reduction, force asymmetry and the costs of finding a sealing path) have been chosen to reflect possible adverse effects during or after surgery. Severe stent malapposition could cause wires, catheters and other endovascular

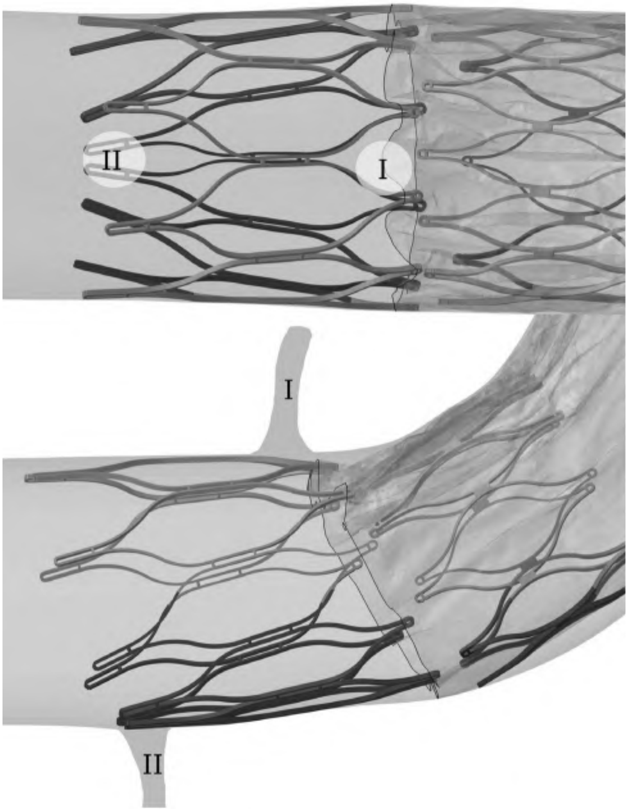

FIGURE 4.9: A finite element rendering of a deployed configuration of the device for the case of an oversize of 20%, angulation of 60°and translation of 21 mm. I and II indicate possible locations of the renal artery origins that could result in multiple struts covering the orifice of the most proximal renal artery (II)

devices to get stuck at the stent edge or move the deployed device. If not ballooned after deployment, poor apposition of the uncovered stent would mean inadequate anchoring of the hooks. Our data shows that severe malapposition is expected for a combination of large angles, low oversize and a short straight landing zone.

A reduction in lumen area will alter the flow conditions, and will induce both a downward and lateral force component. While ballooning after deployment can solve the problem, during the endovascular procedure this force component can move the device away from its intended location. The bending angle is the major influence for area reduction. From our analysis, a high α bending angle has more adverse influence than a high β angle, mainly because of the unstable kinking of the device for angles above 60°. For a β angle between infrarenal neck and aneurysm

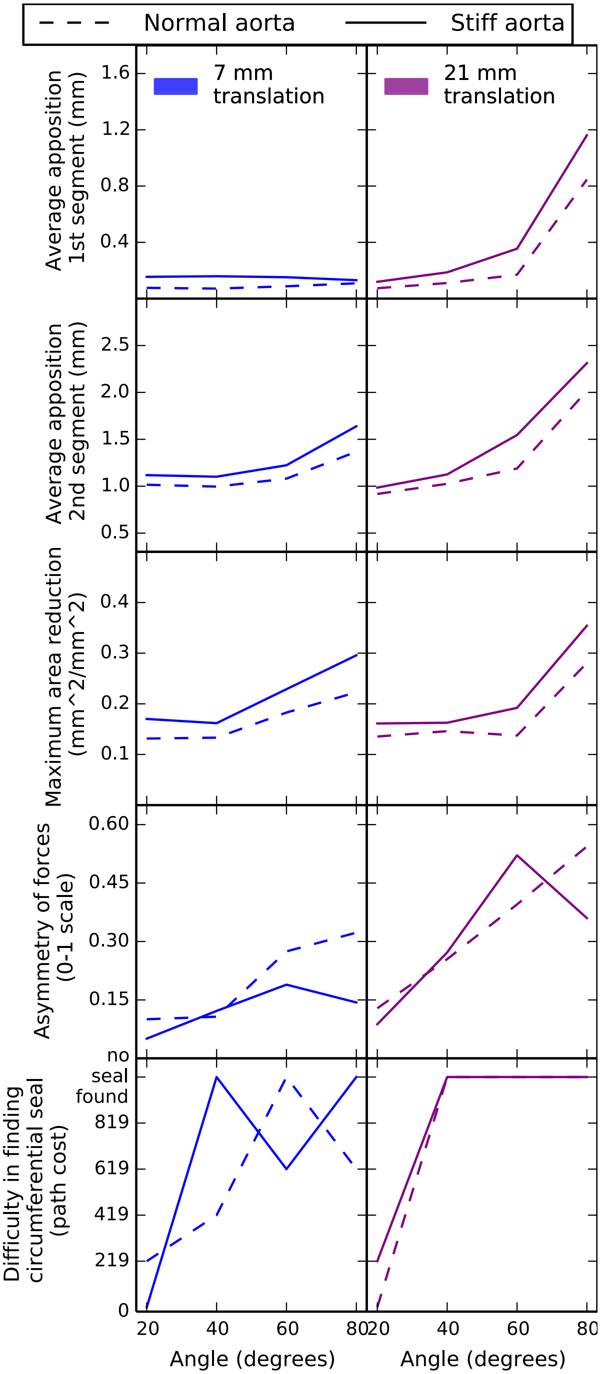

Figure 4.10: Comparison of the output parameters when increasing the stiffness of the aorta. The x-axis shows the result for higher bending angles. Each column and color shows the result for a different straight neck length. Oversize was 30% in all cases

we show that a graft segment not supported by stents at the location of this curve will have the highest reduction in lumen flow area.

Force asymmetry is a relative measure of how forces act to straighten the proximal neck. Neck straightening is often observed [147, 148]. A recent study showed that straightening can be device specific [149]. A high asymmetry index also suggest suboptimal anchoring of the uncovered stent, and a lack of stent to wall contact and sealing at one of the sides of the covered segment.

The last parameter is the cost associated with finding a path over the circumference with the stent pressing onto the vessel. This parameter is the most artificial, in the way that the values are very dependent on the discretization and averaging of the vessel force values. As a relative measure, the parameter does show a distinct trend, showing the risks associated with angulated necks and short straight landing lengths.

For all investigated parameters, a higher stent graft oversize has beneficiary effects in angulated necks, yet not enough to alleviate the risks associated with short and/or angulated necks. This is in accordance with recommendations by some authors to oversize more than 20% in angulated necks [150]. A review on the benefits and risks of oversizing showed that an oversize of 25% could decrease the risk of endoleak, without differentiating between straight and angulated necks [53]. Similar to what we see in our simulations (see figure 4.9), Van Prehn et al.[53] stated that endografts do not land perfectly in line with the aortic neck, but rather angulated. This decreases the *effective* oversize in angulated deployments.

Some risks are still involved with oversizing devices. Higher radial force associated with oversizing could lead to dilatation of the proximal neck region. Higher oversized devices cause more wrinkling of the graft, as evident from the area reduction results presented. Infolding of the stent graft has been reported in literature, however, data on the risk of graft infolding and adverse effects of oversizing more than 30% were inconclusive [53]. In our simulations, infolding of the stent struts in the radial direction does not occur for this device up to 30% oversize.

Besides the risk of treating patients outside IFU and the adverse effects and benefits of oversizing, a third controversial topic with often inconclusive data, is the effect of suprarenal fixation on renal function [54]. CFD calculations and experimental work [151, 152] evaluated the flow reduction caused by stent wires crossing the renal artery ostium. As a qualitative observation, we noted that stent struts can group at the opposite site of a curved neck. Renal arteries are often asymmetrically located. If the aneurysm has a lateral angle, the grouped uncovered stent struts could indeed cover the most proximal renal artery, as graphically shown in figure 4.9. The design of the Zenith LP, with sigmoid struts forming closed cells, is already a marked improvement from the earlier Zenith Flex device. The cell shapes remain open, while only the most proximal parts group together. The adverse situation described above is thus limited to high angled and highly asymmetric renal artery location. The Zenith Flex V-shaped stent struts have little resistance to this circumferential, asymmetric compression and group over a longer length.

Clinical outcome studies differentiating hostile and favorable necks are often difficult to compare or group. Different endograft devices are used in widely differing anatomies. Furthermore, outside or inside IFU is often based on the proximal neck being either too short, too angulated or having a too large diameter. As stated in a meta-analysis [47], “the authors used specific criteria for “hostile neck“ but did not state how many of the patients had two or more of these qualities”. Our analysis for a single device in various adverse geometrical situations shows that for most adverse parameters calculated, the combination of a short straight neck and a high angle causes the highest values.

A more frequent use of a consistent classification system [153, 154] and a standardized method to measure aortic angulation [155] would clearly be beneficial, not only when comparing clinical studies, but also when relating mechanical parameters, such as the ones calculated here, with both short and long term clinical outcomes.

4.4.1 Limitations

The presented study uses the finite element method to calculate the mechanical behavior of a deployed stent graft. This method offers advantages over in vitro setups in associated costs, time and the ability to extract additional information on component deformations and forces. Computational research also presents some limitations.

While the stent graft geometry and mechanical properties are obtained from experiments on a sample, it remains a mathematical representation of reality. Modeling the proximal neck as a curved, cylindrical tube with a single and isotropic compliance is, compared with the in vivo wall properties, a simplified situation. While in this work the focus was on the stent mechanics, a more detailed representation of aortic wall geometry and anisotropic [73] and heterogeneous material properties [156] could add more info to the debate. Furthermore, aortic displacements could be limited by the mechanical support of adjacent tissue, most notably the spine and vena cava.

Similarly, while we calculate the mechanical behavior after deployment, it is known that the proximal neck region remodels over time [157], and can increase in diameter, caused by the radial force of the stent or continuation of the aneurysmal disease [52]. Including this remodeling process and a time dimension in computational research is a valuable yet highly challenging extension to this work.

The used method calculates a mechanical equilibrium between a device with stiff and flexible segments (metallic stents and fabric graft) and the aortic wall. This is just one of the many possible deployed configurations that could occur *in vivo*, where many confounding factors play a role: (stiff) guidewire insertion, deployment speed, forces and movement exerted by the operator on the deployment system, pre or post-procedural ballooning, use of extender cuffs, etc.

This equilibrium is calculated in the absence of external forces. Including pulsatile blood pressure and inertial forces would be an extremely challenging task. The lack of a perfect seal condition can cause both inner and outer surface of the graft to be pressurized. Simulating (pulsatile) pressure gradients and inertial forces is an interesting but challenging coupled fluid structure interactions problem which, if solved, would have very long run times with currently available technological means.

Clinical data on the outcome of hostile versus favorable neck anatomy is often inconclusive and not grouped according to device used or proximal neck morphology. The output parameters calculated in this study can not directly be related to the outcome after EVAR, and the use is limited to comparative analyses which are qualitatively related to possible adverse events. A future, ambitious, objective could be to retrospectively analyze device related failure or reintervention cases with the method used here, with a complication free control group. The idealized geometries used in this study could be supplemented with patient specific simulations and experiments. Finally, more data by stent graft manufacturers on the factors that led to the IFU and the amount of conservatism build in could assist in the debate.

Three

Virtual EVAR: simulating the deployment of a stent graft

CHAPTER 5

In vitro validation of the virtual deployment of a stent graft device

In the previous section, material and geometrical properties were obtained for 4 commercial devices. The constructed models can be used to virtually simulate EVAR. In this chapter, a FE approach is developed and validated *in vitro*. A silicone mock aneurysm model is used to represent a patient's AAA anatomy.

This chapter is based on: "Virtual evaluation of stent graft deployment: a validated modeling and simulation study" as published in the Journal of the Mechanical Behavior of Biomedical Materials [140].

5.1 INTRODUCTION

An Abdominal Aortic Aneurysm (AAA) is a local dilatation of the aorta, commonly involving the region between the renal arteries and the aortic bifurcation. A tear in this weakened aortic tissue would result in life threatening internal bleeding, with a very high mortality rate [158]. Conventional treatment is open surgical repair (OSR) by abdominal incision and clamping of the aorta, a very invasive and high-risk procedure. An alternative to OSR is endovascular aneurysm repair (EVAR) with stent graft implantation. This procedure has proven to be a valid alternative with clear benefits in terms of length of hospital stay, reduced operational mortality and less trauma [35]. In the long term however, the outcome does not differ significantly [159]. One reason for this are stent graft related complications, including graft migration, endoleakage and fatigue failings [20–23, 160].

Numerical modeling of stent grafts and aneurysms can be used to assess the strains, stresses and forces occurring in vivo and can play an important role in research on stent and vessel mechanics [161]. Numerical studies on AAA focused on assessing the rupture risk and location, using Finite Element Analysis (FEA) [70, 73, 162], and Fluid Structure Interaction (FSI) [82, 83]. The interaction of endografts with the intraluminal blood has been investigated using Computational Fluid Dynamics (CFD) and FSI modeling. Using these numerical techniques, the displacement forces on the device and stress reduction on the aneurysm wall by stent graft placement were assessed. Using idealised stent graft models, satisfying results for these objectives were obtained [114, 116, 124, 144, 163]. De Martino et al. (2004) [104] and Moloney et al. (2009) [122], amongst others, have studied the stresses on the aneurysm sac before and after EVAR as well as the stresses placed on the stent graft and its attachment system. Both investigations reported that the majority of stress is absorbed by the stent graft, reducing AAA wall stresses after repair by more than 90% of the values before stent placement. Idealised, uniform stent graft models do not take into account the mechanics of the stent graft during deployment, stresses in the material and radial forces exerted by the device. Comparing these mechanical parameters for different devices is also no option with uniform models.

A large step forward in stent graft device modeling was made in a study by Kleinstreuer et al. (2008) [105] investigating a tubular, diamond-shaped stent graft under cyclic loading and its deployment in a circular AAA neck. However, most endografts used in clinical practice are bifurcated, modular systems, which are only approximately cylindrical. Moreover, the deployment sites are seldom circular, nor straight and can extend (for the majority of recent commercial devices) to the suprarenal region of the aorta, raising the need to model the renal arteries. Consequently, in order to investigate localized damage and failure and the potential suboptimal deployment of the device, or realistic deformations of the artery, a generalized (cylindrical) geometry may not suffice. To the best of our knowledge, no prior research has been published on virtual deployment of a complete, bifurcated stent graft in a realistic AAA model.

In this study, the deployment of a commercial stent design (Talent, Medtronic, Minneapolis, Minnesota) in an aneurysm geometry is performed, and validated in vitro using a silicone mock aneurysm.

5.2 MATERIAL AND METHODS

5.2.1 Stent graft geometry and material properties

Stent geometry and dimensions were reconstructed from high resolution μCT scans of a Talent stent graft. A surface reconstruction of the stent's nitinol rings was performed using *Mimics* software (Materialise, Leuven, Belgium).

The centerlines of the nitinol springs were extracted using a self developed algorithm within the open-source pyFormex framework. Using geometrical operations, the stent surface model was unrolled and clipped into small wire parts. The centerpoints of all wire parts were fitted by splines to form the wire centerlines. Splines are approximated by polylines of non-uniform length according to local curvature. The wires were modelled using Timoshenko beam elements, which are reported to yield accurate results in stent modeling [133]. In the Talent stent graft, wire segments are bent ten times and clamped at the ends to create the M shaped stent rings. The wires added for columnar support are attached in a similar way. In the model, the rings were created from one continuous wire, while the connection between rings and columnar wires was modeled using a 'no slip' connection at the neighbouring nodes. The μCT surface reconstruction and FEA model of the stent wires are shown in Figure 5.1. The deployed device has a diameter of 28 mm (proximal main body), a graft covered length of 170 mm and a total length of 185 mm, the three rings in the main body have a length of approximately 16 mm. The inner diameter of the most distal iliac ring is 14 mm, with a ring length of 14 mm. The more proximal iliac rings are gradually larger, up to 14.8 mm diameter. The device was shrunk to a minimal diameter of 22 Fr. (7.33 mm), equal to the delivery system's diameter. The wire diameter measures 0.5 mm.

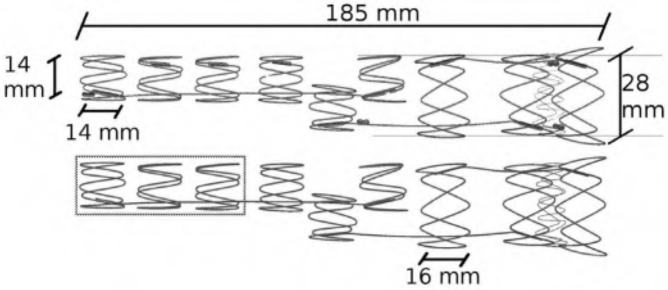

FIGURE 5.1: μCT surface reconstruction (top) and FEA model (botom) of the nitinol stent graft wires.

The super elastic behavior of the nitinol material is modeled using a user-defined material subroutine, based on the model described by Auricchio and Taylor (1997) [134]. Uniaxial tensile testing on wire samples, obtained from a sacrificed sample of the stent, were carried out to determine the material properties of the nickel titanium alloy. Because of the limited dimensions of the stent sample, the wire used for testing was 50 mm, resulting in a grip to grip distance of 24.1 mm. These tests were performed at room temperature using an Instrom 5942 electromechanical tensile test system (Instron, Norwood, MA, USA). Following the ASTM F2516-07e2 standard, the material is pulled to 6% strain, unloaded to less than 7 MPa, and eventually pulled to failure. The system was configured with a 500 N load cell and wedge-style grips. As per ASTM standard, the crosshead speed was selected to be 0.02 * Sample Length. A Differential Scanning Calorimetry (DSC) test was performed to assess the transformation temperature. For the tested sample, the austenite and martensite finish temperatures (A_f and M_f resp.) were determined.

The material properties were validated by performing a radial compression test on three of the stent rings. For this, a radial crimping head (MPT Europe, Leek, The Netherlands) was mounted on the electromechanical test system. The experimental crimping force was compared with a finite element result, mimicking the procedure, and using the uniaxial tensile test material parameters as input. This test was non-destructive and was repeated 5 times to account for any difference in initial sample position. The rings on which the test was performed are indicated in Figure 5.1. The inner diameter of the smallest, most distal ring ring is 14 mm, and the outer diemater measures 15 mm. The two proximal rings are slightly larger (approximately 15.6 mm outer diameter). The crimping was simulated using Abaqus/Explicit in a quasi-static analysis. Frictionless penalty contact was used. One point of each ring was constrained in Z and Theta direction to avoid rigid body movements. A mesh sensitivity analysis was performed on the most distal stent ring to choose proper beam element dimensions. Element size was decreased until the radial outward force during crimping was stable for halving the mesh size. Going from 200 beam elements (size 0.74 mm) to 400 (size 0.37 mm) decreased the radial force after crimping 8 mm by 0.8%. In general, the beam elements show stable results, even for coarser meshes. Although, from this analysis, larger element sizes would be well possible, we opted for a non-uniform mesh with relatively small element sizes to allow for smoother contact, better connection with the covering membrane, and a better visualization. After a mesh sensitivity analysis, the complete stent model consisted of 3046 beam elements of non-uniform length. In curved areas, beam element sizes were smaller. The beam elements had an average length of 0.57 mm, with minimum and maximum lengths of 0.10 and 1.23 mm.

The dacron membrane covering the stent does not show up on the μCT scans of the Talent stent graft and was added to the FEM model by spline fitting the circumference of the subsequent stent rings. The fabric was discretized with 64812 quadrilateral membrane elements. As in reality, the membrane was 'stitched' to the nitinol rings using the 'no slip' connection. The small element size for the membrane elements was necessary from a computational point of view. The elements (that have no resistance to bending) have to be small enough to fold during crimping, without excessive deformations. Deformation behavior of the stent did not change with decreasing membrane element size. The fabric material properties were obtained from literature [105].

5.2.2 AAA geometry and material properties

The aneurysm geometry considered is a physical, realistic silicone model (Elastrat, Geneva, Switzerland). It includes a 4.5 cm diameter fusiform abdominal aortic aneurysm, renal arteries and the common, internal and external iliac arteries. A CT study was performed on a Siemens Somatom Definition FLASH (Erlangen) (128·0.6 mm detector arrays). Signal to noise ratio was optimized with a spiral pitch factor of 0.85 and a slow rotation of 0.33 msec/rotation. Reconstruction parameters were a 'B70 very sharp' reconstruction kernel, a FOV of only 14x14 cm, slice thickness was 0.6 mm, and in plane pixel spacing was 0.27 mm. With this high resolution scan and image reconstruction, and excellent contrast between silicone wall and surrounding air, it was possible to extract the silicone model's wall (inner and outer border). Similar to the μCT data processing pipeline, *Mimics* was used to extract the wall surfaces. Using an in house developed meshing tool [164] we connected and discretized the surfaces, resulting in an accurate digital version of the silicone vessel geometry.

The model was discretized using 34270 linear hexahedrons in a multiblock structural and conformal grid. Aneurysm mesh sensitivity was performed ensuring insensitivity of mesh size on displacements while inflating the aneurysm by an internal pressure. Halving the element size (77334 elements) changed the maximum displacement by 1.73%, further increasing the number of elements (115668 elements) only changed the maximum displacement by 1.95% compared with the chosen mesh size, confirming convergence. Silicone model and finite element model can be seen in Figure 5.2.

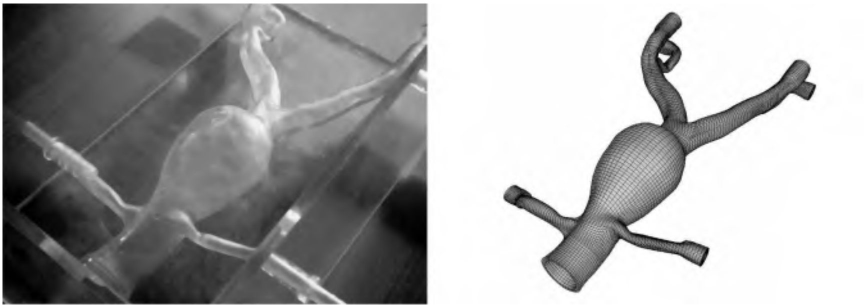

FIGURE 5.2: Silicone model (l.) and discretized FEA model (r.).

$$W(\lambda_1, \lambda_2, \lambda_3) = \sum_{i=1}^{N} \frac{\mu_i}{\alpha_i}(\lambda_1^{\alpha_i} + \lambda_2^{\alpha_i} + \lambda_3^{\alpha_i} - 3) \tag{5.1}$$

The silicone is modeled using the hyperelastic first order Ogden strain energy function (5.1). It has been shown that this material model accurately describes the behavior of silicone rubbers [165]. Furthermore, this strain energy function has the added advantage that the material remains stable at all stresses and strains. Material parameters μ and α were fitted to experimental inflation data. The silicone model was pressurized by increasing water pressure. Simultaneous diameter measurements were performed by ultrasound using a GE Vingmed Vivid 7 ultrasound machine with a 12L Linear Array vascular probe. The finite element model of the silicone mock aneurysm was subjected to an internal pressure, mimicking the experimental inflation. The fitting was performed by minimizing an objective function defined as the sum of the squares of the difference in displacement between this finite element solution and the experimental measurements on the silicone model. Both with ultrasound and in the finite element model, the diameter was measured at the same two discrete measuring points; the location of maximum diameter (aneurysm sac) and the aneurysm neck. The function was minimized using the Constrained Optimization BY Linear Approximation (COBYLA) method, a modified version of Powells method [166]. COBYLA is a derivative-free optimization algorithm adapted to problems with low number of variables (only 2 in this case, order N = 1).

5.2.3 Simulation strategy and post processing

The stent graft and aneurysm finite element models were combined and assigned the material properties obtained from the nitinol uniaxial test and the silicone fitting procedure. A deformable sheet acting as the stent's delivery system was used to perform the crimping and bending of the stent graft, mimicking crimping and stent insertion. Deformations of the stent graft occur through displacement driven contact with this sheet. The virtual displacement of the sheet was imposed using a user subroutine (VDISP) to analytically define nodal displacements [167]. In the first two steps, the sheet (and stent graft) is first crimped to 22 Fr., and subsequently moved into the vessel geometry. During the deployment step, the radius of the guiding sheet is gradually increased, starting at the proximal neck, to the most distal iliac location, mimicking the in-vivo occurring deployment of the device by retracting the delivery system.

The FEA calculations were performed using Abaqus/Explicit 6.10 (SIMULIA, Dassault Systèmes), in a quasi-static analysis with negligible kinetic energy. Endpoints of the aneurysm model (i.e. attached to the acrylic glass case in the physical model) were fixed in place during the entire simulation. Penalty contact was used. During crimping and bending, frictionless contact between stent graft and the crimping sheet was assumed. During deployment, friction between stent graft and sheet was increased to 0.2 to avoid slipping of the distal rings while the proximal part of the device is already released. Friction between stent graft and silicone aneurysm was put at 0.2, as silicone is known to have a high static friction. The finite element method enabled the visualization of the mechanical deformations of the stent and the silicone aneurysm. We investigated both global resulting geometry and artery cross-sections, and assessed radial forces exerted by the stent graft onto the aneurysm neck, and iliac artery. An additional mesh sensitivity analysis for the global model was performed by halving all element sizes, establishing the stability and convergence of the FEM results.

5.2.4 Experimental validation

Experimental validation was performed by inserting the stent graft into the silicone model, using a 22 Fr. introducer sheet with the tip cut off. A CT-scan after stent deployment was performed, to compare the stented configuration with the baseline geometry. The CT imaging was performed with the same scan and reconstruction parameters as the baseline scan. Baseline and stented aneurysm volumes were co-registered by overlapping the fixed endpoints. From the registered image, both external silicone vessel wall and the stent struts were extracted.

As a qualitative validation method, we compared the deformed configuration (with deployed stent) to the finite element results. The lumen increase of the silicone vessel was used as a quantitative comparison method. All calculations were performed on outer border surfaces of the aneurysm model. Triangulated surface models were extracted from the CT data for the silicone model before and after deployment. The outer border of the FE model was made triangular by dividing each quadrilateral face. The STL surfaces were imported into pyFormex, and cross-sectional areas were calculated after cutting the 3D models with 455 axial slices at 0.4 mm intervals. Only the ipsilateral iliac artery lumen was taken into account. The renal arteries were cut off close to the aorta, to avoid an influence on the calculated area and discontinuities in the curve. In line with in vivo investigations described in literature, we performed additional simple diameter measurements on a) the CT image of the silicone mock aneurysm before and b) after stent deployment and c) the simulation result after deployment. Following Sampaio et al. (2006) [52] we measured the diameter increase of the minor axis of the cross-sectional ellipse, midneck. Due to the limited aneurysm neck length, this location is just below the lowest renal artery.

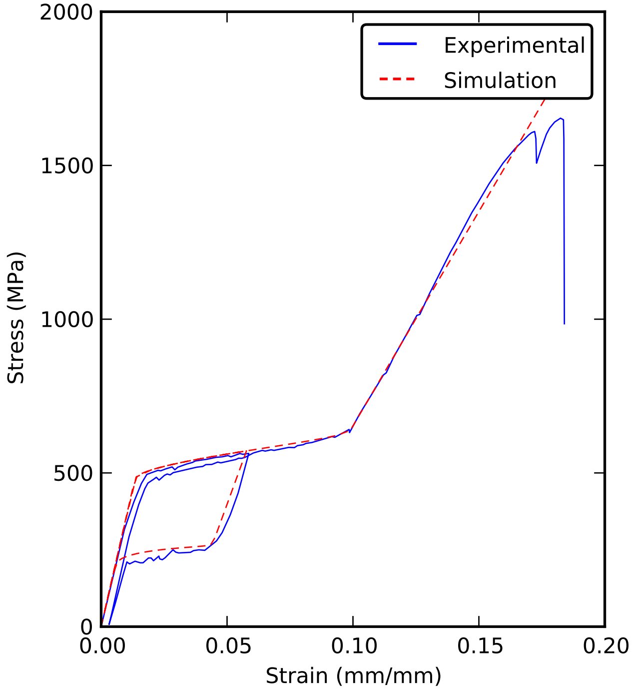

Figure 5.3: Nitinol stress strain curve from the uniaxial tensile test on a wire, and the corresponding finite element material model.

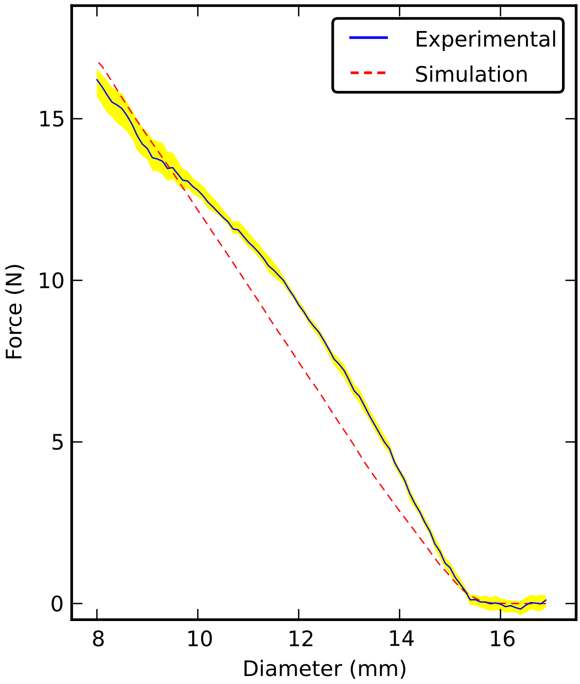

FIGURE 5.4: Simulated and averaged experimental radial loading curves for a Talent stent graft nitinol segment. The yellow surface indicates the maximum spread of the (unfiltered) experimental results

5.3 RESULTS

5.3.1 Material testing

Results of the uniaxial tensile test on the wire sample are plotted in Figure 5.3. The radial crimping results, both experimental and FE results, are depicted in Figure 5.4. The finite element model underestimates radial force by, on average, 0.65 N. The largest difference in result is 1.8 N, or 24.3% less. The calorimetric test yielded transformation temperatures A_f and M_f equal to 283.15 and 257.35 K. Because all tests were performed at room temperature, all wires were in austenitic phase before straining.

The vascular geometry was observed to have a largely varying wall thickness. Minimum wall thickness was 0.39 mm, maximum 4.42 mm and average wall thickness 1.58 mm. For the aneurysm material characterization, the silicone strain energy function parameters returned from the optimization procedure are $\mu = 0.538$ and $\alpha = 2.95$. The resulting

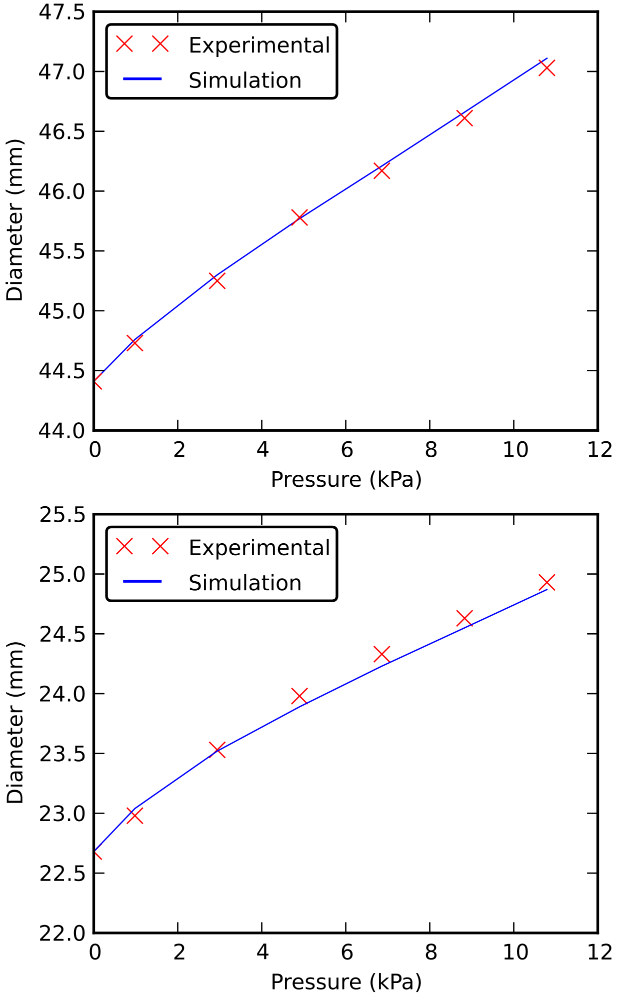

FIGURE 5.5: Measured diameters while inflating, and final finite element resulting diameters after parameter optimization for the aneurysm sac (top) and neck (bottom).

parameters fit the measured inflation data, as can be seen from Figure 5.5. The root-mean-square deviation for the 14 data points is 0.057 mm. The average elastic modulus E_p is 10.9 N/cm^2 for the aneurysm neck and and 18.3 N/cm^2 for aneurysm sac. The elastic modulus of the vessel can be calculated from the measured diameters at systolic and diastolic pressures using equation 5.2. Material properties are summarized in table 5.1, 5.2 and 5.3.

$$E_p(N/m^2) = K\frac{P_{sys} - P_{dias}}{(D_{sys} - D_{dias})/D_{dias}}, where \tag{5.2}$$

$K = 133.3$, a constant to convert E_p from mmHg to N/m^2. $P =$ arterial blood pressure. $D =$ aortic diameter [168]. For the in vitro case, 'systolic' and 'diastolic' are the pressures and diameters at 10.79 kPa (sys) and 0 kPa (dias).

TABLE 5.1: Silicone material properties, a Poisson ratio equal to the Abaqus default for (near) incompressible materials was assumed.

Variable	**Value**
μ	0.538
α	2.95
Poisson ratio ν	0.475

TABLE 5.2: Fabric (PET) material properties.[105]

Variable	**Value**
Young's modulus	1.84 GPa
Poisson ratio ν	0.35

5.3.2 In vitro validation of FEA results

The resulting deformed geometry of stent graft and silicone artery is shown in Figure 5.6. An animated visualization of the complete deployment of the device is available online[1]. The guiding "introducer" is not shown in the simulation to allow for a better view on the stent graft. The FE method makes it possible to extract the external forces and deformations from the model. For this stent graft - artery combination, the radial outward integrated force, which keeps the device in place, totals 4.2 N for the proximal rings, and 8.5 N for the distal, iliac leg. The radial forces are visualized in Figure 5.7. In Figure 5.7, beam elements are color coded according to the maximum principal strain, over all section integration points, at the cross-section location. The

---

[1] `http://dx.doi.org/10.1016/j.jmbbm.2012.04.021`

TABLE 5.3: Nitinol material properties. Symmetry in compression and a Poisson ratio of 0.3 was assumed.

Variable	**Value**
Austenite elasticity E_A(MPa)	35850
Austenite Poisson ratio ν_A	0.3
Martensite elasticity E_M (MPa)	13950
Martensite Poisson ratio ν_M	0.3
Transformation strain ϵ^L	0.0532
Start of transformation loading (MPa)	480
End of transformation loading (MPa)	640
Reference temperature $T_0(K)$	295.15
Start of transformation unloading (MPa)	270
End of transformation unloading (MPa)	200
Start of transformation stress in compression (MPa)	480
A_f temperature (K)	283.15
M_f temperature (K)	257.35

graph in Figure 5.7 shows the distribution of this maximum principal strains after compacting and after deployment. The radial forces and strain distribution during the deployment procedure are shown online in appendix D (animation)[1].

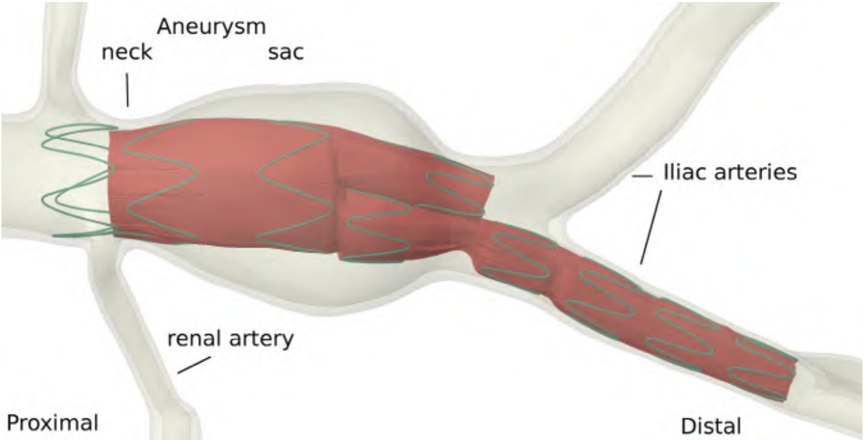

FIGURE 5.6: Rendering of the finite element result showing final deformed configuration of the stent in the semi-transparent silicone mock aneurysm.

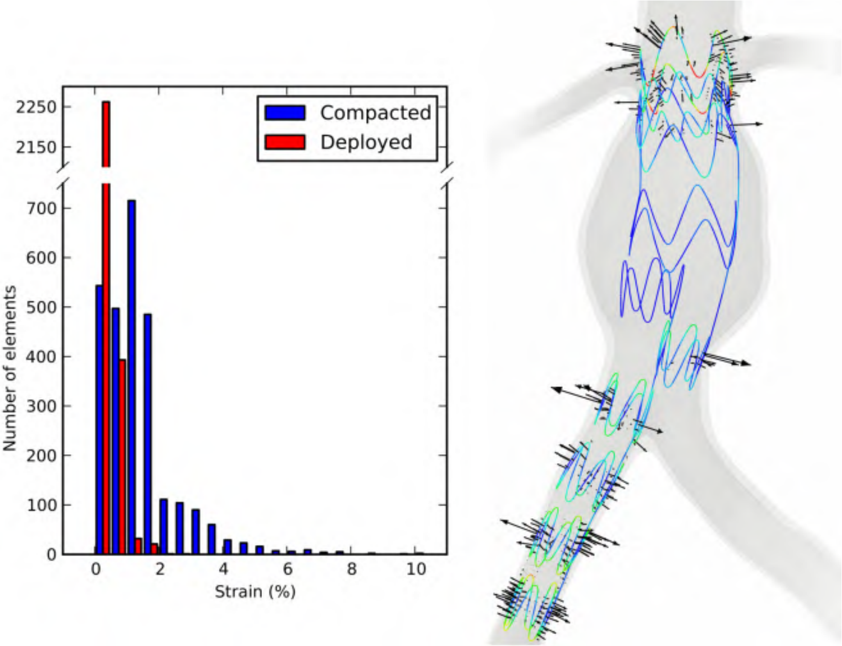

FIGURE 5.7: Contour plot of the maximum principal strain in the stent wires, in the final configuration, color scale from 0% (blue) to 1% (red). Superimposed are the contact force vectors, exerted by the stent graft onto the aneurysm. The graph shows the distribution of strain after compacting and after deployment, with a bin-width of 0.5%

Qualitative comparision

The qualitative comparison consists of assessing the agreement in the final shape of the metallic struts of the deformed stent. As can be seen in Figure 5.8, there is a good agreement in strut location in the proximal and distal regions of the stent. In the bifurcation region however, there is a difference between the two results. It is attributed to a small rotation of the ipsilateral (long) iliac limb in this region which is not present in the simulation result.

Quantitative comparision

To validate the stent graft deployment quantitatively, we compare the vessel lumen increase post stenting for the simulated and experimental situation. The resulting graph (Figure 5.9) confirms the qualitative visual findings. The measured and calculated areas post stenting are similar for the proximal and distal fixation sites. However, in the bifurcation region there is the highest difference, the experimental stent deployment

Figure 5.8: Qualitative visual comparison between 3D models of the experimental deployment (white) and the virtually deployed stent graft (red), with a coronal CT-slice background as a plane in space, obscuring the lower half of the stents.

causing an area increase of 10 mm^2 (or 2.25%) while after the simulated deployment, the area at the bifurcation region does not increase. Also just below the renal arteries, the simulation underestimates the area increase.

The single midneck diameter measurements are 26.6 mm (pre), 27.5 mm (experimental) and 27.3 mm (simulation), resulting in a diameter increase of 0.9 and 0.7 mm respectively. Note that at this slice, the major axis of the cross-sectional ellipse did not increase with stenting.

5.4 Discussion

The work presented investigates the mechanics of endovascular aneurysm treatment, and validates the finite element modelling in vitro. Although the rate of success for endovascular aneurysm treatment is very high with the latest devices, complications and late failure still occur. We developed technology to evaluate the mechanical impact of aneurysm stenting with an endograft, hoping to, in future work, be able to give mechanical insight into better device selection and sizing for high risk patients.

Specific care has been given to the construction of accurate geometrical models and material formulations. Reverse engineering of the stent graft geometry from μCT images has been performed previously [128]. The endograft reconstruction is different by the nature of the geometry (wires vs. lasercut stent) and the need for adding the covering membrane. While nitinol material properties used for endograft devices have been previously reported [105], to the authors knowledge this is the first time that the material properties are derived from mechanical tests on actual

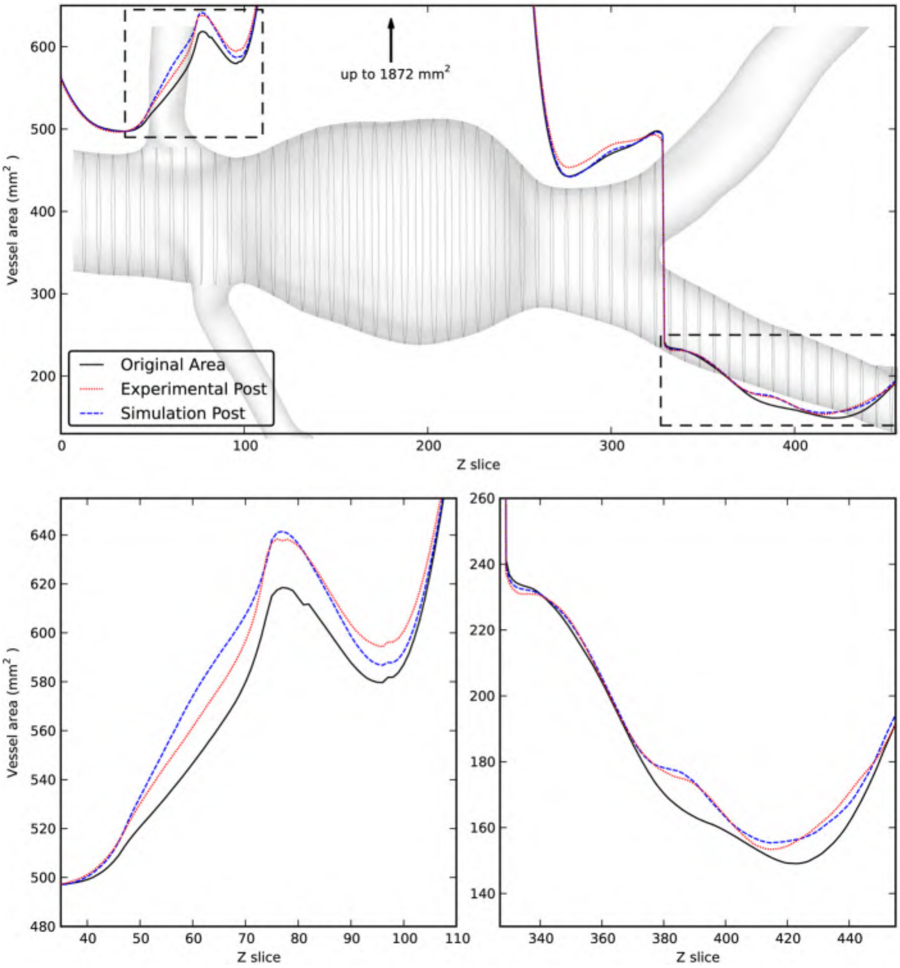

FIGURE 5.9: Lumen area for the baseline situation and the experimental and virtual stented aneurysm. The semi-transparent overlay shows slices used for the area calculations.The dashed indicator rectangles show the location of the enlarged bottom graphs.

stent graft samples. Additionally, we confirmed the material input by comparing a simulated and experimental radial crimp test on a stent graft segment, showing good agreement, although slightly underestimating the response during crimping. Apart from uncertainties and noise on material characterization and geometry, we believe there are two major possible reasons for this behavior; 1) the difference in experimental loading at low strain (<1.4%) of the nitinol, with a declining elastic modulus, and the material model, in which E_a is considered constant, and 2) a possible non-constant frictional behavior during the experimental test. Comparing our results to the reported values by Kleinstreuer et al. (2008) [105] show that the material tested is slightly more flexible than the most flexible material reported (E_A, E_M of 35850, 13950 MPa vs 40000, 18554 MPa). A direct comparison between values is difficult because the size of the tested wire, surface finish, transformation temperatures and possible temperature treatments are all unknowns. The small sample length used in this study could have caused us to underestimate the elastic modulus of the material. Additionally, the testing temperature is different (room vs body temperature). Regardless, it is clear that the nitinol used in this stent has a low elastic modulus, considering the range possible for this alloy.

The work presented validates the FE model in a silicone model, approximating the in vivo situation. The average elastic modulus for the aneurysm neck and sac (10.9 and 18.3 N/cm^2) fall within the range previously reported for human aneurysmal aortas: 6.4-19.4 N/cm^2 for the neck and 5.5-94.6 N/cm^2 for the aneurysm sac (concatenated ranges from various studies [168]), indicating a realistic in vitro situation. The advantage of the in vitro approach is that a higher resolution CT scan could be performed on the inert model, getting an accurate aneurysm geometry, including the localized wall thickness. The silicone material characterization was resolved using an alternative method. Instead of performing mechanical tests on the silicone, the material parameters were obtained by solving the inverse problem of estimating material properties from model deformations. This technique, depending on aneurysm geometry and pressure-diameter data, can be transfered to a clinical situation. Using ultrasound measurements (IVUS or external) [169, 170] or dynamic CT [171] and MRI imaging [172], combined with blood pressure measurements, similar data can be obtained, as recently demonstrated by Tierney et al. (2012) [173] for ECG gated CT.

In validating stent graft deployment, we found that the finite element simulation reproduced the experimental stent deployment adequately, both by visual comparison and quantitative measurements. In the bifurcation region, however, a significant difference is obtained. Upon close inspection, it can be seen that this is mainly a rotation of the upper part of the iliac limb of the graft in the experimental situation. This might be caused by the operator slightly rotating the iliac limb during experimental deployment. It highlights, however, one of the challenges of performing EVAR simulations. Especially for the bifurcated and distal region of the endograft, the vascular surgeon can influence the stent placement. By pushing, pulling or rotating the delivery system after the proximal expansion and anchoring, the physician can change stent graft location.

Radial forces due to stent-graft oversizing in the proximal neck (4.2N for the presented stent-graft in this geometry) enable a good seal of the aneurysm and can compensate for aortic aneurysm neck dilatation. A too high oversize and consequent radial force may lead to the graft folding, compromising the seal, and might trigger aneurysm neck dilatation and related device migration[53]. Palombo et al. (2003) [174] concluded that long-term dilation was due to the continuous radial force of the self-expanding endograft acting on the proximal neck wall. Badran et al. (2002) [175] looked at changes in diameter after endovascular repair and found changes in diameter from 21.8 mm to 22.8 mm within 60 days. Similar results were obtained by Sampaio et al. (2006) [52], with an average post operative diameter increase of 1.45 and 1.1 mm for the AneurX (Medtronic, Minneapolis, Minnesota) and Ancure (Guidant, Menlo Park, California) stent grafts, within 30 days. When assuming the observed neck expansion in these studies is mainly due to the stent graft placement, we see our results fall just below these reported values, suggesting a realistic in vitro deployment of the device. Continuation of the disease can also contribute to neck dilatation, and the cyclic deformations of the aortic wall may influence the mechanics of deployment. Furthermore, the silicone material only approximates the complex behavior of the vessel tissue and at room temperature, the nitinol superelastic plateau stress is lower. In the studies by Badran et al. [175] and Sampaio et al. [52] a large variety of grafts, and thus radial forces, were used, making the reported outcomes more difficult to compare and elucidate. In future work, the presented method can be used as a tool to relate proximal neck dilatation to the radial forces associated with oversizing endografts.

A second important mechanical event occurs when the stent graft limbs of the endograft get occluded. Although the problem is relatively rare, it still occurs in 2.2 to 3.9 % of patients [141]. This can happen due to kinks or thrombosis as a late event. A recent study by Demanget et al. (2012) [107] simulated simple bending of stent graft iliac legs, showing that stent design can greatly influence bending behavior. Thrombosis may be caused by unfavorable flow alterations. These could be detected using case specific CFD simulations. The presented modeling procedure could be used to detect kinking of iliac legs in highly tortuous anatomies, and serve as a starting point for high end CFD or FSI calculations.

This study holds some limitations. First, only the Talent stent was considered. While this stent is still in use, it is being phased out and replaced with next generation stent grafts. Future work will attempt to repeat the method with the most frequently used devices, making the presented results more generally acceptable. The aneurysm geometry was, although realistic, not a challenging situation for EVAR, because the straight neck of the model could easily accomodate the stent graft. Angulated necks and stent graft apposition can influence proximal fixation greatly, and can, in future, be assessed using similar mechanical simulations. The in vitro model had realistic material properties, and deformations in range of those seen in vivo. However, pulsatile deformations of the aortic wall, caused by the cyclic blood pressure, are not taken into account. These could influence the mechanics of stent graft deployment. Cyclic deformations are the cause of fatigue stent strut breaks, and should be taken into account when investigating cyclic stress and strain patterns. For this modeling and validation study of stent graft deployment however, we deemed these limitations and simplifications as acceptable.

The model creation and deployment simulation techniques presented can be adjusted for use with human data. In future work we will focus on accurate modeling of the aortic tissue, including possible thrombus in the AAA and calcifications of the aortic wall. To be able to compare the simulations with the in vivo post operative situation, we will expand the simulations to model the entire procedure. Depending on the device and patient, this can involve the modeling of a contralateral iliac leg, and (ipsilateral) extenders. Mechanical tests on the temperature dependent nitinol material will be repeated at body temperature. Finally, cyclic deformations of the aneurysm wall and blood pressure acting on the stent graft will have to be taken into account when investigating stent fatigue.

5.5 CONCLUSION

The study presented assesses the deformed configuration of the Talent stent graft in a realistic abdominal aortic aneurysm via FE analysis. Visual and quantitative area increase comparisons between the simulated and experimental situation show good agreement at the proximal and distal fixation sites. Operator actions can change the deformed configuration of the stent graft at the bifurcation and distal location, making simulations of EVAR challenging. Though limited to a single stent graft design and one aortic geometry, the presented work confirms the capability of finite element computer simulations to predict the deformed configuration after EVAR. These simulations have the potential to be used to quantify mechanical parameters related to stent graft deployment, specific for each aorta geometry and device.

CHAPTER 6

In vivo case study of the virtual deployment of a stent graft device

In the previous chapter, a FE deployment method was validated in vitro. In the following chapter, we move forward to a patient specific case. In this zero-risk virtual environment, patient-specific geometries obtained from medical imaging can be considered. We present a method to virtually deploy a modular device in a patient-specific geometry with heterogeneous material properties. Using the finite element method, mechanics of the stent graft device and aortic vasculature are taken into account. The simulation qualitatively and quantitatively compares well with reconstructed post-operative CT images and reproduces the minor malapposition at the proximal neck due to the presence of calcifications and the ovalization of the two stent graft limbs.

This chapter is based on: “Virtual stent graft placement to investigate the mechanics of endovascular aortic aneurysm treatment: a patient specific case study” submitted for publication in the Journal of Biomechanics. The study was approved by the ethics committee of the Ghent University Hospital, Belgium (registration number B670201214459).

6.1 INTRODUCTION

Patients with an abdominal aortic aneurysm (AAA), a fusiform or saccular enlargement of the aorta, are frequently treated using endovascular repair (EVAR), especially when they present with multiple comorbidities.

The vasculatures of these mostly elderly patients often show considerable calcifications, tortuosity and thrombus formation. An increasing number of endovascular devices are being developed and approved for clinical use [58]. This leads to not only more AAA patients being treated with endovascular devices, but also an increased use of these devices beyond the instructions for use [143].

Computational biomechanics can play a role in engineering solutions for device design, device comparison and planning that considers patient-specific geometries and mechanical characteristics. Recently, a pilot study has shown that patient-specific rehearsal on virtual reality (VR) simulators prior to EVAR may be valuable in preparing the interventional team and in choosing optimal C-arm angles [176]. Hence, this PROcedure rehearsal software (Simbionix, Cleveland, Ohio) does not take into account the device or vessel wall mechanics, and relies on projection methods to visualize stent placement. Finite element analysis (FEA) can serve as a technology to improve the fidelity of VR simulators, or as the basis to build software with predictive capabilities.

Haigron et al. (2013) [110] have used FEA to compute vessel deformations during stiff guidewire insertion. Von Sachsen et al. (2013) [112] developed a visualization and planning tool for EVAR using FEA, calculating contact forces for individual stent rings of the Anaconda (Vascutek, Renfrewshire, Scotland) stent graft. Auricchio et al. (2013) [111] performed a computer based analysis for the treatment of an ascending pseudoaneurysm with a custom-made stent-graft. Finite element patient-specific simulation of the deployment of stents has been performed in coronary [177, 178] and carotid arteries [179, 180] and in virtual treatment of cerebral aneurysms [167, 181].

In this paper, we present a patient specific FEA study for a modular stent graft device consisting of a main body (trunk and ipsilateral iliac leg) and contralateral iliac limb. The presented deployment and modeling method was previously validated in vitro using a silicone phantom, on a relatively simple aneurysm geometry [140]. The previous work now moves to an in vivo case, with additional challenges in image processing, segmenting and mesh generation. The aortic geometry below the diaphragm is complex and includes the renal arteries, the bifurcation, the common iliac arteries, the external and internal iliac arteries. For this patient specifically, there is a large thrombus present in the fusiform aortic aneurysm, and a small thrombus in the left common iliac.

The complete modular device is deployed in two steps. The body of the stent-graft and the ipsilaterale limb are inserted on the right hand side. The body is deployed as close as possible to the lowest renal artery. Subsequently the contralateral gait is cannulated with a guide wire and selective catheter from the left side, followed by insertion and deployment of the contralateral limb.

We offer and demonstrate solutions to the specific issues concerning the virtual deployment of a stent graft into a patient-specific environment. The simulation is compared with post-operative imaging to evaluate the result.

6.2 MATERIAL AND METHODS

6.2.1 Stent graft geometry and material properties

The device used to treat the patient is a bifurcated Excluder (W.L.Gore and Associates, Flagstaff, Ariz.) stent graft. The metallic stent of the device is made from a Z-shaped helically wound nitinol wire. The proximal part consists of several wires, which end in outward pointing hooks for active fixation. Device geometry, material properties and finite element representation were obtained from a previous study [129]. Main body diameter was 26 mm. The contralateral leg was 14 cm long and had a diameter of 14.5 mm. The material properties of nitinol wire and ePTFE membrane were assumed identical to those of the ipsilateral leg.

6.2.2 Patient AAA geometry and material properties

The case presented was treated at the Ghent University Hospital, Belgium. After approval of the study by the ethics committee, anonymized pre and post-operative CT DICOM data was obtained. In plane CT resolution was 0.782 mm, with a 2 mm slice thickness. DICOM data slices were processed using Mimics (Materialize, Leuven, Belgium). The vessel lumen was clearly visible from CT angiography. Thresholding was used to segment the lumen and calcifications from the slices. Thrombus was manually segmented in every slice. Each slice was checked and lumen, calcification and thrombus masks were manually fixed if needed. These masks were exported as triangulated (STL) surfaces.

The vessel wall was discretized using a hexahedral meshing strategy adopted from [164]. The used mesh consisted of 18630 linear full integration hexahedrons with improved bending behavior (C3D8I). Wall thickness was visible on some slices, and around 3 pixels in width. Thickness was not visible everywhere, and the very calcified nature of the wall further encumbers an accurate wall thickness extraction. Since even a 1 pixel change could cause a 33% error, wall thickness was assumed constant at 1.9 mm [70]. Thrombus was discretized using 23700 linear tetrahedral elements, using the open source TetGen program (www.tetgen.org). Inner vessel wall and thrombus did not have coincident nodes, and were connected using a nodal tied constraint.

An anisotropic hyperelastic material (Holzaphel-Gasser-Ogden form) was used for the aortic and iliac artery tissue [72, 182], while an isotropic hypererlastic neo-Hookean material law was used to describe the behavior of intraluminal thrombus and calcifications [81]. Material behavior in uniaxial loading is shown in figure 6.1. Calcified arterial wall and thrombus material behavior was assigned to discrete mesh elements based on the segmented calcifications. The STL surface of the calcifications was converted into a point cloud. When a calcification point lay inside a (hexahedral or tetrahedral) element, this element was considered calcified. The artery mesh and material assignment is shown in figure 6.2.

Local material orientations, needed for an anisotropic formulation, are defined using distribution tables from element edge orientations [178]. The main directions are axial, circumferential and radial. The transition in orientation at the location of the aortic side branches is smoothed, but still had a discretization error (see figure 6.3).

6.2.3 Simulation strategy

Finite element analysis

FE simulations were performed using Abaqus/Explicit 6.13 in a quasi-static analysis. Mesh density was conservatively chosen based on previous work [140], and convergence was confirmed by doubling the amount of elements. Convergence criterion was the final resulting displacement field, resulting in a fairly coarse mesh for the aneurysm wall and thrombus (compared to the mesh that would be obtained when using a stress

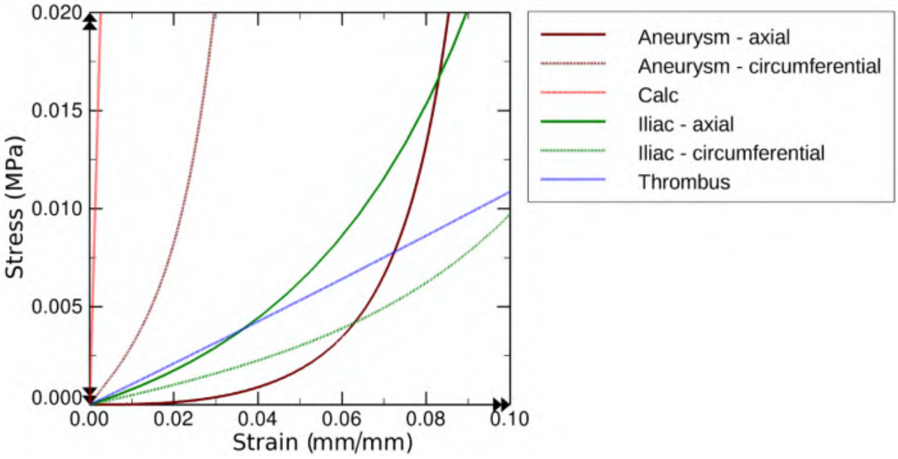

FIGURE 6.1: Material response to uniaxial tensile loading. For anisotropic material, circumferential and axial response are shown.

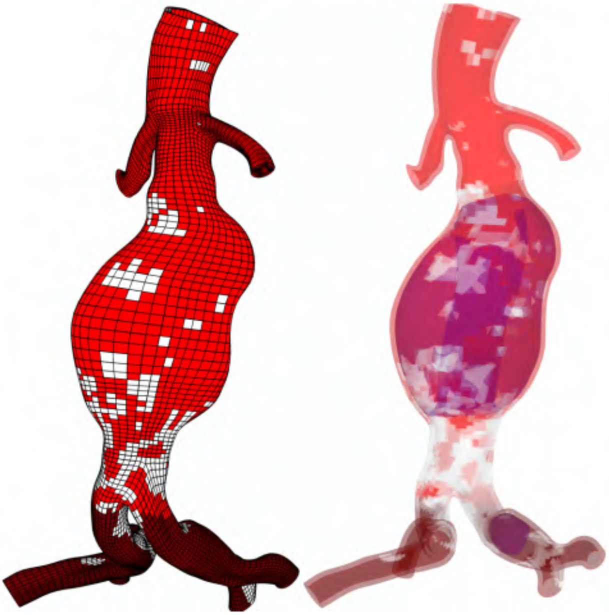

FIGURE 6.2: Visualisation of the finite element mesh, colored according to material assignment. Opaque view with element edges visible (left) and transparent view with visible thrombus (right). Materials are colored as follows: red - aorta; brown - iliac artery; white - calcification; purple - thrombus

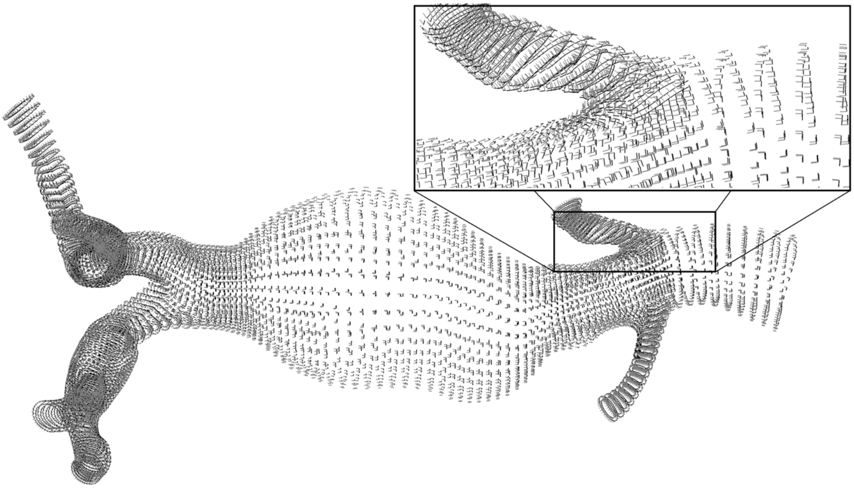

FIGURE 6.3: View of the local coordinate system of each element, needed for anisotropic material assignment. Zoomed window shows the discretization error where two arteries meet.

convergence criterion). The meshes of the stent and membrane were refined to ensure smoother contact between all components. With coarser meshes, the contact algorithm could fail during these complex deformation patterns of stent wires and surrounding graft material. The default contact algorithm – node to face and edge to edge contact with penalty enforcement – was expanded with fold inversion checking. This is an algorithm implemented in Abaqus, originally designed for airbag inflation simulations, which uses more local topological and geometric information in tracking contact between nodes and faces. This inclusion was needed to avoid contact convergence issues due to the sharp folds in the graft material. The final mesh consisted of 342182 elements.

A combination of time and mass scaling was used to speed up the simulation. Time was scaled until the ratio of kinetic and internal energy reached 5%. Subsequently, variable mass scaling of the smallest and stiffest elements was employed to increase the smallest stable time increment. Variable mass scaling was limited to be less than 1%. A small viscous surface load, proportional to the velocity, was added to both the aneurysm wall and graft surface to remove oscillations of these (light) structures. Viscous energy (including high frequency damping) was confirmed to be negligible (<5% of internal energy). The complete finite element model was constructed in pyFormex (www.pyformex.org), an open source geometrical modeling, pre and post-processing software.

Modular device virtual deployment method

To guide the stent to the deployment location, a similar strategy as in [140] is used. A deformable surface acts as the stent's delivery system, crimping and bending the stent graft through contact. For the in-vivo case here, three of these surfaces were used. A first surface for the deployment of the main body, and two surfaces to assist in the deployment of the contralateral leg. The simulation strategy was as described below, with steps indicated on figure 6.4.

Analysis 1

- Step 1 Main body is crimped and bent according to the centerline of the aneurysm and right iliac. This centerline is extracted from the lumen surface using vmtk (www.vmtk.org). Contact between the crimping surface and stent wire and graft is enabled. (A1 - A2)
- Step 2 Deployment of main body from proximal (top) to distal (down), mimicking the in vivo retraction of the delivery system. Contact between stent and all tissues (aneurysm wall, iliac artery walls, thrombus and calcifications) is enabled. (A2 - A4)

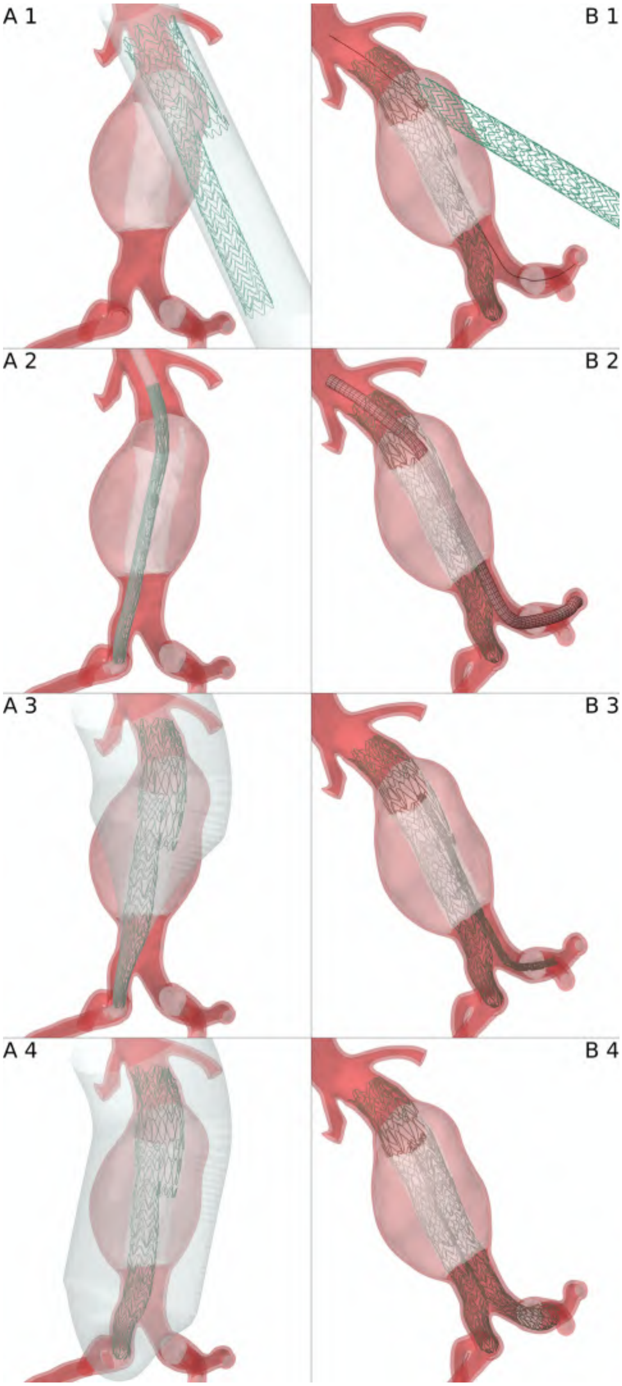

FIGURE 6.4: Modular device deployment method. Mainbody and ipsilateral leg (A) and contralateral leg (B).

- The analysis is ended, saving nodal displacement and stress and strain in material integration points.

- Deformation output is analyzed in pyFormex, the centerline of the lumen and left iliac leg is adjusted to run through the main body and the contralateral opening, using a manual picking of points on a graphical rendering of the deformed configuration, and a spline fit through these points.

Analysis 2

- The analysis is restarted from the previously saved point. Two more deformable surfaces and the contralateral leg are added to the finite element model

- Step 3 In a first, short step, one of the deformable surfaces (HELPSURF) is bent to the centerline calculated at the end of Analysis 1, without any contact enabled with any other material. The diameter of this deformable tube is very small (0.1 mm) (B1)

- Step 4 The contralateral endoprosthesis is crimped and bent using the other surface (DEPLOYSURF). During the same step, HELPSURF, put into position during step 3, expands to a diameter larger than the contralateral leg deployment system diameter. In this step, contact is enabled between stent leg and crimping surface DEPLOYSURF, and between HELPSURF and the previously deployed stent graft body, aneurysm and iliac artery walls, and thrombus. (B1 - B2)

- Step 5 The contralateral endoprosthesis is deployed, proximal to distal. HELPSURF is again reduced in diameter, at the end of this step, HELPSURF does not contact any other material. Contact between the contralateral leg and the stent main body, artery walls and thrombus is enabled. (B3 - B4)

The presented method offers a realistic deployment method that is computationally more efficient than pushing and retracting a deployment sheet, as the device is gradually deformed and released. The procedure was repeated few times at higher speed (higher kinetic energy) with different initial positions (distance from the renal artery) until the finite element deployed device was at approximately the same location as the in vivo deployed stent graft.

6.2.4 Data analysis

We qualitatively analyze global and local deformations, and compare these with the post-operative CT images. Quantitatively, we look at the ovalisation of the iliac stent graft limbs. In the region between abdominal aneurysm and the bifurcation to the iliac arteries, the iliac limbs are confined by the aortic wall, which is highly calcified. Placing two circular tubes in this circular, stiff passageway causes them to compress laterally and become oval in shape. We quantified this ovalization by measuring the two axes (major and minor) over 3 slices - top, middle and bottom of this region. Measurements were performed five times by a single operator and an additional time by five different operators.

FE measurements were automatically performed using a script in the pyFormex postprocessor. Taken at the same location as the CT measurements, the measurements were repeated 5 times in 0.4 mm steps and averaged.

6.3 RESULTS

The complete simulation strategy ran for 18 hours on 16 (2·8) 3.4GHz CPU cores on a high performance computing cluster.

6.3.1 Global qualitative comparison

We present a side-by-side comparison of the post-operative in vivo result, from medical imaging, and the finite element deployment (figure 6.5). Visual comparison was performed in the pyFormex post-processing software, loading FEA and post operative CT images. By study design, the positioning of the device is similar, with comparable lengths of main body and contralateral limb.

6.3.2 Qualitative and quantitative comparison of stent deployment

The location of major interest in EVAR is the proximal neck, where good anchoring and sealing of the stent graft is essential to obtain technical success. When qualitatively comparing in vivo and simulation post-operative data, a noticeable malapposition of the proximal stent can be observed at the inner curvature of the angle (figure 6.6). Not only does the simulation capture this deformation effect, it can be used to offer better insight in the reasons for this badly apposed strut. When displaying contact forces between stent and aneurysm wall (figure 6.7), it can be noted that the inner curve - including a large calcification - acts as a fulcrum for the relatively stiff device (indicated in green in figure 6.6). While the outer curve shows a more even distribution of contact

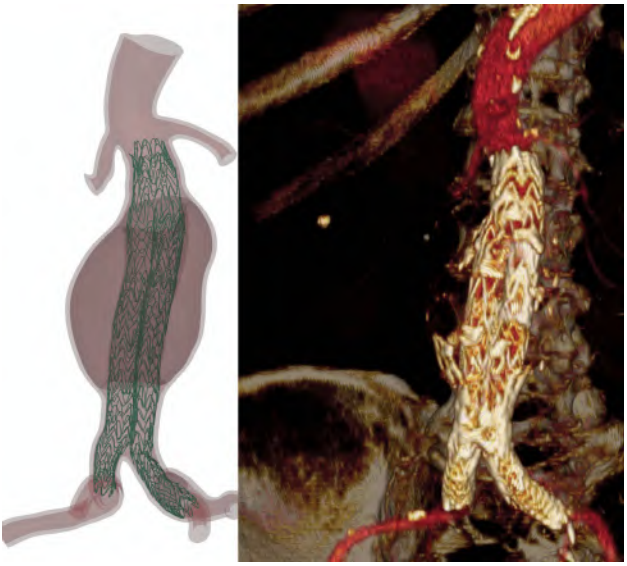

Figure 6.5: Global comparison of post operative in vivo and finite element simulation result

forces, the inner curve has a large and localized concentration of force vectors. This small malapposition (indicated in red in figure 6.6 and 6.7) occurs above the location of the hooks and had no short term clinical consequences concerning migration or endoleakage.

A second observation noted during processing of the simulation data is the ovalisation of the stent graft limbs in the distal aorta (figure 6.8).

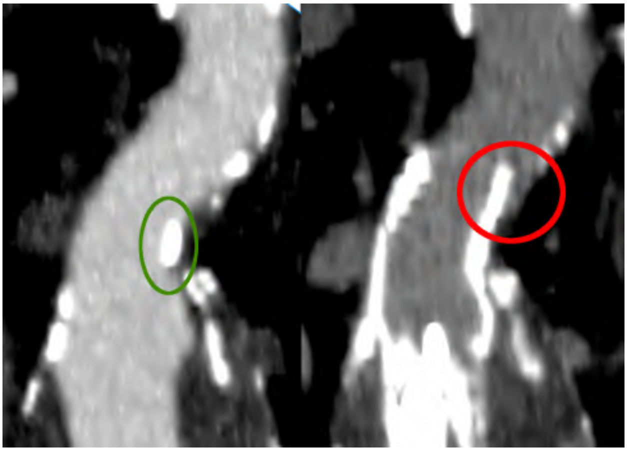

Figure 6.6: Pre (left) and post (right) operative imaging of the proximal neck location. A stent strut malapposition is indicated in red. A calcification in the inner curvature is indicated in green.

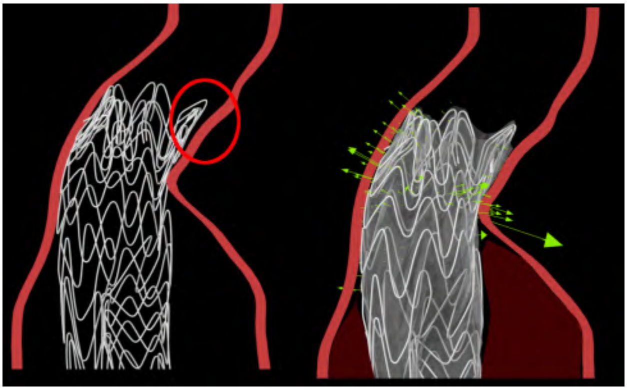

FIGURE 6.7: Rendering of the deformed simulation result. Left shows the malapposition indicated in red. On the right, contact force vectors are drawn, showing the heterogeneous distribution

Measurements after the finite element deployment, together with intra - and interobserver variability are shown on figure 6.9. For all but one measurement, the major axis of the left iliac limb at the middle of the aorta distal to the aneurysm, the finite element result falls within the observer variability (displayed as the mean +- two times the standard deviation).

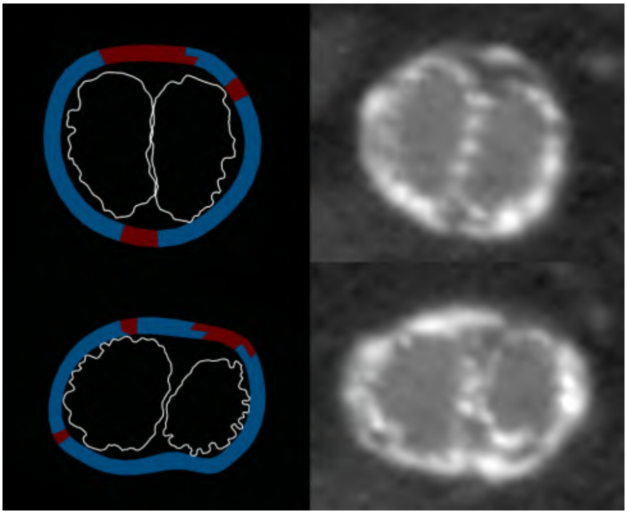

FIGURE 6.8: Ovalisation of the stent graft limbs at the location between aneurysm and bifurcation, shown for finite element result (left) and CT images (right)

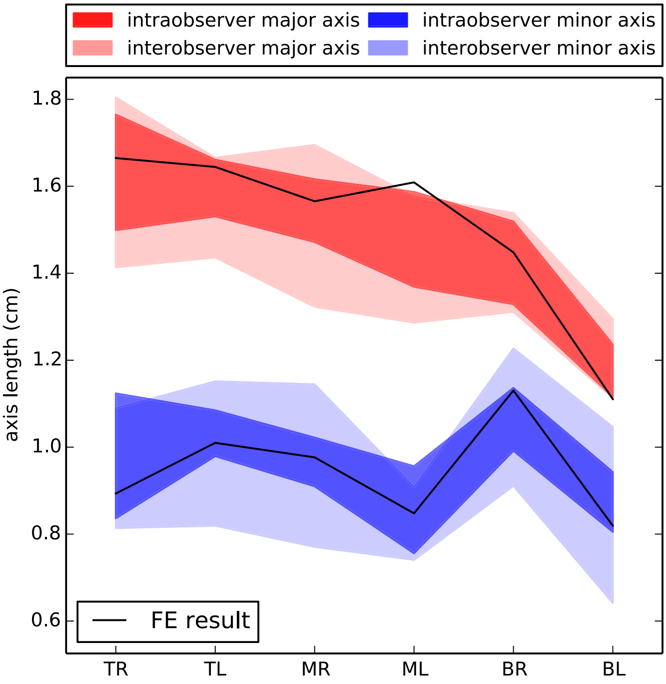

Figure 6.9: Major (red) and minor (blue) axis lengths for 6 measurements: top (T), middle (M) and bottom (B) for the left (L) and right (R) stent graft leg. Finite element simulation results are shown in black, in vivo measurements in color. Intra and interobserver variations are displayed by the colored surfaces which show the mean +- two times the standard deviation.

6.4 Discussion

In this work, we present the patient-specific in silico deployment of a modular abdominal aortic stent graft. This study builds on previous work by our group on generating accurate mechanical finite element models of different clinically used devices [129]. The finite element device deployment was previously validated in vitro, taking advantage of the higher achievable image resolution, simpler geometry and deployed device, uniform material characteristics of the arterial model and stable conditions [140].

Biomechanical studies on stent graft mechanics have, in a short window of time, moved from idealized device and aneurysm geometry models to a prototype planning tool for endoprosthesis sizing. Kleinstreuer et al. (2008) [105] first investigated mechanical and fatigue behavior of a generic stent graft device, including a finite element deployment in a straight tube. Prasad et al. (2012) [106] investigated positional stability using computational fluid dynamics to calculate loads for a finite element generic stent design, deployed in an idealized AAA geometry. Demanget et al. published multiple papers [65, 107, 108] on the subject of the bending behavior of iliac limbs using device specific geometries and realistic (but equal) material properties. This resulted in a comparison of the unconstrained bending for eight marketed stent graft devices [108]. Finally, Von Sachsen et al. (2013) [112] developed a post-processor for a finite element simulation of stent ring crimping. Unfortunately, information on the finite element analysis is lacking, but from the paper we deduct that the vessel wall is assumed rigid, and each stent ring is deployed individually.

To the best of our knowledge, the result presented is the most advanced simulation of a patient-specific stent graft deployment to date. Great attention has been paid in accurately modeling these composite (stent + graft) devices in both geometry and mechanical behavior. Furthermore, we simulate the deployment of a modular device, presenting a method closely mimicking the endovascular procedure, but computationally optimized for faster simulation times. The aneurysm under investigation is a patient-specific abdominal aorta geometry, including renal and iliac arteries and thrombus in both aortic aneurysm and one iliac. Similar to groups investigating aneurysm rupture risk [76], we utilize complex and non-uniform materials in the aortic wall and thrombus, using the finite element discretization to select and assign elements a higher, calcified stiffness. Because in this case the aneurysm region was heavily calcified, deformations were mostly defined and limited by the stiff calcified locations.

The patient-specific finite element device deployment shows good agreement with the post-operative images, and is capable of capturing important qualitative details of the deployment and apposition of the device, also visible on CT images. A limited quantitative comparison between finite element and post-operative images indicates difficulties when working with in vivo imaging, but still shows the ability to detect trends: e.g. the reduced diameter of the left iliac limb compared to the right for the bottom slice investigated in the lower part of the aorta (figure 6.9). Intra and interobserver variability is high in the post-operative CT measurements. Significant differences can have many explanations. When considering the major limiting factor, an in plane resolution of 0.782 mm, an oversize in the lumen mask border of 1 pixel would already overestimate the measurements by 1.5 mm. Changes in blood pressure between the two scan times, positional changes and errors in computational modeling are additional factors influencing the result. Quantitative comparison is also hindered by the resolutions of the diagnostic scans and the scattering of x-ray beams by the metallic stent struts and radio-opaque markers. This prohibits validation methods with continuous area measurements as we previously applied for the in vitro case.

6.4.1 Limitations

The main limitations in the presented work directly stem from limitations associated with the use of in vivo data (limited resolution, scan artifacts due to the stent, uncertainties about the stability of the hemodynamic conditions between pre- and post-op scan). Also, the endovascular specialist can actively alter the deployment behavior of the endoprosthesis. As shown in [110], the insertion of a stiff guidewire can alter tortuous vessel geometry. Molding of the landing and overlap zones and forces exerted on the deployment system can also alter the final result. In this aspect, our simulation can be viewed as the calculation of one possible mechanical equilibrium between a relatively stiff, composite device, and a heterogeneous aortic vasculature. The numerical simulation could be improved by including pre-stressing of the geometry, as the CT images are obtained with the aneurysm under (an unknown) blood pressure. More complexity is, however, not always wanted or required. Many different simplified simulation strategies have been used in the studies previously discussed. Others have treated the stent graft device as a homogeneous structure [115, 183], or have considered a 2D case [123] to investigate complications of EVAR. Each method, regardless of computational complexity, has advantages or disadvantages in implementation, ease of interpretation and level of accuracy. In our opinion, however, rather than further refining the numerical method (e.g. FSI methods and pre-stressing), more is to be gained from improved imaging resolution or modalities, such as 3D or 4D ultrasound and magnetic resonance imaging (for MRI conditional devices). 4D imaging, for instance, could be used to find patient-specific compliances of the aortic neck and aneurysm regions [173]. Engineers have to assess which tool to use for which objective, and at what (computational) cost. The presented method can serve as a validation method for less complex and faster computational methods (e.g. projection or mesh-less methods), to retrospectively analyze failure cases and in device selection and sizing for complex cases. Finally, the shown finite element procedure can be used by design engineers to gain insight into device mechanics and the interaction with the heterogeneous deployment environment.

Four

Conclusions

Chapter 7

Conclusions and future perspectives

In the following chapter we conclude this work. The methodological improvements realised within this PhD are listed and results briefly summarized. Insights into stent graft design are shared. At the end of the chapter, several unresolved research questions are posed and suggestions for further steps in biomechanical stent graft research are given.

7.1 STUDY CONCLUSIONS

At the start of this project, four years ago, little information was available in the public domain on the (mechanical) characteristics of stent graft devices. Continuing the work of our department [184–186] on the biomechanics of stents, the study aimed to investigate covered stents used in the treatment of AAAs. This presented challenges in determining the mechanical behavior of these composite devices (stent + graft). Additionally, AAA geometries are relatively complex, with multiple branching vessels, the bifurcation, and possible thrombus in the aneurysm sac, while the biomechanical behavior of these tissues can have varying degrees of anisotropy and heterogeneity.

7.1.1 Computational mechanics of stent graft devices

Visual inspection of device samples showed that these hand made devices are not regular nor perfectly circular. A first step in determining the mechanical behavior of these devices was getting an accurate geometrical representation. Chapter 2 details the extraction of wire centerlines from μCT scans of the samples, and the close fitting of the graft to the stent rings. While the obtained computer models are accurate representations of commercially used devices, some geometrical simplifications were needed, which are discussed at the end of chapter 2.

Also, to the best of our knowledge, this study was the first to examine the mechanical behavior of commercial stent grafts. We employed a combined experimental and numerical method to examine the mechanical response of 4 commercially available stent grafts (chapter 3). Two bench top mechanical tests were performed: a flat plate compression test and a radial crimping of the devices. An inverse analysis, repeating the tests using FEA, enabled the calibration of each device's material properties. Making use of two independent experiments and the known material properties of stainless steel, we were able to validate this novel method for non-destructive extraction of device material properties. A parameter study revealed the importance of including the stent graft fabric when determining the mechanical behavior of stent grafts. The relation between device design and radial stiffness of the devices was discussed, and devices were objectively compared.

An accurate *in silico* representation of a medical device can be used for fast, inexpensive and zero-risk investigations. The (elevated) risks for treatment of AAA patients by EVAR outside the IFU are not clear. Heterogeneity in devices used and patient AAA anatomy make it difficult to compare and interpret clinical studies on the topic. A missing factor in the discussion is the mechanical behavior of each specific device. Chapter 4 takes advantage of the constructed FE model of the Zenith LP device to investigate the forces and deformations associated with stent graft deployment in geometrically different proximal aneurysm necks. Angulations, neck lengths and device oversize are varied, and the influence on the result was calculated. Stent apposition, area reduction of the graft, asymmetry of contact forces and the sealing capabilities of the stent graft were the metrics under investigation. A combination of the risk factors (high angulation and short landing zones) caused the most adverse affects. A higher oversize alleviated the unwanted consequences, but only by a small amount. For high bending angles ($>60°$), proximal kinking of the device can occur, and proximal stent struts can bend asymmetrically and group at the outer curve. In short, chapter 4 demonstrates the power of computational investigation of device mechanics, and adds the mechanical behavior of a device to the discussion on the geometrical limits for stent graft deployment.

7.1.2 Virtual EVAR: simulating the deployment of a stent graft

Parametric and simplified vessel geometries are fast to use and make it easy to compare results. However, specific patients can have complex AAA morphology, for which these simplified simulations are not adequate. To be able to virtually examine stent graft deployment in a patient specific situation, a FE methodology was devised. Chapter 5 details the virtual deployment of a bifurcated stent graft (Medtronic Talent) in an Abdominal Aortic Aneurysm model. The entire deployment procedure is modeled, with the stent graft being crimped and bent according to the vessel geometry, and subsequently released. The finite element results are validated in vitro with placement of the device in a silicone mock aneurysm, using high resolution CT scans to evaluate the result. The presented work confirms the capability of finite element computer simulations to predict the deformed configuration after EVAR.

Techniques and results from all previous chapters come together in the final chapter. After the *in vitro* validation, the virtual EVAR is moved forward to an *in vivo*, patient specific case study. Medical images (CT and CTA) were processed and segmented. The modeled geometry includes the renal arteries, the bifurcation, the common iliac arteries, the external and internal iliac arteries, a large thrombus in the fusiform aortic aneurysm, and a small thrombus in the left common iliac. Meshes were generated for use in the FE simulation. Heterogeneous material properties are assigned to the different structures. The simulation compares well with the post-operative CT, and shows the capability of the method to obtain realistic deformations.

7.2 STENT DESIGN: CHALLENGES AND INSIGHTS

The sole purpose of a stent graft is sealing the aneurysm sac from the pulsatile blood flow and pressure. Unfortunately, to achieve this, a large number of challenges and possible problems have to be addressed.

A first design objective is getting the stent graft at the location it needs to be. Repositionable devices are already available, and future improvements will surely include fully retractable stent grafts and steerable catheters.

A too large delivery system diameter excludes a lot of patients from EVAR, and can increase the risk of femoral artery hematoma or bleeding. Hydrophilic coating of the delivery system and material choices can influence this diameter, but ultimately, the stent graft design and crimped diameter is the limiting factor.

Challenging and varying anatomies force the device to be sufficiently flexible so it can follow the anatomic curvature. Stiffer designs could however be easier to implant, and give the vascular surgeon more control.

During pre-operative planning, only the stent graft size is determined on a patient specific basis. For fenestrated devices, patient specific modifications are made according to the measured locations of the renal and mesenteric arteries. An obvious direction for future improvement is a patient specific shape setting of the device. With each device made to follow the anatomy as measured on CT imaging.

The actual sealing of the aneurysm is achieved by the radial force of the stent, exerted onto the vessel wall and ensuring good apposition of the graft. An additional objective in designing a stent graft is therefore achieving sufficient radial force, keeping in mind that excessive forces can accelerate neck dilatations.

Once sealed, the device has to remain in place. Hooks and barbs do a sufficient job in anchoring the stent graft, but migration can still occur, especially when devices are used outside the IFU. Design changes to limit the displacement forces, such as tapered grafts and a gradual bifurcation to the iliac arteries could be incorporated in current stent grafts.

Lasercut stent graft designs might offer advantages over wire stents. The practically unlimited freedom in geometrical design could be explored to optimize new stent graft designs. Radial forces, flexibility, design sealing characteristics, stability, minimal crimping diameter, fatigue properties and various other factors have to be balanced. Computational techniques, coupled with in vitro validation and calibration, can be used to optimize these characteristics in a systematic and analytical way. In this thesis, modeling and computational challenges were tackled. Designs were compared and the use of computational techniques for parametric, in vitro and in vivo studies on stent graft mechanics was demonstrated.

An important but unknown factor is the optimization goal. What are suitable radial forces, high enough to seal the aneurysm, but low enough not to damage the vessel or induce dilatation of the proximal neck? Are the most flexible devices the best, or is some stiffness required to give surgeons more control during deployment? How do we balance contrasting factors such as radial stiffness, longitudinal flexibility, low crimping diameters and fatigue safety factors? Or translated to a mathematical optimization problem, what weighting factors do we give to the different (computationally calculated) factors and metrics. More animal and clinical trials, backed up with mechanical calculations, are needed to establish limits and preferable ranges on these heterogeneous issues.

7.3 FUTURE PERSPECTIVES

The research undertaken for this project is a mixture of fundamental research on advanced modeling techniques, and directly applicable data acquisition on device geometry and mechanics. Endovascular stent devices, and stent grafts in particular, have a complex, non-linear mechanical behavior, and are implanted at regions with irregular geometries and heterogeneous viscoelastic behavior. To fully understand and predict the complete device in vivo behavior, more fundamental and applied investigations are needed prerequisites.

The proposed and validated deployment method can be used on a cohort of patients, including cases with device related complications, to establish the influence of specific mechanical parameters and device characteristics on EVAR outcome. We foresee uses in retrospectively analyzing failure cases with the goal of finding the root cause of each device failure. In (randomized controlled) clinical trials, the use of mechanical simulations and virtual EVAR could serve as a tool to eliminate part of the variability caused by the use of different device designs and receiving vessel geometries. Including the mechanical behavior of the device and vasculature in training simulators could increase the fidelity of these simulators, and increase their use as a pre-operative planning tool.

The fabric, covering the stent rings, is modeled in a macromechanical way, with material properties fixed to reflect the mechanical response to the flat plate and radial crimp test. To accurately model fabric failure, the anisotropic behavior of the woven structure should be taken into account. As local stresses and contact with the stent struts are the most likely causes of failure, weave, thread and abrasion properties will be crucial in determining and predicting fabric failure modes. The grafts can be coated (e.g. with albumin or heparin) to improve the endothelial cell adhesion or thrombogenicity of the graft.

While we have determined the mechanical response of the devices to flat plate and radial compression, we did not touch upon the subject of stent strut fatigue breaks. Data is needed on the fatigue properties of endovascular devices. Accelerated fatigue tests on specimens are the only reliable (yet expensive) method to obtain these data, as nitinol grade and surface finishing can greatly influence the fatigue behavior. Computational analysis can then be used to calculate a factor of safety for each geometry, based on the mean strain after deployment, and the alternating strain caused by the varying blood pressure.

Finally, the demonstrated techniques and data processing can be directly transferred to related devices, such as thoracic stent grafts, fenestrated stent grafts and stent grafts for use in the superficial femoral artery.

As a finalizing remark, I present (or remind) readers and researchers on the difficulties of the modeling paradox. We use computer models, mostly to make predictions where no experimental data can (or is too expensive to) be obtained. Computer models are simplified, and assumptions are made. Only part of the reality can be incorporated in the model, making abstractions for all remaining portions. When we "validate" our models, we don't validate the original points and values of interest, as these are not feasibly tested experimentally. In validation, we only replicate an area of interest that can be found through the experiment.

The paradox lies in the fact that we use the model beyond the validated domain, and there is no way to validate this use, because if there was, there would be no need for computational testing to begin with. Dealing with this paradox is threading on a thin line, and for fair and prudent use, limitations should always be kept in mind.

Supplementary data to chapter 4

Apposition 1st segment ~ diameter + angle + translation

Coefficients:

	Estimate	Pr(>|t|)	
(Intercept)	-0.848	0.0792	.
diameter	0.025	0.1890	
angle	0.005	0.0010	**
translation	0.015	0.0005	***

Adjusted R-squared: 0.3509
p-value: 6.052e-05

Apposition 1st segment ~ diameter + angle + translation + diameter*angle + diameter*translation + translation*angle

Coefficients:

	Estimate	Pr(>|t|)	
(Intercept)	-0.8480	0.0236	*
diameter	0.0246	0.0884	.
angle	0.0050	4.07e-05	***
translation	0.0153	1.33e-05	***
di:an	0.0010	0.1345	
di:tr	0.0039	0.0363	*
an:tr	0.0007	5.38e-06	***

Adjusted R-squared: 0.6209
p-value: 1.593e-08

Apposition 2nd segment ~ diameter + angle + translation

Coefficients:

	Estimate	Pr(>|t|)	
(Intercept)	-0.036	0.9550	
diameter	0.013	0.6031	
angle	0.014	2.68e-09	***
translation	0.021	3.56e-04	***

Adjusted R-squared: 0.5895
p-value: 3.127e-09

Apposition 2nd segment ~ diameter + angle + translation + diameter*angle + diameter*translation + translation*angle

Coefficients:

	Estimate	Pr(>|t|)	
(Intercept)	-0.0360	0.9315	
diameter	0.0129	0.4299	
angle	0.0141	3.49e-14	***
translation	0.0210	6.17e-07	***
di:an	0.0027	5.72e-04	***
di:tr	0.0042	0.0499	*
an:tr	0.0010	7.12e-08	***

Adjusted R-squared: 0.8228
p-value: 4.188e-15

Signif. Codes: 0 ‘***’ 0.001 ‘**’ 0.01 ‘*’ 0.05 ‘.’ 0.1 ‘ ’ 1
Pr(>|t|): p-value (t-test significance test)
di – diameter
an – angle
tr – translation

```
Area reduction ~ diameter + angle + translation

Coefficients:
              Estimate       Pr(>|t|)
(Intercept)   -0.0790           0.398
diam           0.0044           0.227
angle          0.0028        7.14e-13      ***
trans          0.0003           0.685

Adjusted R-squared:   0.6764
p-value:              1.764e-11
```

```
Area reduction ~ diameter + angle + translation + diameter*angle +
  diameter*translation + translation*angle

Coefficients:
              Estimate       Pr(>|t|)
(Intercept)    -0.0790          0.349
diam            0.0044          0.181
angle           0.0028       6.67e-14      ***
trans           0.0003          0.652
di:an           0.0005          0.001      **
di:tr          -0.0002          0.660
an:tr         2.73e-05          0.397

Adjusted R-squared:   0.7375
p-value:              1.113e-11
```

```
Force asymmetry ~ diameter + angle + translation

Coefficients:
              Estimate       Pr(>|t|)
(Intercept)   -1.304         6.88e-08      ***
diam           0.054         2.16e-08      ***
angle          0.003         7.53e-06      ***
trans          0.012         4.02e-09      ***
Adjusted R-squared:   0.7229
p-value:              5.997e-13
```

```
Force asymmetry ~ diameter + angle + translation + diameter*angle +
  diameter*translation + translation*angle

Coefficients:
              Estimate       Pr(>|t|)
(Intercept)   -1.3044        1.69e-08      ***
diam           0.0537        5.10e-09      ***
angle          0.0031        2.33e-06      ***
trans          0.0126        9.06e-10      ***
di:an         -0.0003           0.337
di:tr          0.0011           0.243
an:tr          0.0002           0.007      **
Adjusted R-squared:   0.7628
p-value:              1.47e-12
```

```
Signif. codes:  0 ‘***’ 0.001 ‘**’ 0.01 ‘*’ 0.05 ‘.’ 0.1 ‘ ’ 1
```

Pr(>|t|): p-value (t-test significance test)
di – diameter
an – angle
tr – translation

```
Path cost ~ diameter + angle + translation

Coefficients:
        diameter                angle           translation
        0.472                   0.216           0.091

Intercepts:
        19|219          219|419         419|619         619|1019
        14.70           17.21           18.07           19.46

Analysis of Deviance Table (Type II tests)

                        Pr(>Chisq)
diameter                   0.012        *
translation             3.02e-06        ***
angle                   2.02e-08        ***
```

```
Path cost ~ diameter + angle + translation + diameter*angle +
  diameter*translation + translation*angle

Coefficients:
        diameter                translation             angle
        -0.406                  -0.211                  -0.441
        diameter:translation    diameter:angle          translation:angle
        0.012                   0.020                   0.004

Intercepts:
        19|219          219|419         419|619         619|1019
        -8.21           -5.72           -4.83           -3.25

Analysis of Deviance Table (Type II tests)

                        Pr(>Chisq)
diameter                   0.008        **
translation             1.23e-06        ***
angle                   2.38e-08        ***
diameter:translation       0.691
diameter:angle             0.046        *
translation:angle          0.145
```

Signif. Codes: 0 ‘***’ 0.001 ‘**’ 0.01 ‘*’ 0.05 ‘.’ 0.1 ‘ ’ 1
Pr(>Chisq): p-value (chi-square likelihood ratio test)

Bibliography

[1] Team Gegevensverwerking en Resultaatsopvolging, Sterfte door ziekten van het hart- en vaatstelsel. beschikbaar op: `http://www.zorg-en-gezondheid.be/cijfers/` [geraadpleegd op 18-02-2014], Vlaams Agentschap Zorg en Gezondheid, Afd. Informatie en Ondersteuning (2011).

[2] K. W. Johnston, R. B. Rutherford, M. D. Tilson, D. M. Shah, L. Hollier, J. C. Stanley, Suggested standards for reporting on arterial aneurysms, Journal of Vascular Surgery 13 (1991) 452–458.

[3] N. Sakalihasan, R. Limet, O. Defawe, Abdominal aortic aneurysm, The Lancet 365 (2005) 1577–1589.

[4] R. M. Greenhalgh, J. T. Powell, Endovascular repair of abdominal aortic aneurysm, New England Journal of Medicine 358 (2008) 494–501.

[5] M. K. Yii, Epidemiology of abdominal aortic aneurysm in an asian population, Australian and New Zealand Journal of Surgery 73 (2003) 393–395.

[6] F. A. Lederle, The rise and fall of abdominal aortic aneurysm, Circulation 124 (2011) 1097–1099.

[7] A. Zankl, H. Schumacher, U. Krumsdorf, H. Katus, L. Jahn, et al., Pathology, natural history and treatment of abdominal aortic aneurysms, Clinical Research in Cardiology 96 (2007) 140–151.

[8] P. Dobrin, R. Mrkvicka, Failure of elastin or collagen as possible critical connective tissue alterations underlying aneurysmal dilatation., Cardiovascular Surgery 2 (1994) 484–488.

[9] A. Lopez-Candales, D. R. Holmes, S. Liao, M. J. Scott, S. A. Wickline, R. W. Thompson, Decreased vascular smooth muscle cell density in medial degeneration of human abdominal aortic aneurysms., The American Journal of Pathology 150 (1997) 993–1007.

[10] H. Ashton, M. Buxton, N. Day, L. Kim, T. Marteau, R. Scott, S. Thompson, N. Walker, et al., The multicentre aneurysm screening study (mass) into the effect of abdominal aortic aneurysm screening on mortality in men: a randomised controlled trial., Lancet 360 (2002) 1531–1539.

[11] T. G. Costantino, E. C. Bruno, N. Handly, A. J. Dean, Accuracy of emergency medicine ultrasound in the evaluation of abdominal aortic aneurysm, The Journal of Emergency Medicine 29 (2005) 455–460.

[12] J. Powell, Final 12-year follow-up of surgery versus surveillance in the uk small aneurysm trial, British Journal of Surgery 94 (2007) 702–708.

[13] F. A. Lederle, S. E. Wilson, G. R. Johnson, D. B. Reinke, F. N. Littooy, C. W. Acher, D. J. Ballard, L. M. Messina, I. L. Gordon, E. P. Chute, et al., Immediate repair compared with surveillance of small abdominal aortic aneurysms, New England Journal of Medicine 346 (2002) 1437–1444.

[14] J. Cervantes, Reflections on the 50th anniversary of the first abdominal aortic aneurysm resection, World Journal of Surgery 27 (2003) 246–248.

[15] C. Dubost, M. Allary, N. Oeconomos, Resection of an aneurysm of the abdominal aorta: reestablishment of the continuity by a preserved human arterial graft, with result after five months, Archives of Surgery 64 (1952) 405.

[16] A. Schanzer, L. Messina, Two decades of endovascular abdominal aortic aneurysm repair: enormous progress with serious lessons learned, Journal of the American Heart Association 1 (2012) e000075.

[17] J. Parodi, J. Palmaz, H. Barone, Transfemoral intraluminal graft implantation for abdominal aortic aneurysms, Annals of Vascular Surgery 5 (1991) 491–499.

[18] M. L. Schwarze, Y. Shen, J. Hemmerich, W. Dale, Age-related trends in utilization and outcome of open and endovascular repair for abdominal aortic aneurysm in the united states, 2001-2006, Journal of Vascular Surgery 50 (2009) 722–729.

[19] P. R. Nelson, Z. Kracjer, N. Kansal, V. Rao, C. Bianchi, H. Hashemi, P. Jones, J. M. Bacharach, A multicenter, randomized, controlled trial of totally percutaneous access versus open femoral exposure for endovascular aortic aneurysm repair (the PEVAR trial), Journal of Vascular Surgery (2014).

[20] J. L. De Bruin, A. F. Baas, J. Buth, M. Prinssen, E. L. G. Verhoeven, P. W. M. Cuypers, M. van Sambeek, R. Balm, D. E. Grobbee, J. D. Blankensteijn, Long-term outcome of open or endovascular repair of abdominal aortic aneurysm, New England Journal of Medicine 362 (2010) 1881–1889.

[21] F. J. V. Schlösser, R. J. Gusberg, A. Dardik, P. H. Lin, H. J. M. Verhagen, F. L. Moll, B. E. Muhs, Aneurysm rupture after EVAR: can the ultimate failure be predicted?, European Journal of Vascular and Endovascular Surgery 37 (2009) 15–22.

[22] T. Jacobs, V. Teodorescu, N. Morrissey, A. Carroccio, S. Ellozy, M. Minor, L. H. Hollier, M. L. Marin, The endovascular repair of abdominal aortic aneurysm: an update analysis of structural failure modes of endovascular stent grafts, Seminars in Vascular Surgery 16 (2003) 103–112.

[23] C. K. Zarins, F. R. Arko, T. Crabtree, D. A. Bloch, K. Ouriel, R. C. Allen, R. A. White, Explant analysis of AneuRx stent grafts: relationship between structural findings and clinical outcome, Journal of Vascular Surgery 40 (2004) 1–11.

[24] R. B. Rutherford, Structural failures in abdominal aortic aneurysm stentgrafts: Threat to durability and challenge to technology, Seminars in Vascular Surgery 17 (2004) 294–297.

[25] W. S. Moore, R. B. Rutherford, et al., Transfemoral endovascular repair of abdominal aortic aneurysm: results of the North American EVT phase 1 trial, Journal of Vascular Surgery 23 (1996) 543–553.

[26] H. G. Beebe, J. L. Cronenwett, B. T. Katzen, D. C. Brewster, R. M. Green, Results of an aortic endograft trial: impact of device failure beyond 12 months, Journal of Vascular Surgery 33 (2001) 55–63.

[27] T. S. Jacobs, J. Won, E. C. Gravereaux, P. L. Faries, N. Morrissey, V. J. Teodorescu, L. H. Hollier, M. L. Marin, Mechanical failure of prosthetic human implants: a 10-year experience with aortic stent graft devices, Journal of Vascular Surgery 37 (2003) 16–26.

[28] F. J. Criado, R. M. Fairman, G. J. Becker, Talent LPS AAA stent graft: results of a pivotal clinical trial, Journal of Vascular Surgery 37 (2003) 709–715.

[29] J. S. Matsumura, D. C. Brewster, M. S. Makaroun, D. C. Naftel, A multicenter controlled clinical trial of open versus endovascular treatment of abdominal aortic aneurysm, Journal of Vascular Surgery 37 (2003) 262–271.

[30] T. A. Chuter, J. C. Parodi, M. Lawrence-Brown, Management of abdominal aortic aneurysm: A decade of progress, Journal of Endovascular Therapy 11 (2004) II–82–II–95.

[31] M. Desai, J. Eaton-Evans, C. Hillery, R. Bakhshi, Z. You, J. Lu, G. Hamilton, A. M. Seifalian, AAA stent-grafts: past problems and future prospects, Annals of Biomedical Engineering 38 (2010) 1259–75.

[32] A. Carroccio, P. L. Faries, N. J. Morrissey, V. Teodorescu, J. A. Burks, E. C. Gravereaux, L. H. Hollier, M. L. Marin, Predicting iliac limb occlusions after bifurcated aortic stent grafting: anatomic and device-related causes, Journal of Vascular Surgery 36 (2002) 679–684.

[33] F. Cochennec, J. Becquemin, P. Desgranges, E. Allaire, H. Kobeiter, F. Roudot-Thoraval, Limb graft occlusion following evar: clinical pattern, outcomes and predictive factors of occurrence, European Journal of Vascular and Endovascular Surgery 34 (2007) 59–65.

[34] S. C. Krämer, H. Seifarth, R. Pamler, T. Fleiter, J. Görich, Geometric changes in aortic endografts over a 2-year observation period, Journal of Endovascular Therapy 8 (2001) 34–38.

[35] R. M. Greenhalgh, L. C. Brown, G. P. Kwong, J. T. Powell, S. G. Thompson, EVAR trial participants, Comparison of endovascular aneurysm repair with open repair in patients with abdominal aortic aneurysm (EVAR trial 1), 30-day operative mortality results: randomised controlled trial, Lancet 364 (2004) 843–848.

[36] United Kingdom EVAR Trial Investigators, R. M. Greenhalgh, L. C. Brown, J. T. Powell, S. G. Thompson, D. Epstein, M. J. Sculpher, et al., Endovascular versus open repair of abdominal aortic aneurysm, The New England Journal of Medicine 362 (2010) 1863–1871.

[37] M. Prinssen, E. Verhoeven, J. Buth, P. Cuypers, M. Van Sambeek, R. Balm, E. Buskens, D. Grobbee, J. Blankensteijn, Dutch randomized endovascular aneurysm management (dream) trial group. a randomized trial comparing conventional and endovascular repair of abdominal aortic aneurysms, The New England Journal of Medicine 351 (2004) 1607–18.

[38] F. A. Lederle, J. A. Freischlag, T. C. Kyriakides, F. T. Padberg Jr, J. S. Matsumura, T. R. Kohler, P. H. Lin, J. M. Jean-Claude, D. F. Cikrit, K. M. Swanson, et al., Outcomes following endovascular vs open repair of abdominal aortic aneurysm, the Journal of the American Medical Association 302 (2009) 1535–1542.

[39] J.-P. Becquemin, J.-C. Pillet, F. Lescalie, M. Sapoval, Y. Goueffic, P. Lermusiaux, E. Steinmetz, J. Marzelle, A randomized controlled trial of endovascular aneurysm repair versus open surgery for abdominal aortic aneurysms in low-to moderate-risk patients, Journal of Vascular Surgery 53 (2011) 1167–1173.

[40] J. A. Beckman, Is the dream of EVAR over?, The New England Journal of Medicine 367 (2012) 2041–43.

[41] P. De Rango, P. Cao, Long-term results of OVER: the dream of EVAR is not over, European Journal of Vascular and Endovascular Surgery 45 (2013) 313–314.

[42] P. Cao, P. De Rango, F. Verzini, G. Parlani, L. Romano, E. Cieri, Comparison of surveillance versus aortic endografting for small aneurysm repair (CAESAR): results from a randomised trial, European Journal of Vascular and Endovascular Surgery 41 (2011) 13–25.

[43] K. Ouriel, D. G. Clair, K. C. Kent, C. K. Zarins, Endovascular repair compared with surveillance for patients with small abdominal aortic aneurysms, Journal of Vascular Surgery 51 (2010) 1081–1087.

[44] S. Koutsias, G. Antoniou, C. Karathanos, V. Saleptsis, K. Stamoulis, A. Giannoukas, Endovascular treatment of infrarenal abdominal aortic aneurysm with short and angulated neck in high-risk patient., Case Reports in Vascular Medicine (2013) 898024.

[45] R. Hobo, J. Kievit, L. J. Leurs, J. Buth, Influence of severe infrarenal aortic neck angulation on complications at the proximal neck following endovascular AAA repair: a EUROSTAR study, Journal of Endovascular Therapy 14 (2007) 1–11.

[46] A. Schanzer, R. K. Greenberg, N. Hevelone, W. P. Robinson, M. H. Eslami, R. J. Goldberg, L. Messina, Predictors of abdominal aortic aneurysm sac enlargement after endovascular repair, Circulation 123 (2011) 2848–55.

[47] G. A. Antoniou, G. S. Georgiadis, S. a. Antoniou, G. Kuhan, D. Murray, A meta-analysis of outcomes of endovascular abdominal aortic aneurysm repair in patients with hostile and friendly neck anatomy, Journal of Vascular Surgery 57 (2013) 527–38.

[48] Z. Rancic, F. Pecoraro, T. Pfammatter, I. Banzic, H. Klein, K. Kyriakidis, D. Mayer, M. Lachat, The use of Endurant stent-graft for abdominal aortic aneurysm: the story about extension of instruction for use with persistent good results of stent-graft latest generation, The Journal of Cardiovascular Surgery 53 (2012) 579–94.

[49] J. T. Lee, B. W. Ullery, C. K. Zarins, C. Olcott, E. J. Harris, R. L. Dalman, EVAR Deployment in Anatomically Challenging Necks Outside the IFU, European Journal of Vascular and Endovascular Surgery 46 (2013) 65–73.

[50] N. Diehm, F. Dick, B. T. Katzen, J. Schmidli, C. Kalka, I. Baumgartner, Aortic neck dilatation after endovascular abdominal aortic aneurysm repair: a word of caution, Journal of Vascular Surgery 47 (2008) 886–892.

[51] A. Rodway, J. Powell, L. Brown, R. Greenhalgh, Do abdominal aortic aneurysm necks increase in size faster after endovascular than open repair?, European Journal of Vascular and Endovascular Surgery 35 (2008) 685–693.

[52] S. M. Sampaio, J. M. Panneton, G. Mozes, J. C. Andrews, A. a. Noel, M. Kalra, T. C. Bower, K. J. Cherry, T. M. Sullivan, P. Gloviczki, Aortic neck dilation after endovascular abdominal aortic aneurysm repair: should oversizing be blamed?, Annals of Vascular Surgery 20 (2006) 338–45.

[53] J. van Prehn, F. Schlösser, B. Muhs, H. Verhagen, F. Moll, J. van Herwaarden, Oversizing of aortic stent grafts for abdominal aneurysm repair: a systematic review of the benefits and risks, European Journal of Vascular and Endovascular Surgery 38 (2009) 42–53.

[54] S. R. Walsh, J. R. Boyle, A. G. Lynch, U. Sadat, J. P. Carpenter, T. Y. Tang, M. E. Gaunt, Suprarenal endograft fixation and medium-term renal function: systematic review and meta-analysis, Journal of Vascular Surgery 47 (2008) 1364–1370.

[55] A. England, J. Butterfield, R. Ashleigh, Incidence and effect of bare suprarenal stent struts crossing renal ostia following EVAR, European Journal of Vascular and Endovascular Surgery 32 (2006) 523–528.

[56] R. Uflacker, J. Robison, Endovascular treatment of abdominal aortic aneurysms: a review, European Radiology 11 (2001) 739–753.

[57] B. T. Katzen, A. A. MacLean, Past, present, and future endograft devices, Techniques in Vascular and Interventional Radiology 8 (2005) 16–21.

[58] K. Eckroth-Bernard, R. Garvin, E. Ryer, Current status of endovascular devices to treat abdominal aortic aneurysms, Biomedical Engineering and Computational Biology 5 (2013) 25–32.

[59] J. Duffy, R. Rolph, R. Clough, B. Modarai, P. Taylor, M. Waltham, et al., Stent graft types for endovascular repair of abdominal aortic aneurysms., Cochrane database of systematic reviews (Online) 3 (2013) CD008447–CD008447.

[60] D. T. Baril, T. S. Jacobs, M. L. Marin, Surgery insight: advances in endovascular repair of abdominal aortic aneurysms, Nature Clinical Practice Cardiovascular Medicine 4 (2007) 206–213.

[61] M. Mehta, F. E. Valdés, T. Nolte, G. J. Mishkel, W. D. Jordan, B. Gray, M. Eskandari, C. Botti, One-year outcomes from an international study of the ovation abdominal stent graft system for endovascular aneurysm repair, Journal of Vascular Surgery (2013).

[62] D. Krievins, A. Holden, J. Savlovskis, C. Calderas, C. Donayre, F. Moll, B. Katzen, C. Zarins, Evar using the nellix sac-anchoring endoprosthesis: treatment of favourable and adverse anatomy, European Journal of Vascular and Endovascular Surgery 42 (2011) 38–46.

[63] D. Hartl, D. Lagoudas, Thermomechanical characterization of shape memory alloy materials, in: Shape Memory Alloys, Springer, 2008, pp. 53–119.

[64] J. C. Palmaz, Review of polymeric graft materials for endovascular applications, Journal of Vascular and Interventional Radiology 9 (1998) 7–13.

[65] N. Demanget, S. Avril, P. Badel, L. Orgéas, C. Geindreau, J.-N. Albertini, J.-P. Favre, Computational comparison of the bending behavior of aortic stent-grafts, Journal of the Mechanical Behavior of Biomedical Materials 5 (2012) 272–282.

[66] I. C. Santos, A. Rodrigues, L. Figueiredo, L. A. Rocha, J. M. R. Tavares, Mechanical properties of stent–graft materials, Proceedings of the Institution of Mechanical Engineers, Part L: Journal of Materials Design and Applications 226 (2012) 330–341.

[67] L. Eadie, The investigation of the effect of in situ radiofrequency fenestration on the textile components of endovascular stent grafts., Master's thesis, NC State University, 2010.

[68] D. A. Vorp, Biomechanics of abdominal aortic aneurysm, Journal of Biomechanics 40 (2007) 1887–902.

[69] F. Inzoli, F. Boschetti, M. Zappa, T. Longo, R. Fumero, Biomechanical factors in abdominal aortic aneurysm rupture, European Journal of Vascular Surgery 7 (1993) 667–674.

[70] M. L. Raghavan, D. A. Vorp, M. P. Federle, M. S. Makaroun, M. W. Webster, Wall stress distribution on three-dimensionally reconstructed models of human abdominal aortic aneurysm, Journal of Vascular Surgery 31 (2000) 760–9.

[71] M. F. Fillinger, M. Raghavan, S. P. Marra, J. L. Cronenwett, F. E. Kennedy, In vivo analysis of mechanical wall stress and abdominal aortic aneurysm rupture risk, Journal of Vascular Surgery 36 (2002) 589–597.

[72] J. F. Rodríguez, C. Ruiz, M. Doblaré, G. a. Holzapfel, Mechanical stresses in abdominal aortic aneurysms: influence of diameter, asymmetry, and material anisotropy, Journal of Biomechanical Engineering 130 (2008) 021023.

[73] J. Vande Geest, D. Schmidt, M. Sacks, D. Vorp, The effects of anisotropy on the stress analyses of patient-specific abdominal aortic aneurysms, Annals of Biomedical Engineering 36 (2008) 921–932.

[74] T. C. Gasser, G. Görgülü, M. Folkesson, J. Swedenborg, Failure properties of intraluminal thrombus in abdominal aortic aneurysm under static and pulsating mechanical loads, Journal of Vascular Surgery 48 (2008) 179–188.

[75] D. H. Wang, M. S. Makaroun, M. W. Webster, D. A. Vorp, Effect of intraluminal thrombus on wall stress in patient-specific models of abdominal aortic aneurysm, Journal of Vascular Surgery 36 (2002) 598–604.

[76] A. Maier, M. W. Gee, C. Reeps, H.-H. Eckstein, W. A. Wall, Impact of calcifications on patient-specific wall stress analysis of abdominal aortic aneurysms., Biomechanics and Modeling in Mechanobiology 9 (2010) 511–21.

[77] Z.-Y. Li, et al., Impact of calcification and intraluminal thrombus on the computed wall stresses of abdominal aortic aneurysm, Journal of Vascular Surgery 47 (2008) 928–935.

[78] J. Lu, X. Zhou, M. L. Raghavan, Inverse elastostatic stress analysis in pre-deformed biological structures: Demonstration using abdominal aortic aneurysms, Journal of Biomechanics 40 (2007) 693–6.

[79] S. De Putter, B. Wolters, M. Rutten, M. Breeuwer, F. Gerritsen, F. Van de Vosse, Patient-specific initial wall stress in abdominal aortic aneurysms with a backward incremental method, Journal of Biomechanics 40 (2007) 1081–1090.

[80] M. W. Gee, C. Reeps, H. H. Eckstein, W. A. Wall, Prestressing in finite deformation abdominal aortic aneurysm simulation, Journal of Biomechanics 42 (2009) 1732–9.

[81] C. Reeps, M. Gee, A. Maier, M. Gurdan, H.-H. Eckstein, W. A. Wall, The impact of model assumptions on results of computational mechanics in abdominal aortic aneurysm, Journal of Vascular Surgery 51 (2010) 679–88.

[82] D. Bluestein, K. Dumont, M. De Beule, J. Ricotta, P. Impellizzeri, B. Verhegghe, P. Verdonck, Intraluminal thrombus and risk of rupture in patient specific abdominal aortic aneurysm FSI modelling, Computer Methods in Biomechanics and Biomedical Engineering 12 (2009) 73–81.

[83] P. Rissland, Y. Alemu, S. Einav, J. Ricotta, D. Bluestein, Abdominal aortic aneurysm risk of rupture: patient-specific FSI simulations using anisotropic model, Journal of Biomechanical Engineering 131 (2009) 031001.

[84] J. Leung, A. Wright, N. Cheshire, J. Crane, S. Thom, A. Hughes, Y. Xu, Fluid structure interaction of patient specific abdominal aortic aneurysms: a comparison with solid stress models, Biomedical Engineering Online 5 (2006) 33.

[85] J. Humphrey, G. A. Holzapfel, Mechanics, mechanobiology, and modeling of human abdominal aorta and aneurysms, Journal of Biomechanics 45 (2012) 805–814.

[86] G. Martufi, T. C. Gasser, Review: The role of biomechanical modeling in the rupture risk assessment for abdominal aortic aneurysms, Journal of Biomechanical Engineering 1 (2012) 523.

[87] M. Malina, B. Lindblad, K. Ivancev, M. Lindh, J. Malina, J. Brunkwall, Endovascular AAA exclusion: will stents with hooks and barbs prevent stent-graft migration?, Journal of Endovascular Surgery 5 (1998) 310–317.

[88] T. Resch, M. Malina, B. Lindblad, J. Malina, J. Brunkwall, K. Ivancev, The impact of stent design on proximal stent-graft fixation in the abdominal aorta: an experimental study, European Journal of Vascular and Endovascular Surgery 20 (2000) 190–5.

[89] R. Veerapen, A. Dorandeu, I. Serre, J.-P. Berthet, C. H. Marty-Ane, H. Mary, P. Alric, Improvement in proximal aortic endograft fixation: an experimental study using different stent-grafts in human cadaveric aortas, Journal of Endovascular Therapy 10 (2003) 1101–9.

[90] N. Melas, A. Saratzis, N. Saratzis, J. Lazaridis, D. Psaroulis, K. Trygonis, D. Kiskinis, Aortic and iliac fixation of seven endografts for abdominal-aortic aneurysm repair in an experimental model using human cadaveric aortas, European Journal of Vascular and Endovascular Surgery 40 (2010) 429–435.

[91] F. R. Arko, M. Heikkinen, E. S. Lee, A. Bass, J. M. Alsac, C. K. Zarins, Iliac fixation length and resistance to in-vivo stent-graft displacement, Journal of Vascular Surgery 41 (2005) 664–71.

[92] E. H. Murphy, E. D. Johnson, F. R. Arko, Device-specific resistance to in vivo displacement of stent-grafts implanted with maximum iliac fixation, Journal of Endovascular Therapy 14 (2007) 585–92.

[93] T. J. Corbett, D. S. Molony, a. Callanan, T. M. McGloughlin, The effect of vessel material properties and pulsatile wall motion on the fixation of a proximal stent of an endovascular graft, Medical Engineering and Physics 33 (2011) 106–11.

[94] J.-N. Albertini, J. Macierewicz, S. Yusuf, P. Wenham, B. Hopkinson, Pathophysiology of proximal perigraft endoleak following endovascular repair of abdominal aortic aneurysms: a study using a flow model, European Journal of Vascular and Endovascular Surgery 22 (2001) 53–56.

[95] G. Schurink, N. Aarts, J. Van Baalen, L. Kool, J. Van Bockel, Experimental study of the influence of endoleak size on pressure in the aneurysm sac and the consequences of thrombosis, British Journal of Surgery 87 (2000) 71–78.

[96] C. S. Skillern, S. L. Stevens, K. T. Piercy, R. L. Donnell, M. B. Freeman, M. H. Goldman, Endotension in an experimental aneurysm model, Journal of Vascular Surgery 36 (2002) 814–817.

[97] K. K. Lin, J. A. Kratzberg, M. L. Raghavan, Role of aortic stent graft oversizing and barb characteristics on folding, Journal of Vascular Surgery 55 (2012) 1401–1409.

[98] J.-D. Singland, J. Voulgre, G. Picard, D. Mitton, P. Cluzel, F. Lavaste, E. Kieffer, F. Koskas, Static mechanical properties of custom-made aortic endografts, Annals of Vascular Surgery 19 (2005) 293–301.

[99] A. H. M. Bashar, T. Kazui, N. Washiyama, H. Terada, K. Yamashita, M. E. Haque, Mechanical properties of various z-stent designs: An endovascular stent-grafting perspective, Artificial Organs 27 (2003) 714–721.

[100] O. A. Oshin, T. V. How, J. A. Brennan, R. K. Fisher, R. G. McWilliams, S. R. Vallabhaneni, Magnitude of the forces acting on target vessel stents as a result of a mismatch between native aortic anatomy and fenestrated stent-grafts, Journal of Endovascular Therapy 18 (2011) 569–575.

[101] C. R. Johnston, K. Lee, J. Flewitt, R. Moore, G. M. Dobson, G. M. Thornton, The mechanical properties of endovascular stents: an in vitro assessment, Cardiovascular Engineering 10 (2010) 128–135.

[102] T. Yao, B. D. Choules, J. P. Rust, M. W. King, The development of an in vitro test method for predicting the abrasion resistance of textile and metal components of endovascular stent grafts, Journal of Biomedical Materials Research Part B: Applied Biomaterials 102B (2014) 488–499.

[103] G. Mestres, J. P. Uribe, C. García-Madrid, E. Miret, X. Alomar, M. Burrell, V. Riambau, The Best Conditions for Parallel Stenting During EVAR: An InVitro Study, European Journal of Vascular and Endovascular Surgery 44 (2012) 468–73.

[104] E. S. Di Martino, A. Bohra, C. Scotti, E. Finol, D. A. Vorp, Wall Stresses Before and After Endovascular Repair of Abdominal Aortic Aneurysms, ASME Conference Proceedings 2004 (2004) 325–326.

[105] C. Kleinstreuer, Z. Li, C. a. Basciano, S. Seelecke, M. a. Farber, Computational mechanics of Nitinol stent grafts, Journal of Biomechanics 41 (2008) 2370–8.

[106] A. Prasad, N. Xiao, X.-Y. Gong, C. K. Zarins, C. A. Figueroa, A computational framework for investigating the positional stability of aortic endografts, Biomechanics and Modeling in Mechanobiology 12 (2012) 869–87.

[107] N. Demanget, P. Latil, L. Orgéas, P. Badel, S. Avril, C. Geindreau, J.-N. Albertini, J.-P. Favre, Severe bending of two aortic stent-grafts: An experimental and numerical mechanical analysis, Annals of Biomedical Engineering 40 (2012) 2674–2686.

[108] N. Demanget, A. Duprey, P. Badel, L. Orgéas, S. Avril, C. Geindreau, J.-N. Albertini, J.-P. Favre, Finite element analysis of the mechanical performances of 8 marketed aortic stent-grafts, Journal of Endovascular Therapy 20 (2013) 523–535.

[109] A. Duménil, A. Kaladji, M. Castro, S. Esneault, A. Lucas, M. Rochette, C. Göksu, P. Haigron, Finite-element-based matching of pre- and intraoperative data for image-guided endovascular aneurysm repair., IEEE Transactions on Biomedical Engineering 60 (2013) 1353–1362.

[110] P. Haigron, a. Duménil, a. Kaladji, M. Rochette, B. Bou Said, S. Esneault, H. Walter-Le Berre, G. Mouktadiri, M. Castro, P. Louat, D. Roche, C. Göksu, J. Marzelle, a. Cardon, J.-P. Becquemin, a. Lucas, Angiovision: Aortic stent-graft placement by augmented angionavigation, IRBM 34 (2013) 167–175.

[111] F. Auricchio, M. Conti, S. Marconi, A. Reali, J. L. Tolenaar, S. Trimarchi, Patient-specific aortic endografting simulation: From diagnosis to prediction, Computers in Biology and Medicine 43 (2013) 386–394.

[112] S. von Sachsen, B. Senf, O. Burgert, J. Meixensberger, H. Florek, F. Mohr, C. Etz, Stent graft visualization and planning tool for endovascular surgery using finite element analysis, International Journal of Computer Assisted Radiology and Surgery (2013).

[113] M. Arokiaraj, I. Palacios, Finite element modeling of a novel self-expanding endovascular stent method in treatment of aortic aneurysms., Scientific Reports 4 (2014) 3630.

[114] B. A. Howell, T. Kim, A. Cheer, H. Dwyer, D. Saloner, T. A. M. Chuter, Computational fluid dynamics within bifurcated abdominal aortic stent-grafts, Journal of Endovascular Therapy 14 (2007) 138–43.

[115] D. S. Molony, E. G. Kavanagh, P. Madhavan, M. T. Walsh, T. M. McGloughlin, A computational study of the magnitude and direction of migration forces in patient-specific abdominal aortic aneurysm stent-grafts, European Journal of Vascular and Endovascular Surgery 40 (2010) 332–9.

[116] C. A. Figueroa, C. A. Taylor, V. Yeh, A. J. Chiou, C. K. Zarins, Effect of curvature on displacement forces acting on aortic endografts: a 3-dimensional computational analysis, Journal of Endovascular Therapy 16 (2009) 284–94.

[117] T. Frauenfelder, M. Lotfey, T. Boehm, S. Wildermuth, Computational fluid dynamics: hemodynamic changes in abdominal aortic aneurysm after stent-graft implantation, Cardiovascular and Interventional Radiology 29 (2006) 613–23.

[118] G. Xiong, G. Choi, C. A. Taylor, Virtual Interventions for Image-based Blood Flow Computation., Computer Aided Design 44 (2012) 3–14.

[119] Z. Li, C. Kleinstreuer, Fluid-structure interaction effects on sac-blood pressure and wall stress in a stented aneurysm., Journal of Biomechanical Engineering 127 (2005) 662–671.

[120] Z. Li, C. Kleinstreuer, Effects of major endoleaks on a stented abdominal aortic aneurysm, Journal of Biomechanical Engineering 128 (2006) 59–68.

[121] Z. Li, C. Kleinstreuer, Computational analysis of type II endoleaks in a stented abdominal aortic aneurysm model, Journal of Biomechanics 39 (2006) 2573–2582.

[122] D. S. Molony, A. Callanan, E. G. Kavanagh, M. T. Walsh, T. M. McGloughlin, Fluid-structure interaction of a patient-specific abdominal aortic aneurysm treated with an endovascular stent-graft, Biomedical Engineering Online 8 (2009) 24.

[123] A. Amblard, H. W.-L. Berre, B. Bou-Saïd, M. Brunet, Analysis of type I endoleaks in a stented abdominal aortic aneurysm, Medical Engineering and Physics 31 (2009) 27–33.

[124] K. Liffman, M. M. Lawrence-Brown, J. B. Semmens, A. Bui, M. Rudman, D. E. Hartley, Analytical modeling and numerical simulation of forces in an endoluminal graft, Journal of Endovascular Therapy 8 (2001) 358–371.

[125] B. Wolters, M. Rutten, G. Schurink, F. van de Vosse, Computational modelling of endoleak after endovascular repair of abdominal aortic aneurysms, International Journal for Numerical Methods in Biomedical Engineering 26 (2010) 322–335.

[126] A. Fedorov, R. Beichel, J. Kalpathy-Cramer, J. Finet, J.-C. Fillion-Robin, S. Pujol, C. Bauer, D. Jennings, F. Fennessy, M. Sonka, et al., 3d slicer as an image computing platform for the quantitative imaging network, Magnetic resonance imaging 30 (2012) 1323–1341.

[127] M. Conti, D. Van Loo, F. Auricchio, M. De Beule, G. De Santis, B. Verhegghe, S. Pirrelli, A. Odero, Impact of carotid stent cell design on vessel scaffolding: a case study comparing experimental investigation and numerical simulations, Journal of Endovascular Therapy 18 (2011) 397–406.

[128] P. Mortier, M. De Beule, D. Van Loo, B. Masschaele, P. Verdonck, B. Verhegghe, Automated generation of a finite element stent model, Medical & Biological Engineering & Computing 46 (2008) 1169–1173.

[129] S. De Bock, F. Iannaccone, M. De Beule, D. Van Loo, F. Vermassen, B. Verhegghe, P. Segers, Filling the void: A coalescent numerical and experimental technique to determine aortic stent graft mechanics, Journal of Biomechanics 46 (2013) 2477–2482.

[130] L. Wales, M. Dunckley, N. Bohm, T. Kwok, M. Bratby, R. Morgan, M. Thompson, I. Loftus, Device-specific outcomes following endovascular aortic aneurysm repair, European Journal of Vascular and Endovascular Surgery 36 (2008) 661–7.

[131] B. Mensel, J.-P. Kühn, T. Träger, M. Dührkoop, W. V Bernstorff, C. Rosenberg, A. Hoene, R. Puls, Technical and Clinical Outcome of Talent versus Endurant Endografts for Endovascular Aortic Aneurysm Repair, PLOS ONE 7 (2012) e38468.

[132] I. R. Sincos, E. S. da Silva, S. Q. Belczak, A. P. W. Baptista Sincos, M. de Lourdes Higuchi, V. Gornati, J. P. Otoch, R. Aun, Histologic analysis of stent graft oversizing in the thoracic aorta, Journal of Vascular Surgery 58 (2013) 1644–1651.

[133] G. J. Hall, E. P. Kasper, Comparison of element technologies for modeling stent expansion, Journal of Biomechanical Engineering 128 (2006) 751–6.

[134] F. Auricchio, C. Taylor, Shape-memory alloys: macromodeling and numerical simulations of the superelastic behavior, Computer Methods in Applied Mechancis and Engineering 146 (1997) 281–312.

[135] N. Rebelo, N. Walker, H. Foadian, Simulation of implantable nitinol stents, in: Proceedings of the 2001 Abaqus Users Conference, Providence, Rhode Island, USA, 2001.

[136] E. Henderson, D. Nash, W. Dempster, On the experimental testing of fine nitinol wires for medical devices, Journal of the Mechanical Behavior of Biomedical Materials 4 (2011) 261–268.

[137] A. R. Pelton, J. Dicello, S. Miyazaki, Optimisation of processing and properties of medical grade Nitinol wire, Minimally Invasive Therapy & Allied Technologies 9 (2000) 107–118.

[138] L. Petrini, F. Migliavacca, P. Massarotti, S. Schievano, G. Dubini, F. Auricchio, Computational studies of shape memory alloy behavior in biomedical applications, Journal of Biomechanical Engineering 127 (2005) 716–725.

[139] A. Prasad, L. K. To, M. L. Gorrepati, C. K. Zarins, C. A. Figueroa, Computational analysis of stresses acting on intermodular junctions in thoracic aortic endografts, Journal of Endovascular Therapy 18 (2011) 559–568.

[140] S. De Bock, F. Iannaccone, G. De Santis, M. De Beule, D. Van Loo, D. Devos, F. Vermassen, P. Segers, B. Verhegghe, Virtual evaluation of stent graft deployment: A validated modeling and simulation study, Journal of the Mechanical Behavior of Biomedical Materials 13 (2012) 129–139.

[141] T. J. Corbett, A. Callanan, L. G. Morris, B. J. Doyle, P. a. Grace, E. G. Kavanagh, T. M. McGloughlin, A review of the in vivo and in vitro biomechanical behavior and performance of postoperative abdominal aortic aneurysms and implanted stent-grafts, Journal of Endovascular Therapy 15 (2008) 468–84.

[142] A. R. Pelton, V. Schroeder, M. R. Mitchell, X.-Y. Gong, M. Barney, S. W. Robertson, Fatigue and durability of Nitinol stents, Journal of the Mechanical Behavior of Biomedical Materials 1 (2008) 153–64.

[143] J.-P. P. M. de Vries, The proximal neck: the remaining barrier to a complete EVAR world, Seminars in Vascular Surgery 25 (2012) 182–6.

[144] Z. Li, C. Kleinstreuer, M. Farber, Computational analysis of biomechanical contributors to possible endovascular graft failure, Biomechanics and Modeling in Mechanobiology 4 (2005) 221–34.

[145] P. E. Hart, N. J. Nilsson, B. Raphael, A formal basis for the heuristic determination of minimum cost paths, Systems Science and Cybernetics, IEEE Transactions on 4 (1968) 100–107.

[146] R Core Team, R: A Language and Environment for Statistical Computing, R Foundation for Statistical Computing, Vienna, Austria, 2013. URL: `http://www.R-project.org`.

[147] J. van Keulen, K. Vincken, J. van Prehn, J. Tolenaar, L. Bartels, M. Viergever, F. Moll, J. van Herwaarden, The influence of different types of stent grafts on aneurysm neck dynamics after endovascular aneurysm repair, European Journal of Vascular and Endovascular Surgery 39 (2010) 193–199.

[148] H. Ishibashi, T. Ishiguchi, T. Ohta, I. Sugimoto, T. Yamada, M. Tadakoshi, N. Hida, Y. Orimoto, Remodeling of proximal neck angulation after endovascular aneurysm repair, Journal of Vascular Surgery 56 (2012) 1201–5.

[149] K. Hoshina, T. Akai, T. Takayama, M. Kato, T. Nakazawa, H. Okamoto, K. Shigematsu, T. Miyata, Outcomes and morphologic changes after endovascular repair for abdominal aortic aneurysms with a severely angulated neck, Circulation 77 (2013) 1996–2002.

[150] J. van Keulen, F. Moll, J. van Herwaarden, Tips and techniques for optimal stent graft placement in angulated aneurysm necks, Journal of Vascular Surgery 52 (2010) 1081–1086.

[151] K. Liffman, M. M. Lawrence-Brown, J. B. Semmens, I. D. Šutalo, A. Bui, F. White, D. E. Hartley, Suprarenal fixation: effect on blood flow of an endoluminal stent wire across an arterial orifice, Journal of Endovascular Therapy 10 (2003) 260–274.

[152] Z. Sun, T. Chaichana, Investigation of the Hemodynamic Effect of Stent Wires on Renal Arteries in Patients with Abdominal Aortic Aneurysms Treated with Suprarenal Stent-Grafts, CardioVascular and Interventional Radiology 32 (2009) 647–657.

[153] R. Balm, R. Stokking, R. Kaatee, J. D. Blankensteijn, B. C. Eikelboom, M. S. van Leeuwen, Computed tomographic angiographic imaging of abdominal aortic aneurysms: implications for transfemoral endovascular aneurysm management, Journal of Vascular Surgery 26 (1997) 231–7.

[154] C. McDonnell, M. Halak, A. Bartlett, S. Baker, Abdominal aortic aneurysm neck morphology: proposed classification system, Irish Journal of Medical Science 175 (2006) 4–8.

[155] J. W. van Keulen, F. L. Moll, J. L. Tolenaar, H. J. M. Verhagen, J. A. van Herwaarden, Validation of a new standardized method to measure proximal aneurysm neck angulation, Journal of Vascular Surgery 51 (2010) 821–8.

[156] C. Reeps, a. Maier, J. Pelisek, F. Härtl, V. Grabher-Meier, W. a. Wall, M. Essler, H.-H. Eckstein, M. W. Gee, Measuring and modeling patient-specific distributions of material properties in abdominal aortic aneurysm wall, Biomechanics and Modeling in Mechanobiology 12 (2013) 717–33.

[157] P. Watton, N. Hill, Evolving mechanical properties of a model of abdominal aortic aneurysm, Biomechanics and modeling in mechanobiology 8 (2009) 25–42.

[158] W. C. Krupski, R. B. Rutherford, Update on open repair of abdominal aortic aneurysms: the challenges for endovascular repair, Journal of the American College of Surgeons 199 (2004) 946–960.

[159] M. L. Schermerhorn, a. J. O'Malley, A. Jhaveri, P. Cotterill, F. Pomposelli, B. E. Landon, Endovascular vs. open repair of abdominal aortic aneurysms in the Medicare population, The New England Journal of Medicine 358 (2008) 464–74.

[160] N. Chakfé, F. Dieval, G. Riepe, D. Mathieu, I. Zbali, F. Thaveau, C. Heintz, J.-G. Kretz, B. Durand, Influence of the Textile Structure on the Degradation of Explanted Aortic Endoprostheses, European Journal of Vascular and Endovascular Surgery 27 (2004) 33–41.

[161] C. K. Zarins, C. A. Taylor, Endovascular device design in the future: transformation from trial and error to computational design, Journal of Endovascular Therapy 16 Suppl 1 (2009) I12–21.

[162] B. J. Doyle, A. J. Cloonan, M. T. Walsh, D. a. Vorp, T. M. McGloughlin, Identification of rupture locations in patient-specific abdominal aortic aneurysms using experimental and computational techniques, Journal of Biomechanics 43 (2010) 1408–16.

[163] Z. Li, C. Kleinstreuer, Analysis of biomechanical factors affecting stent-graft migration in an abdominal aortic aneurysm model, Journal of Biomechanics 39 (2006) 2264–73.

[164] G. De Santis, M. De Beule, K. Van Canneyt, P. Segers, P. Verdonck, B. Verhegghe, Full-hexahedral structured meshing for image-based computational vascular modeling, Medical Engineering and Physics 33 (2011) 1318–1325.

[165] B. J. Doyle, T. J. Corbett, A. J. Cloonan, M. R. O'Donnell, M. T. Walsh, D. a. Vorp, T. M. McGloughlin, Experimental modelling of aortic aneurysms: novel applications of silicone rubbers, Medical Engineering and Physics 31 (2009) 1002–12.

[166] M. J. D. Powell, Advances in Optimization and Numerical Analysis, Kluwer Academic Publishers, Dordrecht, 1994, pp. 51–67.

[167] S. De Bock, F. Iannaccone, G. De Santis, M. De Beule, P. Mortier, B. Verhegghe, P. Segers, Our capricious vessels: The influence of stent design and vessel geometry on the mechanics of intracranial aneurysm stent deployment, Journal of Biomechanics 45 (2012) 1353–1359.

[168] J. W. van Keulen, J. van Prehn, M. Prokop, F. L. Moll, J. A. van Herwaarden, Dynamics of the aorta before and after endovascular aneurysm repair: a systematic review, European Journal of Vascular and Endovascular Surgery 38 (2009) 586–96.

[169] F. R. Arko, E. H. Murphy, C. M. Davis, E. D. Johnson, S. T. Smith, C. K. Zarins, Dynamic geometry and wall thickness of the aortic neck of abdominal aortic aneurysms with intravascular ultrasonography, Journal of Vascular Surgery 46 (2007) 891–6; discussion 896–7.

[170] N. Grondal, M. B. Bramsen, M. D. Thomsen, C. B. Rasmussen, J. S. Lindholt, The cardiac cycle is a major contributor to variability in size measurements of abdominal aortic aneurysms by ultrasound, European Journal of Vascular and Endovascular Surgery 43 (2012) 30–33.

[171] M.-K. Ganten, U. Krautter, H. von Tengg-Kobligk, D. Böckler, H. Schumacher, W. Stiller, S. Delorme, H.-U. Kauczor, G. W. Kauffmann, M. Bock, Quantification of aortic distensibility in abdominal aortic aneurysm using ecg-gated multi-detector computed tomography, European Radiology 18 (2008) 966–973.

[172] M. van 't Veer, J. Buth, M. Merkx, P. Tonino, H. van den Bosch, N. Pijls, F. van de Vosse, Biomechanical properties of abdominal aortic aneurysms assessed by simultaneously measured pressure and volume changes in humans, Journal of Vascular Surgery 48 (2008) 1401–1407.

[173] A. P. Tierney, A. Callanan, T. M. McGloughlin, Use of regional mechanical properties of abdominal aortic aneurysms to advance finite element modeling of rupture risk, Journal of Endovascular Therapy 19 (2012) 100–14.

[174] D. Palombo, D. Valenti, M. Ferri, A. Gaggiano, R. Mazzei, M. Vola, S. Tettoni, Changes in the proximal neck of abdominal aortic aneurysms early after endovascular treatment, Annals of Vascular Surgery 17 (2003) 408–410.

[175] M. F. Badran, D. A. Gould, I. Raza, R. G. McWilliams, O. Brown, P. L. Harris, G. L. Gilling-Smith, J. Brennan, D. White, S. Meakin, Others, Aneurysm neck diameter after endovascular repair of abdominal aortic aneurysms, Journal of Vascular and Interventional Radiology 13 (2002) 887–892.

[176] L. Desender, Z. Rancic, R. Aggarwal, J. Duchateau, M. Glenck, M. Lachat, F. Vermassen, I. Van Herzeele, et al., Patient-specific rehearsal prior to evar: A pilot study, European Journal of Vascular and Endovascular Surgery 45 (2013) 639–647.

[177] F. J. H. Gijsen, F. Migliavacca, S. Schievano, L. Socci, L. Petrini, A. Thury, J. J. Wentzel, A. F. W. van der Steen, P. W. S. Serruys, G. Dubini, Simulation of stent deployment in a realistic human coronary artery, Biomedical Engineering Online 7 (2008) 23.

[178] P. Mortier, G. A. Holzapfel, M. De Beule, D. Van Loo, Y. Taeymans, P. Segers, P. Verdonck, B. Verhegghe, A novel simulation strategy for stent insertion and deployment in curved coronary bifurcations: comparison of three drug-eluting stents, Annals of Biomedical Engineering 38 (2010) 88–99.

[179] F. Auricchio, M. Conti, M. De Beule, G. De Santis, B. Verhegghe, Carotid artery stenting simulation: from patient-specific images to finite element analysis, Medical Engineering and Physics 33 (2011) 281–289.

[180] W. Wu, M. Qi, X.-P. Liu, D.-Z. Yang, W.-Q. Wang, Delivery and release of nitinol stent in carotid artery and their interactions: a finite element analysis, Journal of Biomechanics 40 (2007) 3034–3040.

[181] D. Ma, G. F. Dargush, S. K. Natarajan, E. I. Levy, A. H. Siddiqui, H. Meng, Computer modeling of deployment and mechanical expansion of neurovascular flow diverter in patient-specific intracranial aneurysms, Journal of Biomechanics 45 (2012) 2256–2263.

[182] T. C. Gasser, R. W. Ogden, G. a. Holzapfel, Hyperelastic modelling of arterial layers with distributed collagen fibre orientations, Journal of the Royal Society, Interface / the Royal Society 3 (2006) 15–35.

[183] Z. Li, C. Kleinstreuer, Computational analysis of type II endoleaks in a stented abdominal aortic aneurysm model, Journal of Biomechanics 39 (2006) 2573–2582.

[184] M. De Beule, Finite element stent design, Ph.D. thesis, Ghent University, 2008.

[185] P. Mortier, Computer modelling of coronary bifurcation stenting, Ph.D. thesis, Ghent University, 2010.

[186] M. Conti, Finite Element Analysis of Carotid Artery Stenting, Ph.D. thesis, Ghent University, Universit degli Studi di Pavia, 2010.